SPECTRAL SLICING FILTERS IN TITANIUM DIFFUSED LITHIUM NIOBATE ($Ti:LiNbO_3$)

A Dissertation

by

RENATO CUNHA RABELO

Submitted to the Office of Graduate Studies of
Texas A&M University
in partial fulfillment of the requirements for the degree of

DOCTOR OF PHILOSOPHY

December 2008

Major Subject: Electrical Engineering

SPECTRAL SLICING FILTERS IN TITANIUM DIFFUSED LITHIUM NIOBATE ($Ti:LiNbO_3$)

A Dissertation

by

RENATO CUNHA RABELO

Submitted to the Office of Graduate Studies of
Texas A&M University
in partial fulfillment of the requirements for the degree of

DOCTOR OF PHILOSOPHY

Approved by :

Chair of Committee,	Ohannes Eknoyan
Committee Members,	Steven Wright
	Christi K. Madsen
	Alexei Sokolov
Head of Department,	Costas Georghiades

December 2008

Major Subject: Electrical Engineering

ABSTRACT

Spectral Slicing Filters in Titanium Diffused Lithium Niobate ($Ti:LiNbO_3$).

(December 2008)

Renato Cunha Rabelo, B.S., Instituto Tecnológico de Aeronáutica;

M.S., Instituto Tecnológico de Aeronáutica

Chair of Advisory Committee: Dr. Ohannes Eknoyan

A tunable guided-wave optical filter that performs spectral slicing at the 1530nm wavelength regime in $Ti:LiNbO_3$ was proposed and fabricated. It is aimed at minimizing crosstalk between channels in dense wavelength division multiplexing (DWDM) optical network applications. The design utilizes a sparse grating allowing the selection of equally spaced channels in the frequency domain. Between selected channels, equally spaced nulls are also produced. The sparse grating is formed by using N coupling regions with different lengths along the direction of propagation of light in the waveguide, generating N-1 equally spaced nulls between adjacent selected channels. The distance between the centers of adjacent coupling regions is kept constant. The filtering is based on codirectional polarization coupling between transverse electric (TE) and transverse magnetic (TM) orthogonal modes in a waveguide through an overlay of strain-induced index grating, via the strain-optic effect.

Two types of devices were fabricated. In the first type, the sparse gratings were produced on straight channel waveguides. Selected channels emerge from the device in a

polarization state orthogonal to the input and a polarizer is needed to observe the filtered light. For the second type, an asymmetric Mach-Zehnder interferometer configuration was used to eliminate the need of the polarizer at the output, and yields an output response that is polarization independent.

Both types of devices were fabricated on x-cut y-propagating $LiNbO_3$ substrates, with $N = 6$ strain-induced coupling regions. The single mode channel waveguides were formed by Ti diffusion. Electrode patterns centered about the optical waveguide were defined by liftoff.

In the straight channel devices, insertion loss was less than 2.5 dB on a 43 mm sample. The 3-dB channel bandwidth of the selected channels is approximately 1.0 nm. Devices were tuned thermally as well as by voltage application to surface electrodes resulting in tuning rates of 1.0 nm/^{o}C and 0.04148 nm/V, respectively.

In the polarization independent device the insertion loss for the phase-matched wavelength was 5.3 dB on a 53 mm long chip. The 3-dB bandwidth was also ~1.0 nm and the thermal tuning rate 1.0 nm/^{o}C. The experimental results are in good agreement with design theory.

To my wife and my children

"I have the strength for everything

through Him who empowers me"

(Philippians 4:13)

ACKNOWLEDGMENTS

I would like to thank my advisor and committee chair, Dr. Ohannes Eknoyan, for his patience, constant encouragement and guidance during the course of my studies. Also, I am grateful to my committee members, Dr. Christi K. Madsen, Dr. Steven Wright and Dr. Alexey Sokolov for their willingness to serve on the committee as of the first moment they were asked to join and as well for their time and effort in following my research steps. Also to be remembered are the contributions made by Dr. Henry F. Taylor (*in memoriam*), who was an early member on the advisory committee and first proposed the approach pursued in this work.

I also would like to take the opportunity to acknowledge other people for their support to the execution of my research work. Mr. Robert Atkins, Lab Manager, and Mr. Jim Gardner, Senior Lab technician, always contributed their best and acted in a timely manner keeping the fabrication facility working smoothly, upgrading machines and also sharing their professional knowledge, which, in the end, also contributed to my learning experience. Friends and lab mates are also to be acknowledged for having listened to me at difficult times and for having provided me with some good laughs along the way. They are: Ryoung-Han Kim, Hsin-Hui Kuo, Yang (Phillip) Ping, Yong-Wook Shin, Mehmet Solmaz, Murat Yapici, Alexander Wojcik, Jae Woo Suh, Xiaomin Song, Won Ju Sung, Donald Adams, Wee Chong and Xia (Alex) Xing.

In a moment like this it is impossible to forget the influence my parents, Reginor Luiz Rabelo e Vicentina Cunha Rabelo (*in memoriam*), have on my education and

character. They made every effort to provide me with the best they had, and when they could not, they showed me the way to accomplish it and supported me. They also taught me early on the value of effort and perseverance in life. I will be forever thankful to them for having put me on the road which led me to this achievement.

There are also the people whom I chose to share this moment with: my family. My beloved wife Sylvia many times worked as a buffer to isolate me from everyday problems, giving me the peace of mind I needed to develop the research. My children Ana Gabriela and John Lucas were always the inspiration to continue working as they would receive me at home with their smiles and showing unconditional love in their eyes. I am thankful to them for having provided me with the proper environment I needed when I was relaxing at home with them.

I would like to thank a good friend Josiel Urbaninho de Arruda for the support he provided in Brazil, taking care of all the paperwork and other interests of mine while I could not be there.

Another invaluable aid was the financial support provided by the Brazilian Air Force, which sponsored all my studies here at Texas A&M, and for that I am also grateful.

Finally, I would like to express my gratitude to God for having given me the life, health and opportunity to pursue this endeavor in my lifetime.

TABLE OF CONTENTS

TABLE OF CONTENTS (continued)

LIST OF FIGURES

LIST OF FIGURES (continued)

FIGURE Page

LIST OF FIGURES (continued)

FIGURE Page

LIST OF FIGURES (continued)

FIGURE Page

LIST OF TABLES

CHAPTER I

INTRODUCTION

The impact of broadband communications in today's society is undeniable. It has changed the way people communicate with each other; acquire information, shop and do other activities.

Most of the communication traffic for those activities is performed through the internet. Many believe that the internet would not be what it represents to us today had it not been for the fiber optic communications. Today it is possible either to send data, from a bank transaction or an online purchase; sounds, from a voice over Internet Protocol (VoIP) phone call or images from a High Definition (HD) TV signal, to mention a few examples, all through the same media, most probably at the same time, with high reliability and quality.

It should also be noted that there is also a constant increase in the final consumer demand for higher quality, higher fidelity and as a consequence higher bandwidth communications.

Fiber optic communication was able to deliver the bandwidth needed in the early days of the broadband communication era and is likely to continue providing bandwidth for the increased consumer demand because of its high carrier frequencies (~100 THz) and achieved low signal attenuation (0.2 dB/km @ λ=1550 nm) [1-3].

This dissertation follows the style and format of *IEEE Journal of Lightwave Technology*.

Therefore the demand for systems which could harness the bandwidth available in fiber optic communication systems has always been the drive to the research and development of new devices that would enable a whole system to perform the task.

In the early days of fiber optic communications, despite the huge channel bandwidth available, not much of that was used. Only one wavelength was sent down the fiber and the maximum attainable transmission rate was limited by how fast the light source output could be modulated, most often in a digital manner, by switching it on and off. This was limited to a few hundreds of megabits per second, and reached its peak around some tens of gigabits per second when employing a modulator external to the source in a scheme named indirect modulation.

On the single wavelength regime of the early fiber optic systems, fiber optic dispersion and attenuation prevented the optical signal from being transmitted over long distances using one single length of fiber. After traveling some maximum length the optical signal needed detection (optical to electrical conversion), regeneration in the electrical domain (to restore original shape) and a conversion back to the optical domain, before it could be coupled to and continue its path on another length of fiber. The complexity of this process hindered efforts in sending more than one wavelength down the fiber, because it would mean a geometric increase in the optical and electronic components at all detection-regeneration sites.

The advent of Erbium Doped Fiber Amplifiers, EDFA for short, enabled part of the regeneration to be done for multiple wavelengths at the same time. Although it only

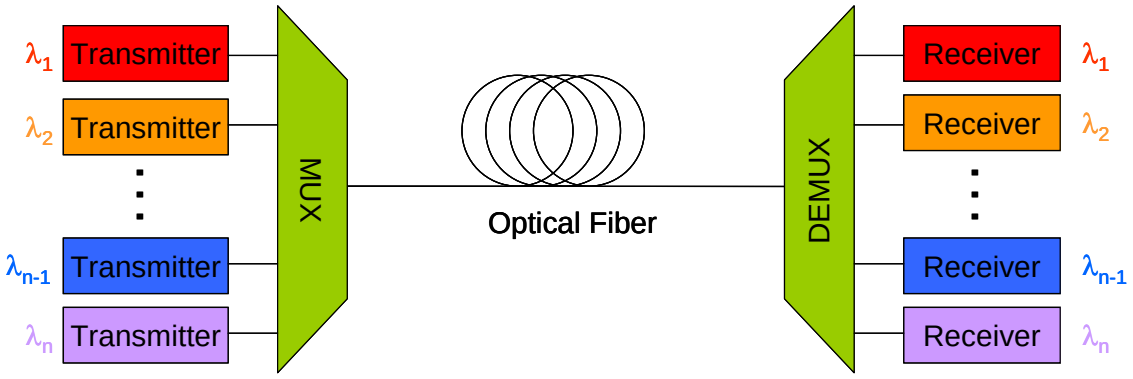

Fig. 1. Schematic diagram of a WDM optical link.

provides amplification as a form of restoring the amplitude of attenuated signals, not dealing with the distortion caused by dispersion, it enabled the first implementations of Wavelength Division Multiplexing, WDM for short. In this approach, instead of sending light carrying digital information down the fiber by using just one wavelength switched at a fixed bit rate; information is sent over a number of wavelengths, each carrying an independent communication channel, multiplying the possible bit rate carried by the fiber, called the aggregate bit rate. Fig. 1 shows a schematic diagram of a WDM system.

More recently with the advancement of the component technology by producing tunable lasers, narrowband optical filters, and other devices, it was possible to pack optical channels even closer together in a technique since then called Dense Wavelength Division Multiplexing, or DWDM for short. One of the early recommendations of ITU-T on DWDM, the G.692, defined 43 wavelength channels, from 1530 to 1565, with 100

GHz spacing between channels, each channel carrying 10 gigabit per second signal, resulting in an aggregate bandwidth of 430 Gbps [4].

Nowadays, commercial systems with more channels, up to 128, and transmission rates up to 40 Gbps, resulting in aggregate bandwidths on the order of some Tbps can be obtained on a single fiber.

From these facts, one can conclude that the feasibility of a DWDM optical network is intimately related to the ability of multiplexing and launching many wavelengths in one fiber, then at the receiving end, be able to demultiplex and detect each and every one of the channels. In addition to that, the devices that are included in the light path do not perform the same way over that bandwidth, either in amplitude or dispersion wise.

Therefore a DWDM optical network demands devices capable of filtering the individual channels respecting strictly defined pass bands and stop bands; in some cases wavelength sensitive routing devices; devices capable of compensating optical dispersion for different wavelengths at the same time, and also devices capable of compensating wavelength dependent losses in the system as well as wavelength dependent gains in EDFA's. Those are still some of the ongoing research efforts to enable DWDM, with ever increasing channel density. Generically speaking, DWMD systems must rely on very strict response optical filters.

Optical Filters have many possible realizations which must encompass network requirements such as merit figures, capacity of operating with already deployed systems,

Table 1. Characteristics of some tunable filters.

Filter Category	-3 dB Bandwidth	Tuning Range	Tuning Time	Tuning mechanism
Fiber Fabry-Perot (FFP)	< 0.5 nm	~ 10 nm	ms	PZT
Fiber Bragg Gratings (FBG)	< 0.2 nm	< 10 nm	ms	Thermal
Arrayed Waveguide Grating (AWG)	< 0.2 nm	~ 40 nm	ms	Thermo-optic
Micromachined Fabry-Perot	< 0.5 nm	~ 100 nm	μs	Mechanical
Acusto-Optically Tunable Filter (AOTF)	~ 1 nm	250 nm	μs	Acouto-optic
Electro-optically Tunable Filter (EOTF)	~ 1 nm	~ 20 nm	ns	Electro-optic

wavelength region of operation, fabrication costs, low power consumption, ability of being reconfigured as well as easiness to perform it, and others.

Among the optical tunable filters, those with smallest response time to a tuning excitation are the ones attracting more interest because they would enable a future dynamically varying DWDM network, in which packet switching and wavelength routing will be routine operations. Table 1 summarizes the important characteristics of the various reported technologies [5].

From that table, it can be seen that the electro-optically tunable filter places as one of the fastest response time devices. There is still ongoing research on devices of that category as well as on the competing technologies.

Research activities at Texas A&M University have demonstrated electro-optic tunable filters employing Ti-diffused waveguides in lithium niobate substrate

($Ti:LiNbO_3$). These devices perform optical filtering by using co-directional TE-TM mode conversion. The coupling between these two modes is accomplished by using a phasematched strain-induced overlay grating of a silica (SiO_2), deposited at high temperature and patterned at room temperature. The difference in SiO_2 and $LiNbO_3$ thermal expansion coefficients will guarantee the existence of a strain field, which in turn generates a periodic refractive index grating in the waveguide through the strain-optic effect. By properly choosing the SiO_2 film deposition parameters as well as waveguide fabrication parameters and grating period, the polarization conversion is made efficient.

Recent results showed devices with nanosecond tuning speed and bandwidth of 2.3nm [6-7] for polarization conversion in the 1.55μm wavelength regime. Also, another electro-optic tunable filter, having a narrower bandwidth of 1.56nm was obtained by the use of a longer polarization coupling region [8].

When uniform gratings are used, the polarization conversion efficiency has a well known frequency spectral response which does not present equally spaced nulls and maxima through the optical bandwidth of interest. Making these features appear regularly in the spectrum makes it easier to define channel regions in the communications spectrum and avoid crosstalk between those.

In order to circumvent the problem of unequally spaced nulls and maxima, a new topology of sparse strain gratings was proposed. It is capable of placing the nulls of the spectrum at well known, equally spaced positions, defining channel spectral regions in the stop band and pass band of the filter [9].

The main purpose of this work is to show the viability of making strain-induced polarization conversion filters that employ the sparse grating idea in Titanium diffused Lithium Niobate waveguides ($Ti:LiNbO_3$) to achieve equally spaced nulls for the filter response spectrum in the frequency domain.

In order to provide the background needed to understand the device operation, Chapter II comprehends a theoretical review. Device structure and analysis are presented in Chapter III. Device fabrication details are treated in Chapter IV. Experimental results and discussions are presented in Chapter V and finally, the concluding remarks are made in Chapter VI.

CHAPTER II

THEORETICAL REVIEW

The experimental goal of this work is to develop a device that will perform filtering of guided optical waves. This function will be accomplished by use of a guided optical wave which propagates on an anisotropic substrate, and the most significant phenomena exploited on this structure will be the mode conversion (TE↔TM). The mode conversion will be enabled by a structure positioned on top of the waveguide which in turn will promote a periodic refractive index modulation along the propagation direction. There are basically two ways for promoting this refractive index change on the substrate that is being used ($LiNbO_3$), the first is by using the electro-optical effect and the second by way of the elasto-optical (strain-optic) effect.

Another aspect to be considered is that the desired filtering function must present some special properties, and there is a mathematical tool, called Z-transform, that helps analyze and design this filtering function.

From this brief description, it is devised the need to draw a theoretical review on some subjects that will help the comprehension of how the device works.

The first subject to be treated is propagation of optical waves in anisotropic media, followed by the optical propagation in dielectric waveguides, both based on Maxwell's equations.

Next the Electro-optic Effect and Elasto-optic Effect will be briefly presented, followed by the Coupled Mode Theory and Polarization Mode Conversion.

Last on this chapter, the Z-transform tool applied to the design of optical filters will be outlined.

A. Lightwave Propagation in Anisotropic Media

A medium where the electrical and magnetic properties relevant to an electromagnetic wave do not vary with the direction of propagation of that wave is named isotropic. On the other hand, a medium where those properties change as a result of changing the wave direction of propagation is called anisotropic.

Light as an electromagnetic wave, must have its electric and magnetic fields satisfy Maxwell's equations and the Constitutive Relations. Depending on the medium homogeneity, loss characteristic, presence of sources and isotropy, those equations are modified to accommodate for these characteristics.

Starting with a homogeneous, lossless source-free, linear medium, Maxwell's Equations are expressed by [10]

$$\nabla \times \mathbf{E} = -\frac{\partial \mathbf{B}}{\partial t} \tag{1}$$

$$\nabla \times \mathbf{H} = \frac{\partial \mathbf{D}}{\partial t} \tag{2}$$

$$\nabla \cdot \mathbf{D} = 0 \tag{3}$$

$$\nabla \cdot \mathbf{B} = 0 \tag{4}$$

where **E** (V/m) and **H** (A/m) are electric and magnetic field intensity vectors, respectively; **D** (C/m^2) is the electric displacement (or electric flux density) vector, and **B** (Wb/m^2) is the magnetic flux density (or magnetic displacement) vector.

The relationships between **E** and **D** and between **H** and **B** are called Constitutive Relations and depend on the electric properties and on the magnetic properties of the medium, respectively. In the electric case the relation is mediated by the medium dielectric permittivity ε (F/m) and in the magnetic case by medium magnetic permeability μ (H/m). These relations are expressed by (linear media):

$$\mathbf{D} = \varepsilon_0 \mathbf{E} + \mathbf{P} = \varepsilon_0 (1 + \chi_e) \mathbf{E} = \varepsilon_0 \varepsilon_r \mathbf{E} = \varepsilon \mathbf{E} \tag{5}$$

$$\mathbf{B} = \mu_0 \mathbf{H} + \mu_0 \mathbf{M} = \mu_0 (1 + \chi_m) \mathbf{H} = \mu_0 \mu_r \mathbf{H} = \mu \mathbf{H} \tag{6}$$

where **P** (C/m^2) is the electric polarization vector and **M** (A/m) the magnetization vector; χ_e (dimensionless) the medium electric susceptibility and χ_m (dimensionless) is the medium magnetic susceptibility; ε_0 (F/m) is the free-space (or vacuum) dielectric permittivity and ε_r (dimensionless) is the medium relative permittivity (or dielectric constant); μ_0 is the free-space (or vacuum) magnetic permeability and μ_r (dimensionless) is the medium relative permeability.

The isotropic or anisotropic behavior of a medium is conveyed through the susceptibilities, either electric or magnetic. If the medium is isotropic (electrically or magnetically) the pertinent susceptibility is a scalar. On the other hand, if the medium is anisotropic, that susceptibility must show the dependence of the displacement vector (**D** or **B**) components on field (**E** or **H**) components along different directions. The mathematical entity that establishes that relation is a tensor. Therefore in an anisotropic medium the susceptibility will be a tensor, and for the linear case a second rank tensor,

represented by 3X3 matrices. As a consequence, the permittivity (electric case) or the permeability (magnetic case) will also be a second-rank tensor.

This work deals with non-magnetic dielectric media, for which the magnetic susceptibility vanishes and the medium permeability equals that of the free space (μ_0). In optical media the anisotropic character of electric origin is often times not explicitly stated, but implied in the word anisotropic, since under the magnetic point of view it is isotropic. On the body of this dissertation, when it is said anisotropic it is intended to say electrically anisotropic medium. For this type of media, the constitutive relations (5) and (6) are rewritten as:

$$\mathbf{D} = \varepsilon_0 \mathbf{I}\mathbf{E} + \mathbf{P} = \varepsilon_0 \left(\mathbf{I} + \tilde{\chi}_e\right)\mathbf{E} = \varepsilon_0 \tilde{\varepsilon}_r \mathbf{E} = \tilde{\varepsilon}\mathbf{E} \tag{7}$$

$$\mathbf{B} = \mu_0 \mathbf{H} \tag{8}$$

where **I** is the identity matrix and the electrical susceptibility and the permittivity are typed with the superscript tilde to denote their tensor character:

The medium relative permittivity may be explicitly rewritten in equation (7), giving:

$$\mathbf{D} = \varepsilon_0 \tilde{\varepsilon}_r \mathbf{E} = \begin{pmatrix} \varepsilon_{11} & \varepsilon_{12} & \varepsilon_{13} \\ \varepsilon_{21} & \varepsilon_{22} & \varepsilon_{23} \\ \varepsilon_{31} & \varepsilon_{32} & \varepsilon_{33} \end{pmatrix} \mathbf{E}. \tag{9}$$

In order to simplify the analysis, a convenient reference coordinate system can be chosen to match the orientation of the crystal principal axes, so that all off-diagonal elements of the electric susceptibility tensor vanish.

In this new coordinate system, equation (9) is rewritten:

$$\mathbf{D} = \varepsilon_0 \widetilde{\varepsilon}_r \mathbf{E} = \begin{pmatrix} \varepsilon_{11} & 0 & 0 \\ 0 & \varepsilon_{22} & 0 \\ 0 & 0 & \varepsilon_{33} \end{pmatrix} \mathbf{E} \tag{10}$$

where ε_{11}, ε_{22} and ε_{33} are called principal permittivities of the medium.

In order to draw some facts about light propagation in anisotropic media, it will be assumed the simplifications of infinite media and plane wave propagation.

Initially assuming plane wave propagation for $\mathbf{D}$ and $\mathbf{H}$, they should be expressed as

$$\mathbf{D}(r,t) = \mathbf{D}\, e^{j(\omega t - \mathbf{k}\cdot\mathbf{r})} \tag{11}$$

and

$$\mathbf{H}(r,t) = \mathbf{H}\, e^{j(\omega t - \mathbf{k}\cdot\mathbf{r})} \tag{12}$$

where $\mathbf{k}$ is the wave propagation vector.

Substituting equations (11) and (12) in equation (2) (Ampère-Maxwell equation) and taking into account vector identity $\nabla \times (\phi \mathbf{A}) = (\nabla \phi) \times \mathbf{A} + \phi(\nabla \times \mathbf{A})$, it is obtained

$$-\mathbf{k} \times \mathbf{H} = \omega \mathbf{D}. \tag{13}$$

Acting similarly with equation (1) (Faraday-Maxwell equation), it is obtained

$$\mathbf{k} \times \mathbf{E} = \omega \mu_0 \mathbf{H}. \tag{14}$$

Recall that

$$\mathbf{k} = \frac{\omega}{v_p} \hat{\mathbf{k}} \tag{15}$$

where v_p is the optical wave phase velocity and $\hat{\mathbf{k}}$ is the unit vector along the propagation direction.

Solving equation (14) for **H** and substituting into equation (13) and taking equation (15) into account

$$\mathbf{D} = -\frac{1}{\mu_0 v_p^2}\left[\hat{\mathbf{k}} \times \left(\hat{\mathbf{k}} \times \mathbf{E}\right)\right]. \tag{16}$$

By using the vector identity $\mathbf{A} \times \mathbf{B} \times \mathbf{C} = \mathbf{B}(\mathbf{A} \cdot \mathbf{C}) - \mathbf{C}(\mathbf{A} \cdot \mathbf{B})$, equation (16) may be rewritten as

$$\mathbf{D} = \frac{1}{\mu_0 v_p^2}\left[\mathbf{E} - \hat{\mathbf{k}}\left(\hat{\mathbf{k}} \cdot \mathbf{E}\right)\right]. \tag{17}$$

Taking into account the constitutive relation expressed by equation (10), also considering the vector components along each crystalline axis, it is obtained from equation (17)

$$\underbrace{\begin{pmatrix} 1-k_1^2-\mu_0\varepsilon_{11}v_p^2 & -k_1k_2 & -k_1k_3 \\ -k_1k_2 & 1-k_2^2-\mu_0\varepsilon_{22}v_p^2 & -k_2k_3 \\ -k_1k_3 & -k_2k_3 & 1-k_3^2-\mu_0\varepsilon_{33}v_p^2 \end{pmatrix}}_{\mathbf{K}} \begin{pmatrix} E_1 \\ E_2 \\ E_3 \end{pmatrix} = 0\,. \tag{18}$$

In order for the homogeneous system expressed by equation (18) to exhibit non-trivial solutions $\det \mathbf{K} = \mathbf{0}$. By imposing that condition and after some manipulation it is obtained

$$\frac{k_1^2}{v_p^2 - 1/\mu_0\varepsilon_{11}} + \frac{k_2^2}{v_p^2 - 1/\mu_0\varepsilon_{22}} + \frac{k_3^2}{v_p^2 - 1/\mu_0\varepsilon_{33}} = 0\,. \tag{19}$$

Equation (19) is known as Fresnel equation of wave normals. Once a direction of propagation is chosen (k_1, k_2, k_3) it can be reduced to an equation in the format

$$v_p^4 - Bv_p^2 + C = 0\,. \tag{20}$$

Equation (20) is a biquadratic equation in v_p which will have two solutions. Each solution can then be substituted in equation (18) and the field components associated to each phase velocity be found. Therefore, for each chosen direction in an electrically anisotropic medium, there will be two allowed propagating solutions.

It is also possible to draw some information about the solutions' field orientation, or the polarization state.

Considering equation (13) one concludes that

$$\mathbf{k}\cdot\mathbf{D} = \mathbf{0}\,. \tag{21}$$

Because the vector product between $\mathbf{k}$ and $\mathbf{H}$ is orthogonal to the plane formed by those vectors. This relation holds for both solutions.

Also equation (17) must hold for each individual solution.

$$\mathbf{D}^{(1)} = \frac{1}{\mu_0 v_{p1}^2}\left[\mathbf{E}^{(1)} - \hat{\mathbf{k}}\left(\hat{\mathbf{k}}\cdot\mathbf{E}^{(1)}\right)\right] \tag{22}$$

$$\mathbf{D}^{(2)} = \frac{1}{\mu_0 v_{p2}^2}\left[\mathbf{E}^{(2)} - \hat{\mathbf{k}}\left(\hat{\mathbf{k}}\cdot\mathbf{E}^{(2)}\right)\right] \tag{23}$$

where the numerical superscripts and subscripts were used to explicitly denote one solution of the possible two.

Taking the dot product of equation (22) by $\mathbf{D}^{(2)}$, the dot product of equation (23) by $\mathbf{D}^{(1)}$, subtracting one from the other, and also considering equation (21), follows

$$\mathbf{D}^{(2)} \cdot \mathbf{D}^{(1)} \left(\mu_0 v_{p2}^2 - \mu_0 v_{p1}^2 \right) = \mathbf{E}^{(2)} \cdot \mathbf{D}^{(1)} - \mathbf{E}^{(1)} \cdot \mathbf{D}^{(2)} . \tag{24}$$

Now focusing on the right-hand side of equation (24) and recalling equation (9)

$$\mathbf{E}^{(2)} \cdot \mathbf{D}^{(1)} - \mathbf{E}^{(1)} \cdot \mathbf{D}^{(2)} = \sum_{i=1}^{3} \sum_{j=1}^{3} E_i^{(2)} \varepsilon_{ij} E_j^{(1)} - \sum_{k=1}^{3} \sum_{l=1}^{3} E_k^{(1)} \varepsilon_{kl} E_l^{(2)} . \tag{25}$$

From the symmetry properties of the dielectric tensor associated with a lossless medium $\varepsilon_{ij} = \varepsilon_{ji}$ [11]. Therefore the right-hand side of equation (25) vanishes, as well as the right-hand side of equation (24). Since the solutions are not degenerate, i.e. $v_{p1} \neq v_{p2}$, $\mathbf{D}^{(1)}$ and $\mathbf{D}^{(2)}$ must be orthogonal to each other. Explicitly

$$\mathbf{D}^{(2)} \cdot \mathbf{D}^{(1)} = 0 . \tag{26}$$

Summarizing, there are two possible solutions of an electromagnetic wave propagating along a certain direction in an electrically anisotropic medium. They propagate at different velocities, given by Fresnel equation of wave normals, and present electric displacement vectors orthogonal to the direction of propagation, and orthogonal to each other.

Therefore the procedure for determining the solutions to equation (17), once the propagation direction is chosen, is to find solutions to the Fresnel equation of wave normals and then substitute each obtained value for phase velocity back in equation (17) in order to find field components.

There is a quicker graphic way of visualizing the solutions field orientations that also enables determining refractive indices associated to each propagating solution. The geometrical construction needed for this method is called the index ellipsoid.

The starting point is analyzing the stored electric energy density of the propagating wave in the anisotropic medium, given by

$$U_e = \frac{1}{2}\mathbf{E}\cdot\mathbf{D}. \tag{27}$$

Combining equations (10) and (27)

$$U_e = \frac{1}{2}\left[\frac{D_x^2}{\varepsilon_{11}} + \frac{D_y^2}{\varepsilon_{22}} + \frac{D_z^2}{\varepsilon_{33}}\right]. \tag{28}$$

Defining $x = D_x / \sqrt{2\varepsilon_0 U_e}$, $y = D_y / \sqrt{2\varepsilon_0 U_e}$ and $z = D_z / \sqrt{2\varepsilon_0 U_e}$ equation (28) becomes

$$\frac{x^2}{\varepsilon_{r11}} + \frac{y^2}{\varepsilon_{r22}} + \frac{z^2}{\varepsilon_{r33}} = 1. \tag{29}$$

In optics it is usual to implicitly refer to propagation velocities by means of the refractive index. Defined as

$$n = \frac{c}{v_p} = \frac{\sqrt{\mu_0 \varepsilon}}{\sqrt{\mu_0 \varepsilon_0}} = \sqrt{\varepsilon_r} \tag{30}$$

where ε is the permittivity "seen" by one specific solution and ε_r is the relative value associated with it.

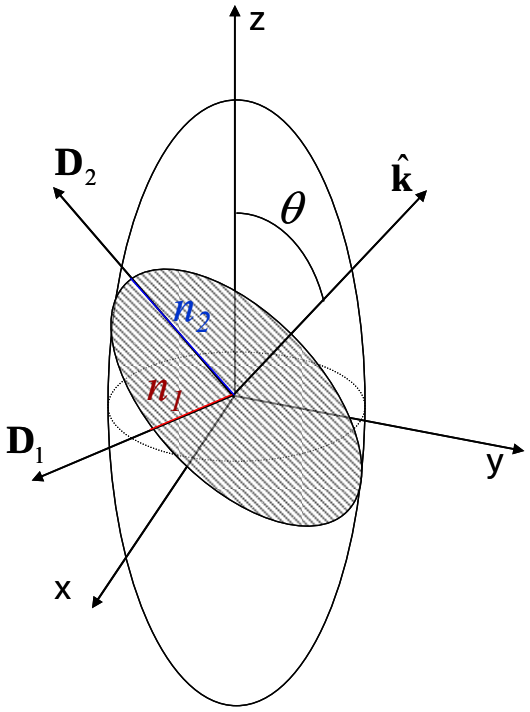

Fig. 2. The index ellipsoid.

Keeping this in mind, equation (10), may be modified to

$$\mathbf{D} = \varepsilon_0 \tilde{\varepsilon}_r \mathbf{E} = \varepsilon_0 \begin{pmatrix} n_x^2 & 0 & 0 \\ 0 & n_y^2 & 0 \\ 0 & 0 & n_z^2 \end{pmatrix} \mathbf{E} \quad . \tag{31}$$

Also equation (29) may be modified to

$$\frac{x^2}{n_x^2} + \frac{y^2}{n_y^2} + \frac{z^2}{n_z^2} = 1 \quad . \tag{32}$$

Equation (32) is the equation of an ellipsoid and is known as the index ellipsoid or optical indicatrix [11].

Figure 2 shows a representation of the index ellipsoid along with electric displacement vectors orientation for both solutions ($\mathbf{D}_1$ and $\mathbf{D}_2$) and the direction of propagation $\hat{\mathbf{k}}$.

To determine the refractive indices associated with an arbitrary direction of propagation $\hat{\mathbf{k}}$, the intersection of the plane orthogonal to $\hat{\mathbf{k}}$ with the index ellipsoid and containing the origin is taken. This intersection is an ellipse, shaded in Fig. 2. The two allowed orthogonal polarizations ($\mathbf{D}_1$ and $\mathbf{D}_2$) coincide with the major and minor axes of the ellipse. The shaded ellipse semi-axes lengths are the refractive indices "seen" by the solution which has its electric displacement vector aligned with the respective semi-axis.

According to how the principal refractive indices (dielectric permittivities) relate to each other, the medium to which they relate receives a different denomination. If $n_x \neq n_y \neq n_z$ ($\varepsilon_{11} \neq \varepsilon_{22} \neq \varepsilon_{33}$), the medium is said to be biaxial. This nomenclature comes from the fact that there are two directions in the medium along which both solutions propagate with the same refractive index (degenerate propagation velocities).

On the other hand, if $n_x = n_y \neq n_z$ ($\varepsilon_{11} = \varepsilon_{22} \neq \varepsilon_{33}$), the medium is said to be uniaxial, and for this type of medium there is only one direction along which both solutions propagate with the same refractive index. This direction is called the crystal optic axis and by convention the crystalline z axis is always chosen to be aligned along this direction. This is the case of Lithium Niobate ($LiNbO_3$), the material used as substrate in this work.

In Figure 2, for a uniaxial crystal, there is an axial symmetry along z, therefore, one propagation mode always "sees" the same refractive index (n_1), because the semi-axis contained in the xy plane is bound by a circle. This one is called the ordinary refractive index, denoted n_o, and the solution associated to it ordinary wave. The other refractive index obtained from the semi-axis out of the xy plane (n_2) will have its value dependent on the propagation vector orientation with respect to the optic axis (θ). This latter is called extraordinary refractive index, denoted n_e, and the solution associated to it extraordinary wave. Equation (32) may be rewritten as

$$\frac{x^2}{n_o^2}+\frac{y^2}{n_o^2}+\frac{z^2}{n_e^2}=1 \ . \tag{33}$$

Also from Fig.2 the relationship between the refractive index dependent on θ (major semi-axis length) and lengths along coordinated axes are deduced as

$$\begin{aligned} x &= 0 \\ y &= n_e(\theta)\cos\theta \\ z &= n_e(\theta)\sin\theta \ . \end{aligned} \tag{34}$$

Substituting equation (34) into equation (33) and solving for $n_e(\theta)$ yields

$$n_e(\theta)=\frac{n_o n_e}{\sqrt{n_e^2\cos^2\theta+n_o^2\sin^2\theta}} \ . \tag{35}$$

B. Optical Waveguides

In order to explain guided light propagation in dielectric waveguides the so called Slab (planar) waveguide model will be considered. This model assumes the simplification of invariance of the field along one of the directions transversal to the

propagation. The invariance comes as a consequence of the infinite transverse dimension along said axis. Also the refractive index in each one of the structure layers is assumed invariant with position or direction (homogeneous and isotropic).

In actual devices this behavior may be mimicked when one of the dimensions transverse to the propagation is much larger than the other. Although this is not the more frequent case, the model provides important insights about properties of guiding structures and about properties of guided solutions of the wave equation.

The geometry considered in this analysis is outlined in figure 3. It is assumed three regions, each with a distinct refractive index. Region 1 has refractive index n_c and is often called cover layer. Region 2 has refractive index n_f, has a thickness t and is called film or guiding layer. Region 3 has refractive index n_s and is called substrate.

Also in figure 3, a reference coordinate system is adopted for the analysis. The y dimension is the one assumed infinite. Propagation happens along z direction.

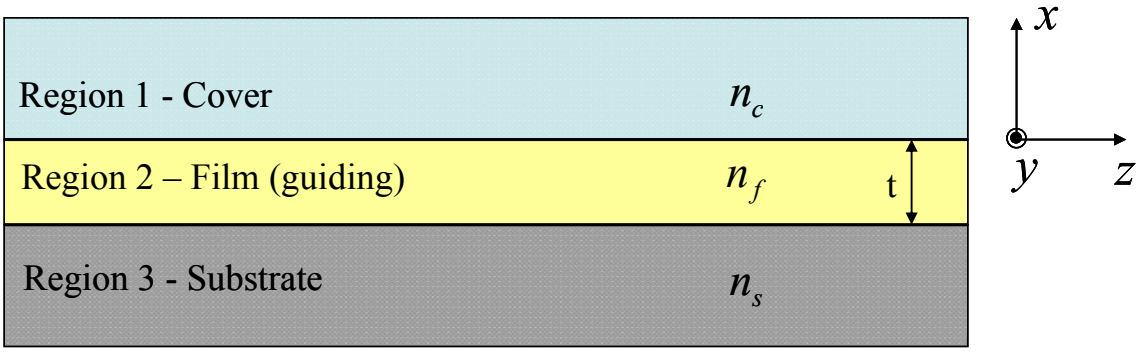

Fig. 3. Schematic diagram of a dielectric slab waveguide.

The procedure to derive wave equation using Maxwell equations is the standard. Take the curl of equation (1); use the vector identity $\nabla\times\nabla\times\mathbf{A}=\nabla(\nabla\cdot\mathbf{A})-\nabla^2\mathbf{A}$; assume electrically and magnetically isotropic and homogeneous medium (constant scalar permittivity and permeability) , so that equation (3) may be used in conjunction with the electric constitutive relation to yield $\nabla\cdot\mathbf{E}=\mathbf{0}$ and obtain

$$-\nabla^2\mathbf{E}=-\mu_0\frac{\partial}{\partial t}(\nabla\times\mathbf{H}). \tag{36}$$

Use equation (2) to substitute the expression for $\nabla\times\mathbf{H}$ in equation (36) and get

$$\nabla^2\mathbf{E}-\mu_0\varepsilon\frac{\partial^2\mathbf{E}}{\partial t^2}=0. \tag{37}$$

Equation (37) is know as time domain wave equation for the electric field.

In order to further the analysis, assume time harmonic variation for the electric field and propagation along z with propagation constant β, i.e.

$$\mathbf{E}(r,t)=\mathbf{E}(x,y)\,e^{j(\omega t-\beta z)}. \tag{38}$$

In rectangular coordinates, $\nabla^2=\partial^2/\partial x^2+\partial^2/\partial y^2+\partial^2/\partial z^2$. Taking into account the proposed structure, $\partial/\partial y=0$, because it is infinite along y direction. Considering also the field variation in equation (38), $\partial^2/\partial z^2=-\beta^2$, and equation (37) becomes[11-12]:

$$\frac{d^2\mathbf{E}(x)}{dx^2}+\left(\omega^2\mu_0\varepsilon-\beta^2\right)\mathbf{E}(x)=0. \tag{39}$$

Consider the identity

$$k=n\frac{\omega}{c_0}=n\omega\sqrt{\mu_0\varepsilon_0}=nk_0 \tag{40}$$

where k is plane wave propagation constant the in a medium with refractive index n and k_0 is the free space (vacuum) plane wave propagation constant.

Equation (39) with the use of equation (40), becomes

$$\frac{d^2\mathbf{E}(x)}{dx^2} + \left(k_0^2 n^2 - \beta^2\right)\mathbf{E}(x) = 0\,. \tag{41}$$

The fields in each particular region of the structure must satisfy equation (41), only the respective refractive index should be substituted in that equation. The solutions in each of the three regions must not depart from the solution on other regions as the wave propagates, because it would disrupt the total solution as a propagating mode, hence they must have the same propagation constant β. With that in mind, equation (41), becomes a system of simultaneous equations, written as

$$\begin{aligned}
&\text{for Region 1}: \frac{d^2\mathbf{E}(x)}{dx^2} + \left(k_0^2 n_c^2 - \beta^2\right)\mathbf{E}(x) = 0 \\
&\text{for Region 2}: \frac{d^2\mathbf{E}(x)}{dx^2} + \left(k_0^2 n_f^2 - \beta^2\right)\mathbf{E}(x) = 0 \\
&\text{for Region 3}: \frac{d^2\mathbf{E}(x)}{dx^2} + \left(k_0^2 n_s^2 - \beta^2\right)\mathbf{E}(x) = 0\ .
\end{aligned} \tag{42}$$

Still aiming at matching solutions in the three regions in order to constitute a complete solution for the proposed structure, the fields must satisfy the boundary conditions at the interfaces between each pair of media. More specifically, at the boundary between the two dielectric media, the tangential components of electric and magnetic fields, $\mathbf{E}$ and $\mathbf{H}$ respectively**;** and the normal components of electric and magnetic flux densities, $\mathbf{D}$ and $\mathbf{B}$ respectively, must all be continuous.

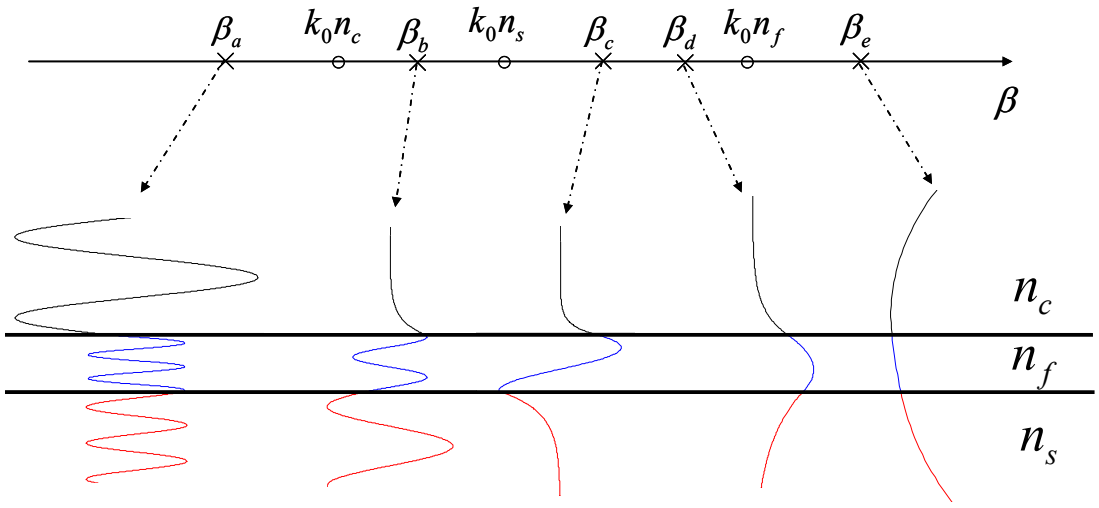

Fig. 4. Electric field distributions of a three-layer dielectric slab waveguide as a function of varying propagation constant β.

Assuming the relationship between the refractive indices in the three regions is $n_f > n_s > n_c$, the solution to equation (42) in each region can be classified as either oscillatory or exponential in nature, depending on the value of the propagation constant β.

If $\beta < k_0 n_c$, the solutions to equations (42) are sinusoidally oscillating in every region. For this case there is no confined or guided energy in any of the three layers. This is called a radiation solution (case "a" in figure 4).

If $k_0 n_c < \beta < k_o n_s$, the solution will be exponentially decaying in the cover and sinusoidal in the film and substrate. This is called a substrate radiation solution (case "b" in figure 4).

If $k_0 n_s < \beta < k_0 n_f$, the solution will be exponentially decaying in the cover and substrate, and sinusoidally oscillatory in the film layer. This is called a confined or guided mode (cases "c" and "d" in figure 4). By observing those cases in figure 4, it is possible to conclude that a great part of the electromagnetic field is confined to the film layer (Region 2), which presents the highest refractive index. Each value of β (eigenvalue) will be associated to a vector field distribution (eigenvector) and receives the denomination "mode". There is a minimum value β may have, called cutoff, because below it the light starts leaking into the substrate and there cannot be propagating modes anymore. As a rule of thumb, this value can be assumed equal to $k_0 n_s$. This is the case only for symmetric slab waveguides, i.e. the film layer is sandwiched between identical layers ($n_c = n_s$).

The last case left to analyze is when $\beta > k_0 n_f$. For this one, the solution will behave exponentially increasing, constituting a physically unrealistic one (infinitely increasing energy).

Once the thickness of the film layer is chosen, the slab dielectric waveguide can only support a finite number of guided modes. Those modes are classified according to the presence of field components along the propagation direction. They are divided into two groups of mutually orthogonal polarization states. In one class of modes the electric field is completely transverse to the propagation direction and is called transverse electric or simply TE mode. Using the same coordinate system orientation adopted in figure 3, the field components present on this solution are E_y, H_x and H_z (no E_z). In the other

class the magnetic field is the one completely transverse to the propagation direction. This latter is called the transverse magnetic or simply TM mode and the field components present on this solution are H_y, E_x and E_z (no H_z).

Focusing on the TE mode

$$\mathbf{E}(x,t) = E_y(x)e^{j(\omega t-\beta z)}\,\hat{y} \tag{43}$$

$$H_x = -\frac{\beta}{\omega\mu_0}E_y \tag{44}$$

$$H_z = -\frac{1}{j\omega\mu_0}\frac{\partial E_y}{\partial x} \quad . \tag{45}$$

Closed-form expressions for the y-component of the electric field (E_y) are obtained by substituting equation (43) in equations (42), solving it recalling that a guided mode will have exponentially decaying behavior outside the guiding layer and sinusoidal behavior in the guiding layer. Next, the tangential components of the electric and magnetic field (E_y and H_z) at the interfaces ($x = 0$ and $x = -t$) should be forced to be continuous (Boundary conditions), yielding:

$$E_y(x) = \begin{cases} Ae^{-qx} & \text{for } x > 0 \quad \text{(Cover)} \\ A\left[\cos(hx) - {}^{q}\!/_{h}\sin(hx)\right] & \text{for } -t < x \le 0 \text{ (Film)} \\ A\left[\cos(ht) + {}^{q}\!/_{h}\sin(ht)\right]e^{p(x+t)} & \text{for } x \le -t \quad \text{(Substrate)} \end{cases} \tag{46}$$

where A is an arbitrary constant, t is the film layer thickness, $q = \sqrt{\beta^2 - k_0^2 n_c^2}$, $h = \sqrt{k_0^2 n_f^2 - \beta^2}$, $q = \sqrt{\beta^2 - k_0^2 n_s^2}$.

Equation (45) is determined using only three of the four boundary conditions. The last boundary condition, which establishes the continuity of the tangential magnetic field (H_z) at the interface $x = -t$ yields:

$$\tan(ht) = \frac{p+q}{h - \frac{pq}{h}} \quad . \tag{47}$$

By solving equation (47) it is found the discrete values of h , and as a consequence of β , for which TE mode propagation is allowed in the structure. Equation (47) is called dispersion equation for the TE mode. Other denominations like characteristic equation or eigenvalue equation are also used.

Now focusing on the TM mode, the field components are expressed as:

$$\mathbf{H}(x,t) = H_y(x) e^{j(\omega t - \beta z)} \, \hat{y} \tag{48}$$

$$E_x = -\frac{\beta}{\omega \varepsilon_0 n^2} H_y \tag{49}$$

$$E_z = -\frac{1}{j\omega \varepsilon_0 n^2} \frac{\partial H_y}{\partial x} \quad . \tag{50}$$

Adopting a procedure similar to the one used in deriving equation (46) by substituting equation (48) in equation (42) and applying boundary conditions at the interfaces, expressions for the transversal magnetic field (H_y) identical to the ones obtained for E_y in the TE case (equation (46)) are obtained. Explicitly

$$H_y(x) = \begin{cases} Be^{-qx} & \text{for } x > 0 \quad \text{(Cover)} \\ B\left[\cos(hx) - \frac{q}{h}\sin(hx)\right] & \text{for } -t < x \le 0 \text{ (Film)} \\ B\left[\cos(ht) + \frac{q}{h}\sin(ht)\right]e^{p(x+t)} & \text{for } x \le -t \quad \text{(Substrate)} \end{cases} \tag{51}$$

where B is the arbitrary amplitude constant and h, p and q are defined the same way.

Similarly, by applying the last boundary condition, the dispersion equation that governs allowed values of h for the TM modes is obtained:

$$\tan(ht) = \frac{\left(\frac{n_f}{n_s}\right)^2 p + \left(\frac{n_f}{n_c}\right)^2 q}{h - \left(\frac{n_f^2}{n_s n_c}\right)\frac{pq}{h}} \quad . \tag{52}$$

Although the dielectric slab waveguide is not suitable for applications where functions of light filtering, modulation and switching are desired, it provides a framework for the comprehension of the basic concept guidance and the requirement of an increased refractive index layer to accomplish it. Along with that it also provides the concept of a guided mode and that the dispersion equation can only be satisfied by a discrete set of values of the propagation constant.

More realistic devices would have also to consider that light is also confined in the other transversal dimension, or the y direction, in addition to the considered confinement in depth assumed in the slab model. These devices are called rectangular or 3-D dielectric waveguides.

In contrast to what happens with microwave rectangular-wall waveguides, in which pure TE and TM modes can be supported because of the boundary conditions satisfied by the fields at perfect conductor walls; in rectangular dielectric-only waveguides there are no pure TE and TM modes.

Instead, there are two families of hybrid modes, classified according to the field direction of polarization. The modes are referred as TE-like, because the electric field is aligned along the y direction; or as TM-like, because the electric field is aligned along the x direction, in direct correspondence to what happens with the slab modes. Closed-form analytical expressions for the fields cannot be obtained unless approximations are assumed, although numerical solutions can be obtained by using dedicated software in a digital computer.

Among the methods assuming approximations there are the Marcatili's [13] and the effective index method [14].

In the Marcatili's Method the modes are assumed well confined and far from cutoff. The nomenclature for the regions, refractive indices, coordinate system convention as well as important dimensions are shown in figure 5. Most of the power, hence the fields, is confined to region I , and small amount of power travel outside. The fields in regions *II*, *III*, *IV* and *V* decay exponentially, based on the knowledge gained in the slab waveguide. The amount of power traveling in the four shaded areas is neglected.

This simplification is the source of errors in the method, which are acceptable in well confined and far from cutoff analysis.

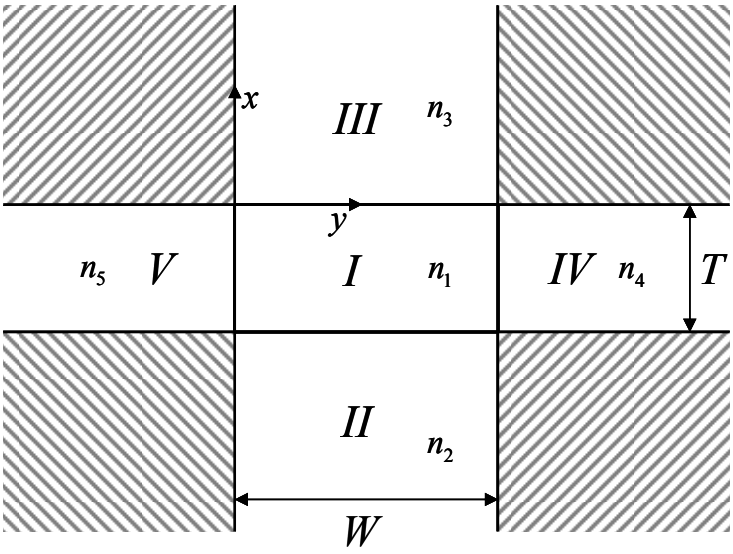

Fig. 5. Cross-section of a generalized structure used in Marcatili's Method.

The wave equation for longitudinal components can then be solved by separation of variables and closed-form expressions for the field in all five regions can be determined. Solutions are named after the field polarization. TE polarization will present $E_x = 0$, and transversal electric field aligned along y direction. TM polarization will present $H_x = 0$, and transversal magnetic field aligned along y direction. Dispersion equations and field amplitudes are obtained from application of boundary conditions at the interfaces ($x = 0, x = -T, y = 0, y = W$). By direct inspection of the dispersion equations and field expressions it is noticed that the transversal component of electric field in the TE solution (E_y) behaves along the x direction like a slab TE mode in a structure of film thickness T and along the y direction like a slab TM mode in a structure of thickness W . Likewise, the transversal component of electric field in the TM

solution (E_x) behaves along the y direction like a slab TE mode in a structure of film thickness W; and along the x direction like a slab TM mode in a structure of thickness T.

The perception of this fact allied with the knowledge of the solution for the fields and dispersion equations of the slab waveguide model enables to write solutions for the fields in a rectangular dielectric waveguide almost by inspection. That alone shows the importance of the studying slab waveguides, even though they do not represent frequently used devices.

The Effective Index Method makes use of this perceived fact to improve Marcatili's Method range of validity (including close to cutoff modes). The structure is divided into two other structures: one obtained by stretching the guiding layer along its longer dimension and the other obtained by stretching the guiding layer along its shorter dimension. For the first structure, calculate the mode effective index, given by $n_{eff1} = \beta / k_0$. For the second structure, instead of using the actual value of the guiding region refractive index as the guiding layer refractive index, use the obtained value of n_{eff1} in its place, keeping actual values of surrounding refractive indices. The resulting value of β after this second step is closer to the actual value in almost cutoff modes.

Up to now, only homogenous refractive indices in guiding and surrounding regions were assumed. This is another simplification in the dielectric waveguide analysis. More realistic approach would have to consider varying refractive index, even maybe an arbitrary refractive index profile. It can be found in the literature analyses that

treat the problem of diffused waveguides in planar geometry (slab) [15] and rectangular geometry [16].

Today there are many software packages for waveguide analysis that allow the guiding region to show arbitrary refractive index profiles. They are also based on some approximations and sometimes even on the simplified analytic solution. Therefore the knowledge of those methods helps understanding the software limitations or even developing your own software. The basic concepts presented up to this point suffice to understand the behavior of a diffused channel waveguide mode and a more profound analysis would be out of the scope of this dissertation.

Throughout this work, single mode propagation in waveguide is pursued. Only the lowest order (called fundamental) mode for each polarization is allowed to propagate.

C. Linear Electro-Optic (Pockels) Effect

In certain types of crystals the application of an electric field changes the orientation and semi-axes lengths of the index ellipsoid, therefore the name electro-optic effect. The linear electro-optic (or Pockels) effect is the one under which the relationship between applied electric field and the optical change is linear. There is also the Kerr effect in which the relationship between the optical property and the applied electric field is quadratic. Other nonlinear (higher order) electro-optic effects do exist, but the change they promote on a medium is very small and because of that are almost always neglected. The Pockels effect is the strongest among the electro-optical and is the most commonly used for light control in integrated optical devices.

The approach followed to present the electro-optic effect will be a phenomenological one. The deformation suffered by the index ellipsoid as a result of an applied electric field will be quantified and related to the index ellipsoid with no field applied.

Instead of approaching the problem through the permittivity tensor, it is common in the literature to do so by using the impermeability tensor, defined as

$$\eta = \varepsilon^{-1}. \tag{53}$$

The deformation in the index ellipsoid is then expressed as a variation in the impermeability sensor as

$$\eta(E \neq 0) = \eta(E = 0) + \Delta\eta(E). \tag{54}$$

Recall that equation (32) is the representation of the index ellipsoid when the crystallographic principal axes are aligned with the reference coordinate system.

Rewriting equation (32) in terms of the impermeability tensor gives

$$\eta_{11}x^2 + \eta_{22}y^2 + \eta_{33}z^2 = 1 \tag{55}$$

where $\eta_{11} = 1/n_x^2$, $\eta_{22} = 1/n_y^2$ and $\eta_{33} = 1/n_z^2$

When the principal axes are no longer aligned with this system, off diagonal terms in the dielectric permittivity tensor will appear and the equation of the index ellipsoid, now arbitrarily oriented in space, will be given by [17]:

$$\eta'_{11}x^2 + \eta'_{22}y^2 + \eta'_{33}z^2 + 2\eta'_{23}yz + 2\eta'_{13}xz + 2\eta'_{12}xy = 1 \tag{56}$$

where $\eta'_{ij} = 1/n_{ij}^2$ with $i, j = 1, 2, 3$

The induced relative impermeability change due to an applied electric field is expressed as

$$\Delta\eta_{ij} = \sum_{k=1}^{3} r_{ijk} E_k \tag{57}$$

where r_{ijk} is the electro-optic coefficient tensor.

Due to the impermeability tensor being symmetric, like the permittivity tensor, there are only six independent values of the impermeability tensor components. This fact enables a contracted index notation to be used in equation (57) and the electro-optic coefficient tensor be represented by a 3X6 matrix. The indices ij are changed according to

$$\begin{aligned} 11 &\rightarrow 1 & 23 &\rightarrow 4 \\ 22 &\rightarrow 2 & 13 &\rightarrow 5 \\ 33 &\rightarrow 3 & 12 &\rightarrow 6 \end{aligned}$$

Equation (57) is then explicitly rewritten

$$\begin{pmatrix} \Delta\eta_1 \\ \Delta\eta_2 \\ \Delta\eta_3 \\ \Delta\eta_4 \\ \Delta\eta_5 \\ \Delta\eta_6 \end{pmatrix} = \begin{pmatrix} r_{11} & r_{12} & r_{13} \\ r_{21} & r_{22} & r_{23} \\ r_{31} & r_{32} & r_{33} \\ r_{41} & r_{42} & r_{43} \\ r_{51} & r_{52} & r_{53} \\ r_{61} & r_{62} & r_{63} \end{pmatrix} \begin{pmatrix} E_1 \\ E_2 \\ E_3 \end{pmatrix} . \tag{58}$$

Lithium Niobate ($LiNbO_3$) belongs to a crystal symmetry class called trigonal 3m for which the electro-optic coefficient tensor has the format

$$\begin{pmatrix} 0 & -r_{22} & r_{13} \\ 0 & r_{22} & r_{13} \\ 0 & 0 & r_{33} \\ 0 & r_{51} & 0 \\ r_{51} & 0 & 0 \\ -r_{22} & 0 & 0 \end{pmatrix} . \tag{59}$$

The values of the electro-optic coefficients for $LiNbO_3$ at various wavelengths are tabulated in the literature. The largest is r_{33} , closely followed by r_{51} ; r_{13} and r_{22} are typically much smaller than them. They are on the order of 10^{-12} to 10^{-11} m/V. For the sake of an example $r_{33} = 30.8\times10^{-12}$ m/V, $r_{51} = 26\times10^{-12}$ m/V, $r_{13} = 8.6\times10^{-12}$ m/V and $r_{22} = 3.4\times10^{-12}$ m/V at the He-Ne red laser emission wavelength ($\lambda = 632.8$ nm).

Analyzing the case in which an electric field applied to $LiNbO_3$ is aligned along the z is direction, by use of equations (56), (58) and (59), the new index ellipsoid equation becomes

$$\left(\frac{1}{n_o^2} + r_{13}E_z\right)x^2 + \left(\frac{1}{n_o^2} + r_{13}E_z\right)y^2 + \left(\frac{1}{n_e^2} + r_{33}E_z\right)z^2 = 1 \ . \tag{60}$$

There are no crossed-product terms, therefore, the index ellipsoid was not rotated, only the axes were elongated. The new refractive indices along the principal axes are related to the previous ones by:

$$\begin{aligned} \frac{1}{n_x^2} &= \frac{1}{n_o^2} + r_{13}E_z \\ \frac{1}{n_y^2} &= \frac{1}{n_o^2} + r_{13}E_z \\ \frac{1}{n_z^2} &= \frac{1}{n_e^2} + r_{33}E_z \quad . \end{aligned} \tag{61}$$

Solving for the refractive indices and using the small argument binomial expansion, the new values for the refractive indices (index ellipsoid semi-axes length) are

$$\begin{aligned} n_x &= n_o + \frac{1}{2} n_o^3 r_{13} E_z \\ n_y &= n_o + \frac{1}{2} n_o^3 r_{13} E_z \\ n_z &= n_e + \frac{1}{2} n_e^3 r_{33} E_z \quad . \end{aligned} \tag{62}$$

This is one of the most common orientation of the modulating electric field in $LiNbO_3$ waveguides.

D. Photoelastic (Strain-Optic) Effect

The approach used to describe the photoelastic effect will be similar to the one used in describing the electro-optic effect, i.e. a phenomenological one, based on the deformation induced in the index ellipsoid caused by a mechanical deformation.

The photoelastic effect couples the mechanical strain that results from a mechanical deformation to changes in the impermeability tensor, hence to changes in the refractive indices. This effect is described by

$$\Delta \eta_{ij} = \sum_{k=1}^{3} \sum_{l=1}^{3} p_{ijkl} S_{kl} \tag{63}$$

where $\Delta \eta_{ij}$ is the variation in the impermeability tensor, p_{ijkl} is the strain-optic tensor and S_{kl} is the strain tensor.

Every elastic continuous solid body that suffers the action of a stress undergoes a mechanical deformation which in turn induces a strain. The parameter that relates the

strain to the stress is the mechanical compliance through the well known Hooke's Law. With a strain within the elastic limits of the material from which the body is composed, the strain tensor will present nine components defined as

$$S_{ij} = \frac{1}{2}\left(\frac{\partial u_i}{\partial x_j} + \frac{\partial u_j}{\partial x_i} \right) \tag{64}$$

where u_i is the component of a deformation vector **u** along the direction of the coordinate x_i.

The strain components along the diagonal of the strain tensor ($i = j$) are called principal strains and the off-diagonal components ($i \neq j$) are called shear strains. The principal strains are related to deformations components oriented in the same direction as the stress that generated them, whereas shear strains are related to deformations components coupled to directions other than the direction where the stress that generated them is applied.

By direct inspection of equation (64), the symmetry property of the strain tensor may be noticed. There are only 6 independent components, allowing this tensor to be represented by a 6 X 1 matrix, using the same contracted index notation adopted in the previous section for the impermeability tensor.

The symmetry of the impermeability tensor and of the strain tensor forces the strain-optic (p_{ijkl}) tensor to also exhibit symmetry properties. Since the impermeability tensor and the strain tensor are represented by 6 X 1 matrices, the strain-optic tensor must be represented by a 6 X 6 matrix. In this contracted index notation, equation (63) becomes

$$\Delta\eta_i = \sum_{j=1}^{6} p_{ij} S_j \,. \tag{65}$$

For crystals of the symmetry class $3m$, to which $LiNbO_3$ belongs, equation (65) may written as

$$\begin{pmatrix} \Delta\eta_1 \\ \Delta\eta_2 \\ \Delta\eta_3 \\ \Delta\eta_4 \\ \Delta\eta_5 \\ \Delta\eta_6 \end{pmatrix} = \begin{pmatrix} p_{11} & p_{12} & p_{13} & p_{14} & 0 & 0 \\ p_{12} & p_{11} & p_{13} & -p_{14} & 0 & 0 \\ p_{31} & p_{31} & p_{33} & 0 & 0 & 0 \\ p_{41} & -p_{41} & 0 & p_{44} & 0 & 0 \\ 0 & 0 & 0 & 0 & p_{44} & p_{41} \\ 0 & 0 & 0 & 0 & p_{14} & \frac{1}{2}(p_{11} - p_{12}) \end{pmatrix} \begin{pmatrix} S_1 \\ S_2 \\ S_3 \\ S_4 \\ S_5 \\ S_6 \end{pmatrix} \tag{66}$$

where the strain-optic (photoelastic) tensor was explicitly shown [11].

If an impermeability change $\Delta\eta_5$ is desired, then either S_5 or S_6 or both is needed. Assuming a strain component S_6 exists, according to equations (66), the impermeability change will be

$$\Delta\eta_5 = p_{41} S_6 \,. \tag{67}$$

A change in this is the impermeability component will promote a rotation of index ellipsoid abount the y axis (in the $x-z$ plane), which in the end will promote coupling between TE and TM modes.

The index change associated with that is

$$\Delta n_5 = -\frac{1}{2}\bar{n}^3 p_{41} S_6 \tag{68}$$

where $\bar{n} = \sqrt{n_o n_e}$.

E. Coupled Mode Theory and TE-TM Converters

Coupled Mode Theory relates charge density distribution perturbations in the region a waveguide is immersed to the perturbations experienced in the waveguide parameters (propagation constants and field distributions) in terms of these parameters in the unperturbed waveguide.

For this analysis, it will be assumed a structure and a coordinate system orientation like the one depicted in figure 6. It will also be assumed a uniaxial substrate.

It is known that the mode field distributions must satisfy the time domain wave equation expressed in equation (37). Rewritten here for convenience

$$\nabla^2 \mathbf{E} - \mu_0 \varepsilon \frac{\partial^2 \mathbf{E}}{\partial t^2} = 0 \ . \tag{69}$$

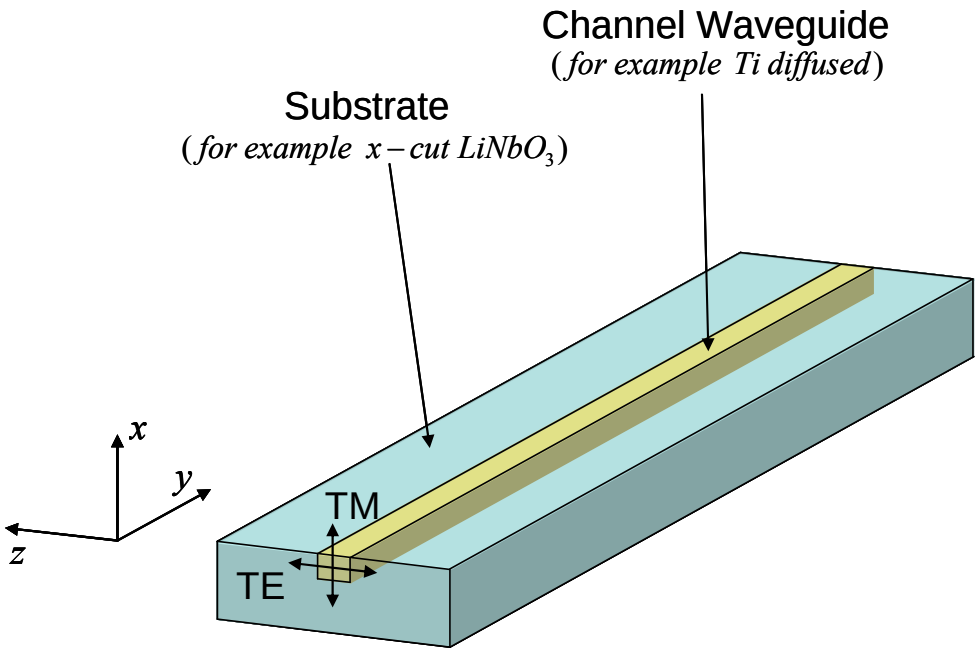

Fig. 6. Schematic diagram of a channel waveguide and coordinate system orientation used.

Recall that the electric displacement (or electric flux density) vector **D** accounts for charge displacements and changes through the polarization density **P** vector and that they are related through the constitutive relation expressed in equation (7), repeated below for convenience

$$\mathbf{D} = \varepsilon_0 \mathbf{E} + \mathbf{P} = \varepsilon_0 (\mathbf{I} + \tilde{\chi}_e) \mathbf{E} \tag{70}$$

A perturbation in the charge density can then be added to equation (70), resulting in a new electric displacement vector such that

$$\mathbf{D}' = \mathbf{D} + \mathbf{P}_{pert} \tag{71}$$

where $\mathbf{D}'$ is the perturbed electric displacement vector that results as an effect of the perturbation in the polarization density vector, expressed by $\mathbf{P}_{pert}$.

Substituting equation (71) into equation (69), yields

$$\nabla^2 \mathbf{E} - \mu_0 \varepsilon_0 \tilde{\varepsilon} \frac{\partial^2 \mathbf{E}}{\partial t^2} = \mu_0 \frac{\partial^2 \mathbf{P}_{pert}}{\partial t^2} \quad . \tag{72}$$

For the unperturbed waveguide ($\mathbf{P}_{pert} = 0$), equation (72) is reduced to equation (69) and the solution for a y-propagating TE mode is in the format

$$\mathbf{E}^m(x,y,z) = \tfrac{1}{2}(C_m E_z^m(x,z) e^{j(\omega t - \beta_m y)} + \underbrace{C_m^* E_z^{m^*}(x,z) e^{-j(\omega t - \beta_m y)}}_{c.c.}) \hat{z} \tag{73}$$

where the asterisk ($*$) stands for complex conjugation and β_m is the propagation constant of the m-th TE mode.

The second element on the right-hand side of equation (73) is the complex conjugate of the first term, denoted by "*c.c.*" from this point on.

The solutions of the unperturbed waveguide form a complete orthogonal set,

therefore, under the assumption of small perturbation, the electric field distribution of the perturbed waveguide may be written as

$$E'(x,y,z) = \frac{1}{2}\sum_{all\ m}(A_m(y)E_T^m(x,z)e^{j(\omega t-\beta_m y)} + c.c.) \tag{74}$$

where $A_m(y)$ is the amplitude of the m-th mode in the composition of the perturbed waveguide electric field distribution, assumed to be a function of y.

Substituting (74) into (72) after some mathematical manipulations and under the assumption of slow-varying amplitude $\left(\left|\partial^2 A_m(y)/\partial y^2\right| << \left|\beta_m\, \partial A_m(y)/\partial y\right|\right)$, it is obtained

$$\sum_{all\ m}\left[-j\beta_m \frac{dA_m}{dy}\mathbf{E}_T^m(x,z)e^{j(\omega t-\beta_m y)} + c.c.\right] = \mu_0 \frac{\partial^2}{\partial t^2}\mathbf{P}_{pert}(\mathbf{r},t) \tag{75}$$

where $\mathbf{E}_T^m(x,z)$ is the transversal component of the m-th unperturbed waveguide mode and the y dependence of A_m is implicitly assumed.

Equation (75) is known as Coupled Mode Equation and for each coupling case to be analyzed, the parameters for the modes that are involved should be conveniently plugged in to obtain the specific equations describing the coupling between the chosen modes.

Considering the co-directional coupling between TE and TM modes of a channel waveguide, assuming the spatially varying amplitude of the TE mode $A_{TE} = A$ and the one associated with TM mode $A_{TM} = B$ to avoid dubious notation, equation (74) can be rewritten

$$\mathbf{E}'(x,y,z) = \frac{1}{2}(A\,E_z^{TE}(x,z)e^{j(\omega t-\beta_{TE}y)}\hat{z} + B\,E_x^{TM}(x,z)e^{j(\omega t-\beta_{TM}y)}\hat{x} + c.c.) \tag{76}$$

and equation (75) may be rewritten as

$$-je^{j\omega t}\left[\beta_{TE}\frac{dA}{dy}\mathbf{E}_{TE}(x,z)e^{-j(\beta_{TE}y)}+\beta_{TM}\frac{dB}{dy}\mathbf{E}_{TM}(x,z)e^{-j(\beta_{TM}y)}+c.c.\right]=\mu_0\frac{\partial^2}{\partial t^2}\mathbf{P}_{pert}(\mathbf{r},t)\,. \quad (77)$$

For the perturbed polarization density vector $\mathbf{P}_{pert}$ it can be written

$$\mathbf{P}_{pert}=\varepsilon_0\left(\Delta\widetilde{\varepsilon}_r\right)\mathbf{E}' \quad (78)$$

where $\Delta\widetilde{\varepsilon}_r$ is the variation in the dielectric permittivity tensor due to the perturbation in the charge density.

Substituting (78) into (77), taking (76) into account, yields

$$\begin{aligned}&-j\left[\beta_{TE}\frac{dA}{dy}\mathbf{E}_{TE}(x,z)e^{-j(\beta_{TE}y)}+\beta_{TM}\frac{dB}{dy}\mathbf{E}_{TM}(x,z)e^{-j(\beta_{TM}y)}+c.c.\right]\\&=\\&\frac{1}{2}\mu_0\frac{\partial^2}{\partial t^2}\left[\left(A\,\Delta\widetilde{\varepsilon}_r\mathbf{E}_{TE}(x,z)e^{-j(\beta_{TE}y)}+B\,\Delta\widetilde{\varepsilon}_r\mathbf{E}_{TM}(x,z)e^{-j(\beta_{TM}y)}+c.c.\right)\right]\,.\end{aligned} \quad (79)$$

Calculating the dot product of equation (79) by $\mathbf{E}^*_{TE}(x,z)$, integrating from $-\infty$ to ∞ in the transverse plane

$$\begin{aligned}&-j\left[\beta_{TE}e^{-j(\beta_{TE}y)}\frac{dA}{dy}\int_{-\infty}^{\infty}\mathbf{E}^*_{TE}(x,z)\mathbf{E}_{TE}(x,z)\,dxdz+\beta_{TM}e^{-j(\beta_{TM}y)}\frac{dB}{dy}\int_{-\infty}^{\infty}\mathbf{E}^*_{TE}(x,z)\mathbf{E}_{TM}(x,z)\,dxdz\right]\\&=\\&-\frac{\omega^2\mu_0\varepsilon_0}{2}\int_{-\infty}^{\infty}\left[\left(A\,\mathbf{E}^*_{TE}(x,z)\Delta\widetilde{\varepsilon}_r\mathbf{E}_{TE}(x,z)e^{-j(\beta_{TE}y)}+B\,\mathbf{E}^*_{TE}(x,z)\Delta\widetilde{\varepsilon}_r\mathbf{E}_{TM}(x,z)e^{-j(\beta_{TM}y)}\right]dxdz\,.\end{aligned} \quad (80)$$

Mode orthonormality condition states that [11]

$$\int_{-\infty}^{\infty} \mathbf{E}_m^*(x,z)\,\mathbf{E}_s(x,z)dxdz = \frac{2\omega\mu}{\beta_m}\delta_{ms} \tag{81}$$

where δ_{ms} is the Kroenecker delta, defined as unity only for $m = s$ and zero for all other values of m and s.

Applying equation (81) to equation (80), yields

$$\frac{dA}{dy} = -jB\frac{\omega\varepsilon_0}{4}\int_{-\infty}^{\infty} \mathbf{E}_{TE}^*(x,z)\Delta\tilde{\varepsilon}_r\mathbf{E}_{TM}(x,z)e^{j(\beta_{TE}-\beta_{TM})y}dxdz \quad . \tag{82}$$

In a similar way it is obtained

$$\frac{dB}{dy} = -jA\frac{\omega\varepsilon_0}{4}\int_{-\infty}^{\infty} \mathbf{E}_{TM}^*(x,z)\Delta\tilde{\varepsilon}_r\mathbf{E}_{TE}(x,z)e^{-j(\beta_{TE}-\beta_{TM})y}dxdz \quad . \tag{83}$$

Defining the quantities

$$\begin{aligned} \kappa_{TE-TM} &= \frac{\omega\varepsilon_0}{4}\int_{-\infty}^{\infty} \mathbf{E}_{TE}^*(x,z)\Delta\tilde{\varepsilon}_r\mathbf{E}_{TM}(x,z)dxdz \\ \kappa_{TM-TE} &= \frac{\omega\varepsilon_0}{4}\int_{-\infty}^{\infty} \mathbf{E}_{TM}^*(x,z)\Delta\tilde{\varepsilon}_r\mathbf{E}_{TE}(x,z)dxdz \quad . \end{aligned} \tag{84}$$

Since the fields are all real

$$\kappa_{TE-TM} = \kappa_{TM-TE} = \kappa \tag{85}$$

This result allows to write equations (82) and (83) as simultaneous set of differential equations

$$\begin{aligned} \frac{dA}{dy} &= -j\,\kappa\,B\,e^{j(\beta_{TE}-\beta_{TM})y} \\ \frac{dB}{dy} &= -j\,\kappa\,A\,e^{-j(\beta_{TE}-\beta_{TM})y} \quad . \end{aligned} \tag{86}$$

It can be noticed in equation (86), known as co-propagating Coupled Mode Equations, that there is a phase factor in each of the two equations. These factors are called phase mismatch and they arise from propagation constant difference between the two modes. As a result, after some propagation distance, one of the modes will start lagging behind the other and the conversion between polarizations will be disrupted.

This fact can be qualitatively explained stating that once a perturbation is present, there will be mode coupling in a region over which a waveguide traverses. After having propagated for some length, light will have transferred energy to the other polarization mode and since both modes travel at different speeds, they start accumulating phase differences between them. As the phase departs from a null, destructive interference between light converted at different positions will start happening, lowering the efficiency in the conversion.

In order to circumvent the phase mismatch problem, a periodic variation along the propagation direction is introduced in the perturbation that couples both modes. This variation will be assumed to have a spatial period Λ , allowing to expand the term $\Delta\varepsilon_r$ in a Fourier series such that

$$\Delta\varepsilon_r = \sum_{m\neq 0} \varepsilon_m(x,z) e^{-jm\frac{2\pi}{\Lambda}y} \tag{87}$$

where ε_m is the amplitude of the permittivity modulation m -th harmonic.

Introducing this change in equations (84) and (86), under the assumption that only the first harmonic of the perturbation will efficiently promote coupling between the modes, being the other harmonic amplitudes small enough to be neglected, equation (86)

is now rewritten

$$\frac{dA}{dy} = -j\,\kappa\,B\,e^{j\Delta y}$$
$$\frac{dB}{dy} = -j\,\kappa\,A\,e^{-j\Delta y} \tag{88}$$

where $\Delta = \beta_{TE} - \beta_{TM} \pm \frac{2\pi}{\Lambda}$ and is called the phase mismatch factor.

Assuming that prior to entering in the coupling region all light is in one state of polarization, we may write:

$$A(0) = 1 \quad \text{and} \quad B(0) = 0 \quad . \tag{89}$$

For this initial condition, the solutions to equations (88) are

$$A(y) = e^{-j\Delta y/2}\left[\cos\delta y + j\frac{\Delta}{2\delta}\sin\delta y\right]$$
$$\text{and} \tag{90}$$
$$B(y) = j\frac{\kappa}{\delta}e^{j\Delta y/2}\sin\delta y$$

where $\delta = \sqrt{\left(\Delta/2\right)^2 + \kappa^2}$.

Assuming a reversed initial condition for the input amplitudes, say

$$A(0) = 0 \quad \text{and} \quad B(0) = 1 \quad . \tag{91}$$

Solutions to equations (88) will be

$$A(y) = j\frac{\kappa}{\delta}e^{j\Delta y/2}\sin\delta y$$
$$\text{and} \tag{92}$$
$$B(y) = e^{j\Delta y/2}\left[\cos\delta y - j\frac{\Delta}{2\delta}\sin\delta y\right] \quad .$$

Any state of polarization arriving at the coupling region may be decomposed in

the two orthogonal polarization modes. After having propagated through the coupling region the amplitudes in each polarization are then added together (considering phases) to result the new amplitude in that polarization. This may be summarized using a matrix form to describe the amplitudes in each polarization after the coupling region:

$$\begin{pmatrix} A(y) \\ B(y) \end{pmatrix} = \begin{pmatrix} e^{-j\Delta y/2}\left[\cos\delta y + j\frac{\Delta}{2\delta}\sin\delta y\right] & je^{-j\Delta y/2}\frac{\kappa}{\delta}\sin\delta y \\ je^{j\Delta y/2}\frac{\kappa}{\delta}\sin\delta y & e^{j\Delta y/2}\left[\cos\delta y - j\frac{\Delta}{2\delta}\sin\delta y\right] \end{pmatrix} \begin{pmatrix} A(0) \\ B(0) \end{pmatrix} \quad . \quad (93)$$

The phase mismatch Δ can be expressed in terms of the optical signal frequency by

$$\Delta = \frac{2\pi\nu}{c}\left(n_{TE} - n_{TM}\right) \pm \frac{2\pi}{\Lambda} \quad (94)$$

where ν is the optical frequency, c is the vacuum speed of light, n_{TE} and n_{TM} are the effective refractive indices for each mode (TE and TM, respectively) and Λ is the spatial period of perturbation.

For a specific optical frequency ν_o at which phase-matched condition ($\Delta = 0$) is achieved:

$$\Lambda = \frac{c}{\nu_o(n_{TE} - n_{TM})} = \frac{\lambda_o}{\left|n_{TE} - n_{TM}\right|} \quad (95)$$

where λ_o is the wavelength associated with frequency ν_o. The absolute value was used to avoid results with no physical meaning.

It can be noticed from equation (95) that the distance over which both polarizations accumulate a phase difference of 2π between them should be equal to the

perturbation spatial period. Now light with a specific wavelength which had its polarization converted in the preceding perturbation period will "interfere constructively" with light that will have its polarization converted in the next perturbation period. Since the phase difference is a function of the wavelength, this may be attained perfectly only for a single wavelength, leaving other wavelengths with imperfect match or phase-mismatched.

Coupling structures built with this goal are often defined by a photolithographic process with some phase matched wavelength in mind. Once the perturbation spatial period is defined in the photolithography, the device can be wavelength tuned only by changing the term $(n_{TE} - n_{TM})$ in equation (95). This may be accomplished through the temperature dependence of the crystal birefringence or through eletrooptical birefringence tuning.

Aiming at evaluating the spectral behavior of the amplitudes for a phase mismatched condition, one should expand the expression for the phase mismatch factor (Δ) around the phase-matched frequency (ν_o):

$$\Delta = \frac{d\Delta}{d\nu}(\nu - \nu_o) = \frac{2\pi}{c}\left[(n_{TE} - n_{TM}) + \nu\frac{d(n_{TE} - n_{TM})}{d\nu}\right](\nu - \nu_o) \quad . \tag{96}$$

Expanding and regrouping terms in (96)

$$\Delta = \frac{2\pi}{c}\left[\underbrace{n_{TE} + \nu\frac{dn_{TE}}{d\nu}}_{n_{gTE}} - \underbrace{\left(n_{TM} + \nu\frac{dn_{TM}}{d\nu}\right)}_{n_{gTM}}\right](\nu - \nu_o) \quad . \tag{97}$$

Finally resulting in

$$\Delta = \frac{2\pi}{c}(n_{gTE} - n_{gTM})(\nu - \nu_o) \tag{98}$$

where n_{gTE} and n_{gTM} are the group refractive indices of the TE and TM modes, respectively and the term $(\nu - \nu_o)$ expresses the frequency difference from phase matched frequency and is usually called frequency detuning.

Assuming that the substrate is a *x-cut* $LiNbO_3$ sample, that the modes are well confined and recalling the schematic diagram in figure 6, the TM mode will propagate with an effective refractive index very close in value to the substrate ordinary refractive index n_o, whereas the TE mode effective refractive index will be close in value to the substrate extraordinary index n_e.

F. Z-Transform and Optical Filters

The Z-transform is a tool used in analyzing discrete signals. One of the most common ways of obtaining a discrete signal is by sampling a time continuous signal at a regular sampling interval T. The obtained signal is then represented by discrete sequence.

Similar to the analysis done on a continuous time signal by a Fourier transform, the discrete signal can be analyzed by a version of the Fourier transform tailored to time discrete signals, called discrete-time Fourier transform (DTFT). Summarizing the facts, the sequence that describes a discrete signal in the time domain is transformed by the DTFT in another sequence which expresses the frequency content of the time domain version of the signal. Since the time version was sampled at regular intervals, it is also

expected that the frequency spectrum will show a periodic behavior, that will depend on the bandwidth of the signal being analyzed as well as on the sampling interval T.

The expression for a DTFT of a sequence $x(n)$ is given by

$$X(\nu) = \sum_{n=-\infty}^{\infty} x(n) e^{-j2\pi\nu n} \tag{99}$$

where ν is a normalized frequency defined as $\nu \equiv fT = f/FSR$, f is the absolute (unscaled) frequency, T is the sampling interval and FSR is the free-spectral range, i.e. the frequency interval after which the frequency response starts repeating itself (frequency spectrum period) [18].

Another format commonly used is obtained by using the normalized angular frequency given by $\omega = 2\pi\nu$.

For discrete signals, the Z-transform is to the DTFT in much the same way the Laplace transform is to the Fourier transform for continuous signals. As the Laplace transform is a very powerful tool to describe analog filters, so is the Z-transform in describing digital filters. It is obtained by substituting z for $e^{j\omega}$ in equation (99), resulting [18]

$$H(z) = \sum_{n=-\infty}^{\infty} h(n) z^{-n} \tag{100}$$

where $h(n)$ is the impulse response of a filter.

The inverse transform is defined by applying complex-plane integration theorem (Cauchy integral theorem) as

$$h(n) = \frac{-j}{2\pi} \oint H(z) z^{n-1} dz \quad . \tag{101}$$

The Z-transform may also be seen as a mapping operation on the complex s-plane (from Laplace Transform). The mapping is done through the relationship $z = e^{sT}$. This way, the imaginary (frequency) axis is mapped on the unit circle in the z-plane; the stability region on the s-plane (left-hand semi-plane) is mapped inside the unit circle in the z-plane. The unstable region on the s-plane (right-hand semi-plane) is mapped outside the unit circle. The frequency response of a filter is calculated by evaluating $H(z)$ over the unit circle ($z = e^{j\omega}$). Figure 7 illustrates this mapping operation.

In a digital filter, the input and the output are related by a sum that involves inputs and previous outputs

$$y(n) = b_0 x(n) + b_1 x(n-1) + \cdots + b_M x(n-M) - a_1 y(n-1) - \cdots - a_N y(n-N) \tag{102}$$

where the coefficients a_n and b_m are the weights for each component on the filter output.

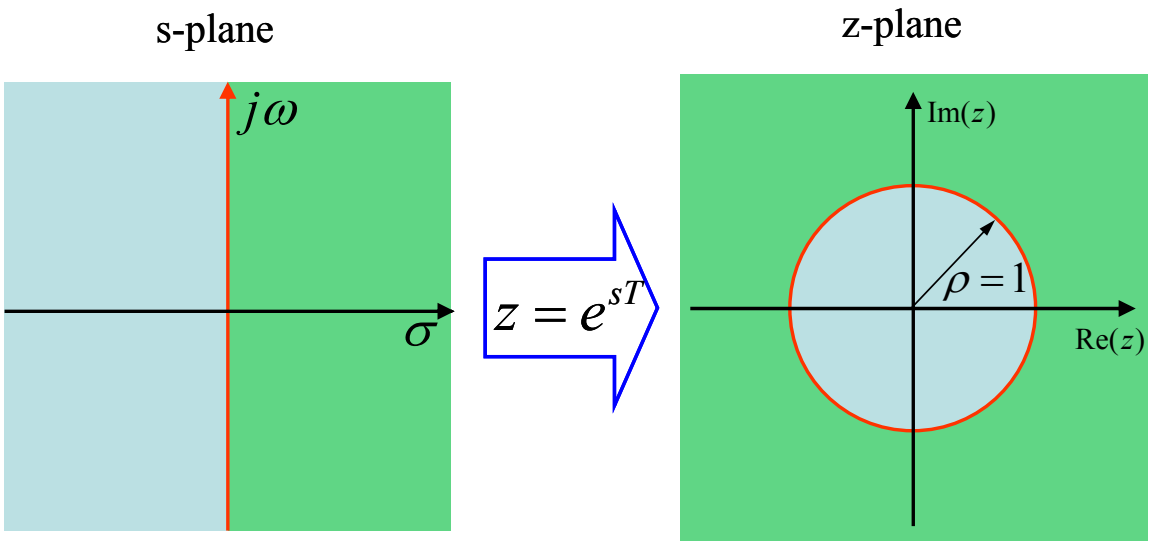

Fig. 7. Mapping of s-plane into z-plane.

The Z-transform description of the sequence in equation (102) is expressed as

$$H(z) = \frac{B(z)}{A(z)} = \frac{\sum_{m=0}^{M} b_m z^{-m}}{1 + \sum_{n=1}^{N} a_n z^{-n}} = \frac{\Gamma\, z^{N-M} \prod_{m=1}^{M} (z - z_m)}{\prod_{n=1}^{N} (z - p_n)} \tag{103}$$

where Γ is a gain factor, z_m are called the zeroes and p_n are called the poles of the filter response.

There are two basic configurations of digital filters distinguished by the type of polynomials that appear in their Z-transform description.

A filter having only zeroes (no poles) is called a Finite Impulse Response (FIR) filter, its description would be limited to the numerator of equation (103) and it would present only feedforward paths. The schematic diagram of a single stage FIR filter is presented in figure 8 (a).

On the other hand, a filter having only poles is called a Infinite Impulse Response (IIR) filter and its description would be limited to the $\Gamma / A(z)$ term of equation (103), presenting only feedback paths. The schematic diagram of a single stage IIR filter is presented in figure 8 (b).

All other possible configurations of a digital filter can be expressed as a combination of these two basic building blocks.

Much like the same way a desired filtering function in the analog domain is synthesized by conveniently locating poles and zeroes of the transfer function on the s-plane, digital filters are synthesized by applying this procedure on the z-plane.

In order to trace the relationship between digital and optical filters, assume an optical wave entering a section of a waveguide. After having propagated a certain distance L along the waveguide, the electric field intensity of the wave may then be described in terms of the input electric field intensity as

$$E(L) = E_{in} e^{-jn\frac{\omega}{c}L} \tag{104}$$

where n is the group refractive index of the mode at which the optical wave propagates along the waveguide.

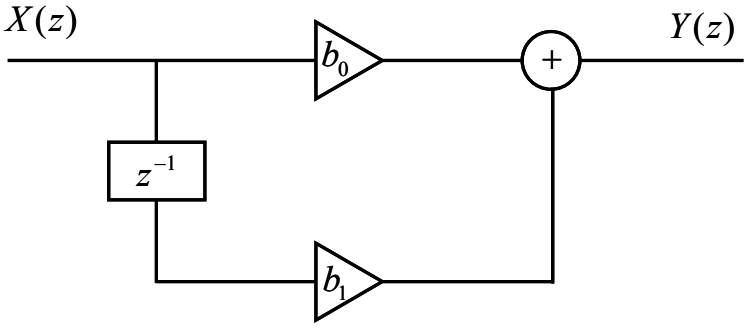

(a)

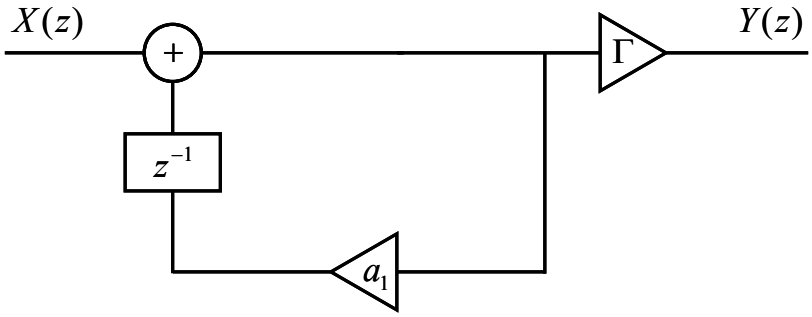

(b)

Fig. 8. Schematic diagram of single-stage filters: (a) FIR filter; (b) IIR filter.

If equation (104) is further simplified by including the propagation delay between the two positions, given by $T = nL/c$, it is reduced to

$$E(L) = E_{in} e^{-j\omega T} \quad . \tag{105}$$

If now the term $e^{-j\omega T}$ is substituted for a new variable z^{-1} ; the analogy between sampling a signal at a regular time interval, in digital filter theory, and observing an optical signal at regular positions apart a propagation length L (or a delay T), as it propagates down a waveguide, is made clear.

With this tool at hand, transfer functions in the optical domain can now be synthesized by using it, at least in theory. It is only left to the realizability of the building blocks in the optical domain.

For example a single-stage FIR filter in the optical domain may be synthesized by use of a Mach-Zenhder interferometer with asymmetric arms [18] by assuming that the unit delay T is related to the path difference between both arms. The analogy can be seen by comparing figure 9(a) with figure 8(a).

The same way a single-stage IIR filter in the optical domain may be synthesized by use of a ring resonator, a Fabry-Perot interferometer or a Gires-Tournois interferometer. The dependence of the output on previous history of inputs and/or outputs can be seen by comparing figure 9(b) with figure 8(b).

Very important parameters in analyzing the filter response are the magnitude response, group delay and dispersion.

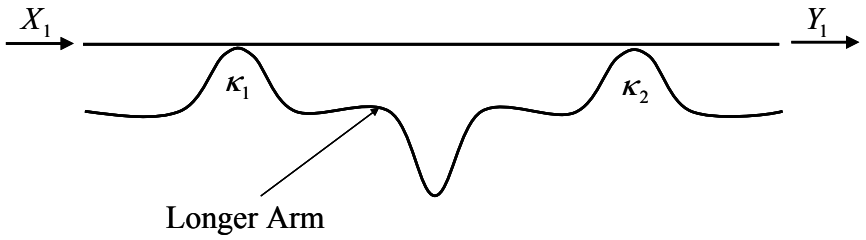

(a)

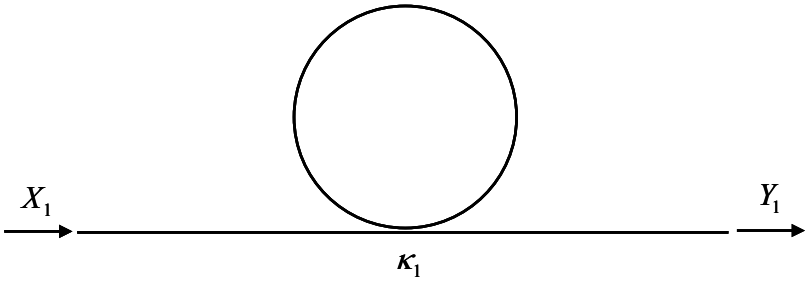

(b)

Fig. 9. Examples of single-stage optical filter realizations: (a) FIR filter by use of a Mach-Zehnder Interferometer; (b) IIR filter by use of a Ring Resonator.

A filter magnitude response is defined as the modulus of the transfer function evaluated on the unit circle ($z = e^{j\omega}$), i.e. [18]

$$\left|\left[H(z)\right]_{z=e^{j\omega}}\right| = \left|H(\omega)\right| \ . \tag{106}$$

In optical systems, the physical quantity more easily measured is power, not field intensity; therefore, it makes more sense to calculate the square magnitude when analyzing filters in the optical domain.

The filter group delay is defined as the negative derivative of the transfer function phase, also evaluated on the unit circle, i.e. [18]

$$\tau_n = -\frac{d}{d\omega}\tan^{-1}\left[\frac{\mathrm{Im}\{H(z)\}}{\mathrm{Re}\{H(z)\}}\right]_{z=e^{j\omega}} \tag{107}$$

where τ_n is the group delay normalized with respect to the unit delay T, therefore the absolute group delay is given by $\tau_g = \tau_n T$.

The dispersion is defined as the derivative of the group delay with respect to the frequency, i.e. [18]

$$D_n = \frac{d\tau_n}{d\nu} = 2\pi\frac{d\tau_n}{d\omega} \tag{108}$$

where D_n is the dispersion in filter normalized parameters.

In optical systems, the absolute dispersion is usually defined by the derivative of the absolute group delay with respect to the wavelength, therefore the scaling between the absolute and normalized dispersions is

$$D = -c\left(\frac{T}{\lambda}\right)^2 D_n \quad . \tag{109}$$

CHAPTER III

DEVICE STRUCTURE AND ANALYSIS

In this chapter the proposed structure for a sparse grating filter is presented and analyzed. The starting point for the comprehension of the operation is the continuous-grating TE-TM polarization converter. Once the principle of operation is understood, the concept, analysis and design of a sparse grating filter are presented. Tuning processes for the center wavelength are then presented. Last on the chapter, as an extension of the concept, a polarization independent filter based on TE-TM polarization converting sparse gratings is proposed and explained.

A. Continuous-Grating TE-TM Polarization Converter

The first building block in constructing the sparse grating filter is the grating itself. Understanding the way a continuous grating works will also help understand the TE-TM polarization conversion in a sparse grating structure.

The TE-TM modes of an unperturbed channel waveguide propagate without power exchange between each other because of the mode orthogonality property. In order to achieve the mode conversion, under the light of the Coupled Mode Theory presented in the previous chapter, some sort of periodic perturbation along the propagation direction should be introduced in the waveguide.

Among the ways of building this periodic perturbation, often called grating, is by way of the static strain-optic effect. This is the way used throughout this work.

The strain-inducing grating is accomplished by growing a strain-inducing SiO_2 film and defining an overlay periodic structure on the $LiNbO_3$ substrate.

The induced strain arises from the fact that the SiO_2 film is deposited on a $LiNbO_3$ substrate, previously heated and kept at an elevated constant temperature during deposition. As the sample is cooled down and brought to room temperature, due to the fact that lithium niobate has a much higher thermal expansion coefficient than the silicon dioxide film ($\alpha_{LiNbO_3} = 1.54 \times 10^{-5}\ ^{o}C^{-1}$ [19] and $\alpha_{SiO_2} = 5.5 \times 10^{-7}\ ^{o}C^{-1}$ [20]), it will tend to contract much more than SiO_2. But now adhering to each other an equilibrium position will be found at which $LiNbO_3$ will not contract as much as it would alone and SiO_2 will contract a little more than it would alone. As a result some of the energy used in the $LiNbO_3$ expansion and the energy used to contract SiO_2 will be stored in a strain field. Summarizing, the expansion coefficient mismatch between the two materials builds up strain at their interface.

That strain propagates into the substrate and waveguide; via the strain-optic effect produces a change in one of the components of the dielectric permittivity tensor that will enable coupling between the two modes with orthogonal polarizations.

After cooling down, the silicon dioxide film is patterned by a photolithographic process and then etched at room temperature to define the overlaid structure with spatial period Λ on the waveguide. This results in the periodic variation on the appropriate shear strain, therefore on the appropriate impermeability tensor component needed to phase-match the two modes.

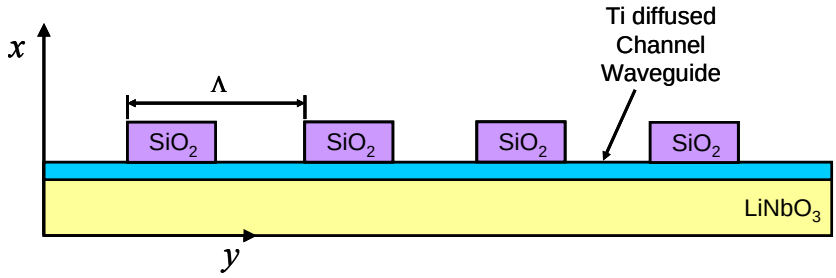

(a)

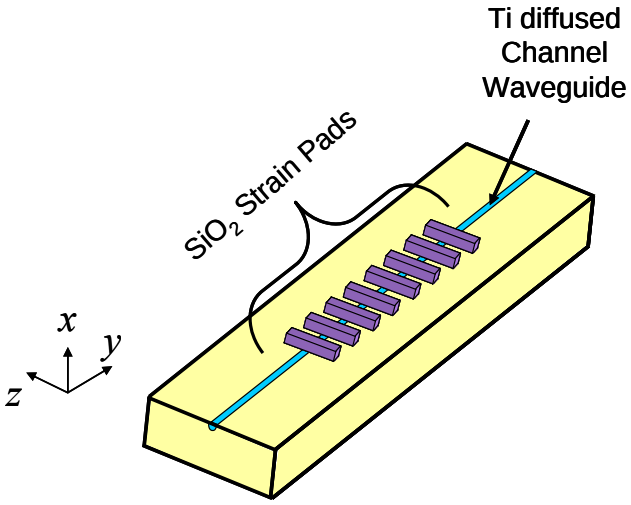

(b)

Fig. 10. Schematic diagram of a TE-TM polarization converter using a continuous SiO_2 strain-inducing grating on a x-cut, y-propagating Ti-diffused $LiNbO_3$ waveguide: (a) Sideview; (b) Perspective.

The channel waveguides used in this work are fabricated by diffusing Ti strips into an x-cut $LiNbO_3$ substrate, light propagation is in the y-axis direction. A schematic diagram of the final structure is shown in figure 10.

Previous results in our group [20] and published in the literature [21] show the periodic behavior of the shear strain component S_6 needed.

According to equation (95), there will be a wavelength, called phase-matched wavelength, which will have no phase mismatch ($\Delta = 0$). Assume an optical wave with the phase-matched wavelength have propagated a length L in the polarization conversion region, from equation (93), the field relations after this length may be written as

$$\begin{pmatrix} A(L) \\ B(L) \end{pmatrix} = \begin{pmatrix} \cos\kappa L & j\sin\kappa L \\ j\sin\kappa L & \cos\kappa L \end{pmatrix} \begin{pmatrix} A(0) \\ B(0) \end{pmatrix} \tag{110}$$

where A is the electric field amplitude of one of the modes (TE mode for example) and B is the amplitude of the mode orthogonal to the first (TM mode).

One parameter used to evaluate the performance of polarization converters of this type is the polarization conversion efficiency, defined as the ratio, at the output of the coupling region, between power in the converted polarization and the sum of powers in both polarizations, when only one polarization is input.

Assuming an optical wave with TE polarization only is coupled to the waveguide with normalized amplitude ($A = 1,\ B = 0$), the polarization conversion efficiency at the phase-matched wavelength is expressed according to equation (110) as

$$PCE = \frac{|B(L)|^2}{|A(L)|^2 + |B(L)|^2} = \frac{\sin^2\kappa L}{\cos^2\kappa L + \sin^2\kappa L} = \sin^2\kappa L \quad . \tag{111}$$

The power fraction remaining in the unconverted polarization is given by

$$PF_{unconv} = \frac{|A(L)|^2}{|A(L)|^2 + |B(L)|^2} = \frac{\cos^2\kappa L}{\cos^2\kappa L + \sin^2\kappa L} = \cos^2\kappa L \quad . \tag{112}$$

This procedure can be repeated for every wavelength in the bandwidth of interest, except that now, the frequency detuning from the phase-matched condition should be taken into account. the associated "transmission matrices" for the coupling regions (equation (93)) will not be simple trigonometric functions of κL, they will show complex exponentials multiplied by trigonometric functions that are both functions of the frequency detuning. Figure 11 shows the power fraction in each of the two polarizations for the two situations described above. For the phase-mismatched wavelength it was assumed a frequency detuning such that $\delta = 2\kappa$.

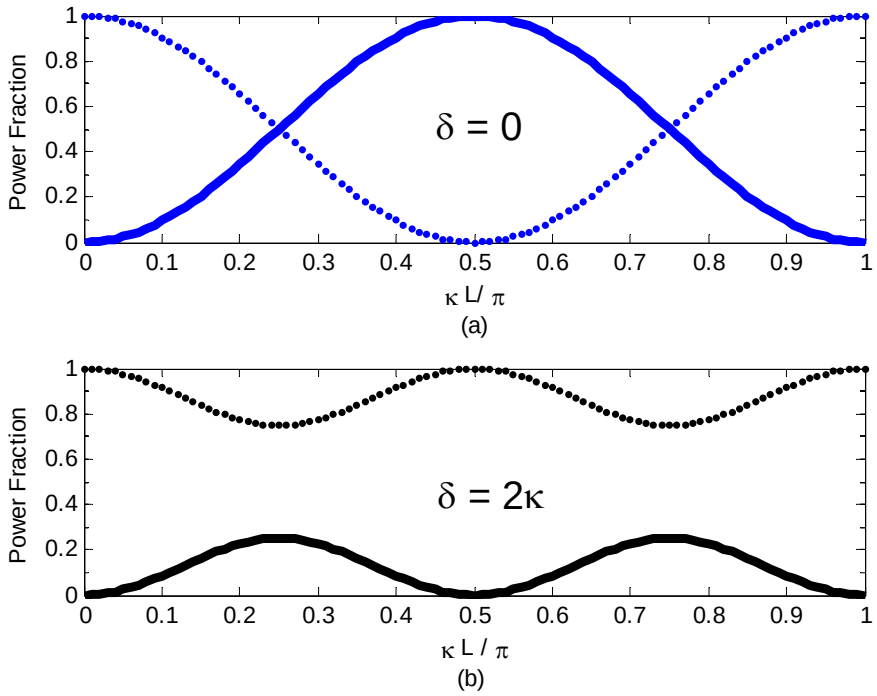

Fig. 11. Power fraction in each mode as a function of normalized propagation length in conversion region. For both, unconverted power fraction in dotted line: (a) $\delta = 0$; (b) $\delta = 2\kappa$.

From figure 11, it can be concluded that full conversion is achievable only for the phase-matched wavelength ($\delta = 0$) and under the condition $L = (2n+1)\pi/2\kappa$. All other wavelengths will experience different conversion efficiencies over the same propagation length as a consequence of being detuned from the phase-matched wavelength.

Figure 12 shows an example of the polarization conversion efficiency over a broad spectrum of frequencies. It was assumed a phase-matched wavelength of 1545 nm ($\nu_0 = 194.03883\,\text{THz}$). Coupling region length was taken such that $L = \pi/2\kappa$. The modes were assumed well confined, therefore, their effective indices being close to the respective value of the bulk substrate ($n_{TE} \approx n_e$ and $n_{TM} \approx n_o$), at the phase-matched wavelength.

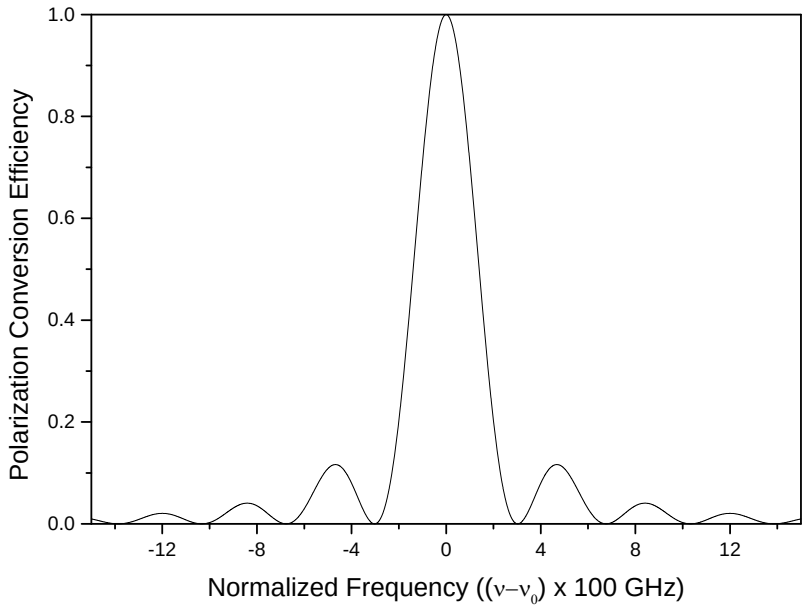

Fig. 12. Polarization conversion efficiency for a countinuous strain-inducing grating $n_{TE} = 2.13828$; $n_{TM} = 2.21150$; $n_{gTE} = 2.18267$; $n_{gTM} = 2.26442$.

Refractive indices were obtained from the literature [22], from which the dispersion curves were also obtained. From the dispersion curves, group refractive indices ($n_{gTE} = 2.18267$ and $n_{gTM} = 2.26442$) could be calculated and substituted into equation (98). After that, equations (111) and (93) were used to plot the well-known polarization conversion efficiency shown.

At the grating output, some of the light will remain on the same polarization as it entered the device (non-phase-matched wavelengths) and some of the light will be converted to the orthogonal polarization state, following the conversion function plotted in figure 12. Therefore it is possible to realize a filtering function with this structure, by means of a polarization filtering, for example, with a polarizer placed after the device.

It is observed in the filtering function (figure 12) that the nulls are not equally spaced in frequency, therefore making it difficult to define channel regions and avoid cross-talk between them upon detecting the optical signal after filtering in this type of device.

For example, assume a “comb” of closely-packed channels, with 100 GHz spacing between their centers and with 100 GHz bandwidth (FWHM), like it is depicted in figure 13 (a). This is a fair representation of a channel assignment for a DWDM communication system.

Now assume the filtering function in figure 13 (b). This is the same filtering function of figure 12, shown only on a narrower bandwidth.

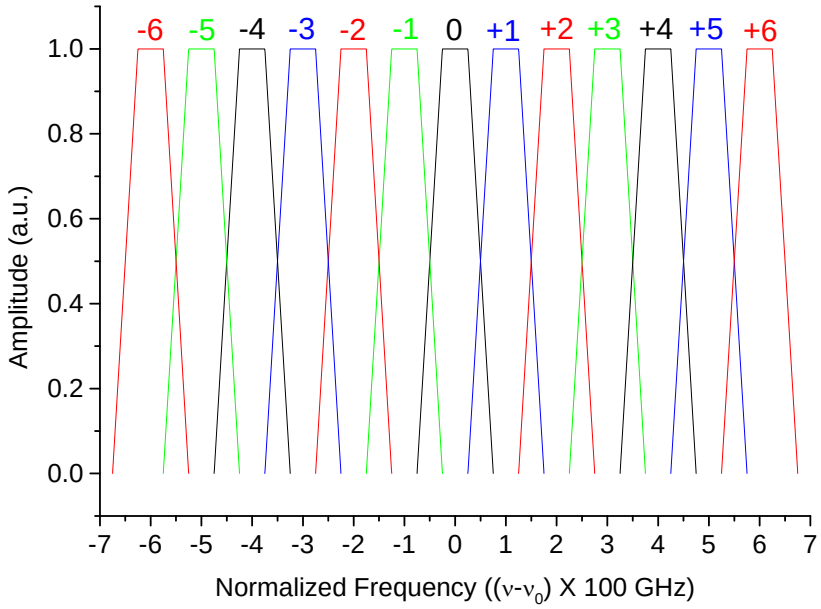

(a)

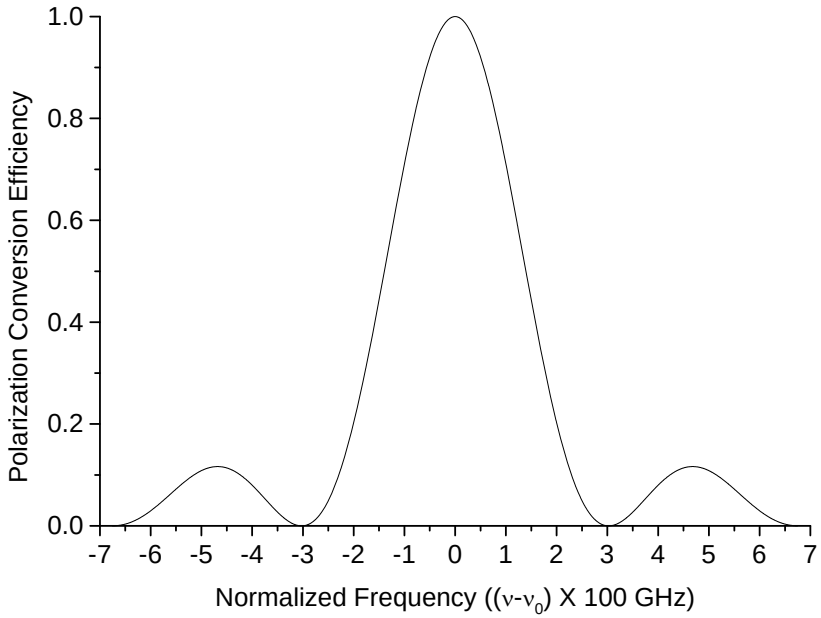

(b)

Fig. 13. Example of filtering performed by a continuous strain-inducing grating: (a) channel “comb”; (b) filtering function; (c) resulting spectrum.

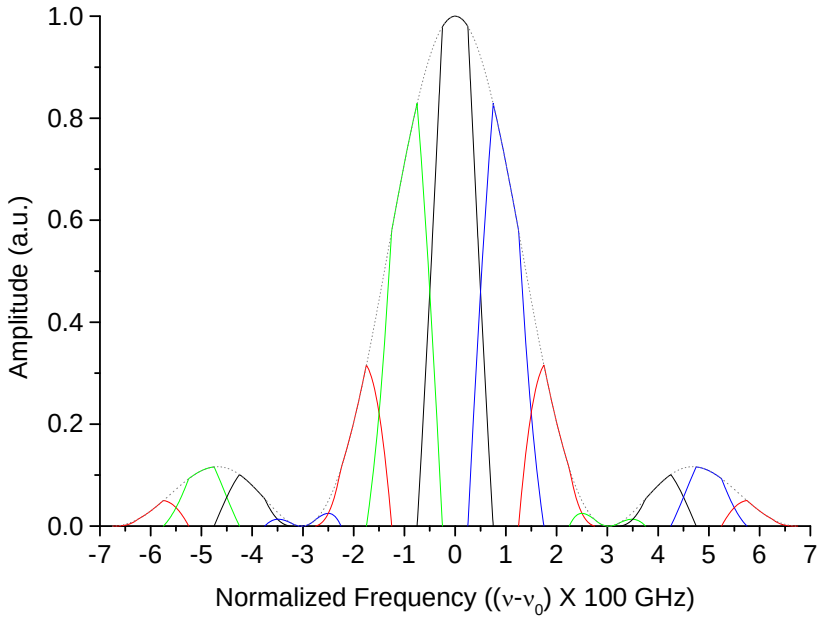

(c)

Fig. 13. Continued

The obtained frequency spectrum after the channel "comb" being filtered by going through the continuous grating is obtained by multiplying the two spectra in figure 13(a) and (b). It is shown in figure 13(c).

Also form figure 13(c), it can be noticed that upon being detected the channels will cross-talk. First because of the low selectivity of the main detection region to operate with the proposed channel spacing: channels -2,-1, 0,1 and 2 show significant power detected within the passband. This can be fixed by using a longer grating (longer L) or by making the strain-optic interaction stronger, resulting in a bigger coupling coefficient (κ), thus making the product κL bigger ($3\pi/2$ or even $5\pi/2$).

Second because even channels located on sidelobes put some power in the detection bandwidth.

In figure 13(c) there are two channels (-3 and +3) that almost have no power in the detected bandwidth. That would be the ideal behavior for every channel in the stopband.

Therefore in an ideal filtering function, the passband should contain only one channel within its limits and channels on the stopband would have to fall on nulls of the filtering function to minimize power on the detected bandwidth.

Controlling the filtering function to place nulls in the center of channels in the stopband is the goal of the sparse-grating TE-TM polarization converter idea.

B. Sparse-Grating TE-TM Polarization Converter

By sparse grating it is meant a structure with smaller sections of polarization conversion separated by clear sections (no grating) along the desired waveguide like it is pictured in figure 14 for a 8-coupling region sparse grating.

The desired periodicity in the rejection band of the filtering function would also require that the overall filtering function be periodic itself, presenting transmission peaks after every certain number of channels. This way, instead of filtering only one wavelength it would slice the communications spectrum.

The determination of the coupling strengths for each region, i.e. what fraction of the incident light power is converted to the orthogonal polarization, and as a consequence their length; their spacing, that will define the repetition period of the filtering function

(Free-spectral range); as well as the number of coupling regions, which dictates the number of nulls in the stop band, will be defined by the requirements of the desired filtering function.

This integrated-optic topology is very similar in functioning to the bulk polarization interference filter, also know as Šolc filter. In that device, rotated birefringent plates control the amount of light coupled to the orthogonal polarization mode and its length controls the phase retardation accumulated between the two modes upon propagating through the plate. Spacing between birefringent plates controls the free spectral range (FSR) of the overall filter response [11].

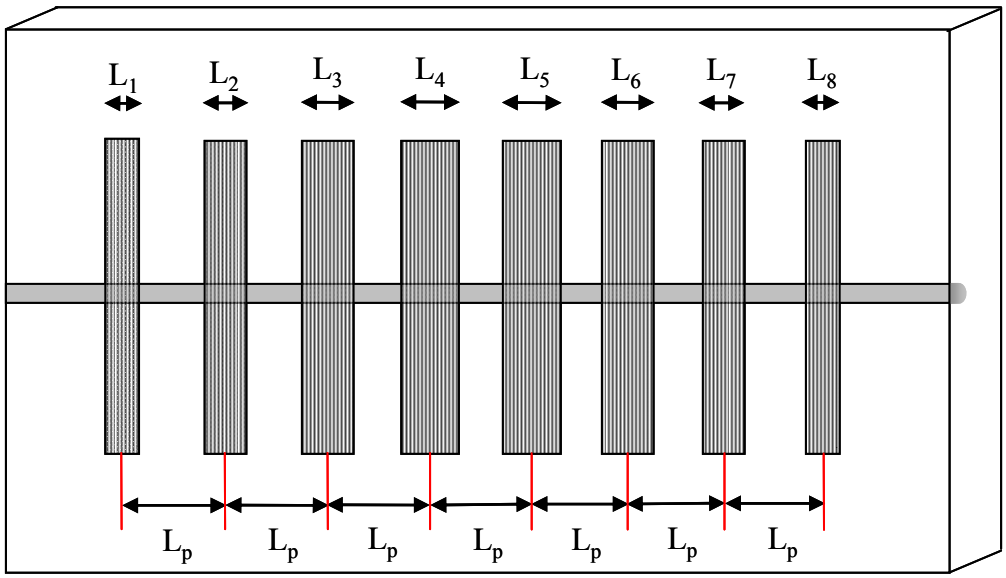

Fig. 14. Schematic diagram of an eight-coupling region sparse-grating TE-TM polarization converter filter.

In order to analyze this type of device a propagation matrix approach will be adopted.

The propagation of light through a polarization coupling region of length L_i, is obtained by direct substitution of the length in equation (93), yelding

$$\begin{pmatrix} E_{TE}(L_i) \\ E_{TM}(L_i) \end{pmatrix} = \overbrace{\begin{pmatrix} e^{-j\Delta L_i/2}\left[\cos\delta L_i + j\frac{\Delta}{2\delta}\sin\delta L_i\right] & je^{-j\Delta L_i/2}\frac{\kappa}{\delta}\sin\delta L_i \\ je^{j\Delta L_i/2}\frac{\kappa}{\delta}\sin\delta L_i & e^{j\Delta L_i/2}\left[\cos\delta L_i - j\frac{\Delta}{2\delta}\sin\delta L_i\right] \end{pmatrix}}^{C_i} \begin{pmatrix} E_{TE}(0) \\ E_{TM}(0) \end{pmatrix} \tag{113}$$

where C_i will be called the coupling matrix for the $i-th$ coupling region, i varies in the range $i = 1, \ldots N$ and N is the number of polarization coupling regions in the whole structure.

Besides the coupling regions, one must consider the differential group delay that arises from the different optical paths for each polarization when propagating from one coupling region to the next. The propagation matrix relation for both polarizations in the clear region is given by

$$\begin{pmatrix} E_{TE}(L_p) \\ E_{TM}(L_p) \end{pmatrix} = \begin{pmatrix} e^{-j\frac{\omega}{c}\left(n_{gTM}-n_{gTE}\right)L_p} & 0 \\ 0 & 1 \end{pmatrix} \begin{pmatrix} E_{TE}(0) \\ E_{TM}(0) \end{pmatrix}. \tag{114}$$

The term $\left(n_{gTM} - n_{gTE}\right)L/c$ in the expression above is the differential time delay experienced between both polarizations when propagating between sections. It represents the unit delay T used in the Z-transform description shown in the previous chapter (see equation (104)). Using the variable *z*, the propagation matrix for the light propagating

between coupling regions (clear region), is obtained by rewriting equation (114), yielding

$$\begin{pmatrix} E_{TM-out} \\ E_{TE-out} \end{pmatrix} = \overbrace{\begin{pmatrix} z^{-1} & 0 \\ 0 & 1 \end{pmatrix}}^{P} \begin{pmatrix} E_{TM-in} \\ E_{TE-in} \end{pmatrix} \quad . \tag{115}$$

Realizing that the output of a coupling region is coincident with the input of the clear region and vice versa, the compound result of propagation through a coupling region followed by a clear waveguide length is obtained by multiplying the coupling matrix C_i in equation (113) and the propagation matrix P in equation (115).

Therefore, the resulting matrix for the whole structure is obtained by cascading the matrices like the sections (coupling or just propagation) appear in the light path. It will present polynomials in z^{-1} as its elements. The off-diagonal elements will be the polarization converted filtering function (amplitude-like).

$$\begin{pmatrix} E_{TM-out} \\ E_{TE-out} \end{pmatrix} = C_n P C_{n-1} P \cdots P C_2 P C_1 \begin{pmatrix} E_{TM-in} \\ E_{TE-in} \end{pmatrix} = \begin{pmatrix} A(z) & jB^R(z) \\ jB(z) & A^R(z) \end{pmatrix} \begin{pmatrix} E_{TM-in} \\ E_{TE-in} \end{pmatrix} \tag{116}$$

where the superscript R denotes the nomenclature “reverse polynomial”.

The reverse polynomial of an order N polynomial, $H_N(z)$, is defined as [18]

$$H_N^R(z) = z^{-N} H_N^*[(z^*)^{-1}] \quad . \tag{117}$$

Equation (117) can be more simply stated in the sentence: The reversed polynomial is obtained by complex conjugating the original polynomial coefficients and reversing their order in the polynomial, explicitly

$$H_N(z) = h_0 + h_1 z^{-1} + \cdots + h_N z^{-N}$$
$$H_N^R(z) = h_N^* + h_{N-1}^* z^{-1} + \cdots + h_o^* z^{-N} \quad . \tag{118}$$

Recalling that the z-transform is a mapping operation on the complex s-plane, and that the imaginary (frequency) axis is mapped on the unit circle in the z-plane, it is possible to conveniently place the desired filtering function zeros on the unit circle, obtain the resulting polynomial and identify term by term with the off-diagonal polynomial obtained by cascading the matrices. This approach will result in *N* equations in *N* unknown coupling strengths.

Figure 15 shows an example of zeroes placement in the z-plane. Aligned with the goal of the present work, it shows five zeroes equally spaced around the circle (equally spaced in frequency and over a free-spectral range).

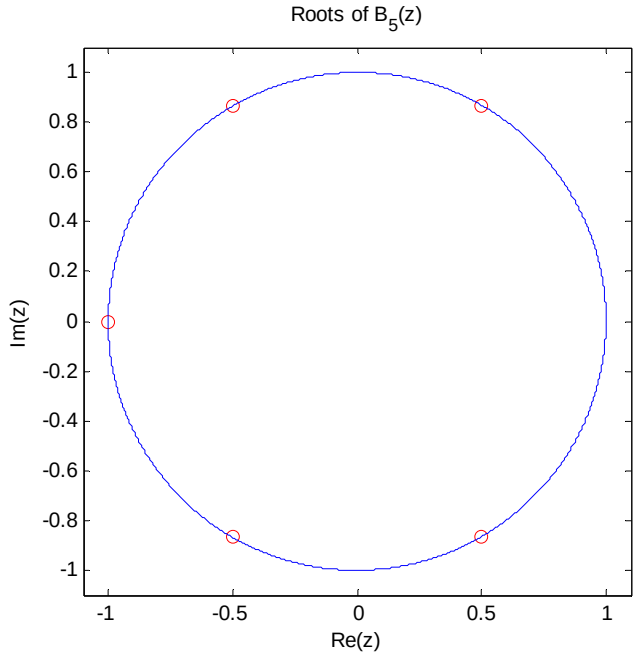

Fig. 15. Five equally spaced zeroes (red circles) placed on the z-plane unit circle.

In order to calculate the coupling strengths, the approximation that the coupling region lengths are much smaller than the separation between them ($L_i / L_p << 1$) was initially made. This simplification will make the transmission matrix elements of the coupling regions to be only trigonometric functions of the coupling strengths $\zeta_i = \kappa L_i$ because

$$e^{\pm j\Delta\frac{L_i}{2}} = e^{\pm j\pi(\nu-\bar{\nu})T\frac{L_i}{L_p}} \xrightarrow{L_i/L_p<<1} 1$$

and (119)

$$\delta L_i = \sqrt{\left(\Delta\frac{L_i}{2}\right)^2 + (\kappa L_i)^2} \xrightarrow{L_i/L_p<<1} \kappa L_i \quad .$$

The proposed filtering structure present a design constraint that will be assumed in the device analysis: Equal spacing between coupling regions, already implied in figure 14. This constraint keeps the same spectral repetition period (FSR) generated in all sections (coupling region followed by a clear propagation region). Also implied in figure 14 is the symmetrical behavior of the coupling lengths with respect to the device center. This is not in fact an *a priori* constraint, but a consequence of the device reciprocity, as it was later noticed.

From the standpoint of easiness of implementation in a computer algorithm and time spent in the coefficient determination, it is better to apply a set of recursive polynomial-order step-down relations to the off-diagonal elements of the overall matrix in equation (116) than to apply polynomial identity process described earlier.

Table 2 – Coupling strengths $\zeta_i = \kappa L_i$ for various numbers of coupling regions (N).

N \ i	1	2	3	4	5	6	7	8
2	0.78540	0.78540	–	–	–	–	–	–
3	0.47766	0.61548	0.47766	–	–	–	–	–
4	0.33312	0.45228	0.45228	0.33312	–	–	–	–
5	0.25336	0.34236	0.37936	0.34236	0.25336	–	–	–
6	0.20365	0.26987	0.31188	0.31188	0.26987	0.20365	–	–
7	0.16995	0.22032	0.25859	0.27308	0.25859	0.22032	0.16995	–
8	0.14568	0.18499	0.21784	0.23688	0.23688	0.21784	0.18499	0.14568

In the polynomial-order step-down algorithm, after each step, it is obtained a coupling strength for the respective section and another polynomial, with its order reduced by one. This new polynomial encompasses the characteristics of the remainder of the structure. The process is repeated until the last coupling strength is obtained and happens as if the device is being traveled backwards.

These step-down relations are perfectly analogous to the ones obtained in the analysis of the Mach-Zehnder lattice filters [18-23] and the polynomial-order step-down algorithm is identical. A routine in MATLAB^{TM} was developed to find coupling strengths for various numbers of coupling regions. The routine script is in Appendix A. The required coupling strengths to achieve the filtering function with equally spaced

nulls were calculated for various numbers of coupling regions by using this routine and are summarized on Table 2.

Note in table 2 the symmetry of coupling strengths with respect to the center of the structure, as stated before.

Another fact, that will have a direct consequence in the sparse grating design, is that the sum of the coupling strengths in one row is equal to $\pi/2$. This is similar to the requirement for full polarization conversion obtained in the continuous grating case ($\kappa L = \pi/2$), except that for the sparse grating it has to be computed as the sum of the same product for each of the coupling regions.

The values obtained in table 2 are in a good agreement with the ones in [8], although they were determined by different techniques.

Figure 16 (b) shows the theoretical filtering function obtained for a 6-coupling region sparse-grating polarization converter device. Figure 16(a) shows the same channel "comb" as in figure 13 (a). Figure 16(c) shows the result of the channels being filtered by the function in figure 16(b). Comparison of figure 16(c) with figure 13(c) shows the higher selectivity in the passband and lower cross-talk in the whole detection band.

In figure 13(c), the periodic behavior of the filtering function spectrum may be observed, as channels +6 and -6 are filtered along with channel 0. That is the reason the filter is named spectral slicing filter.

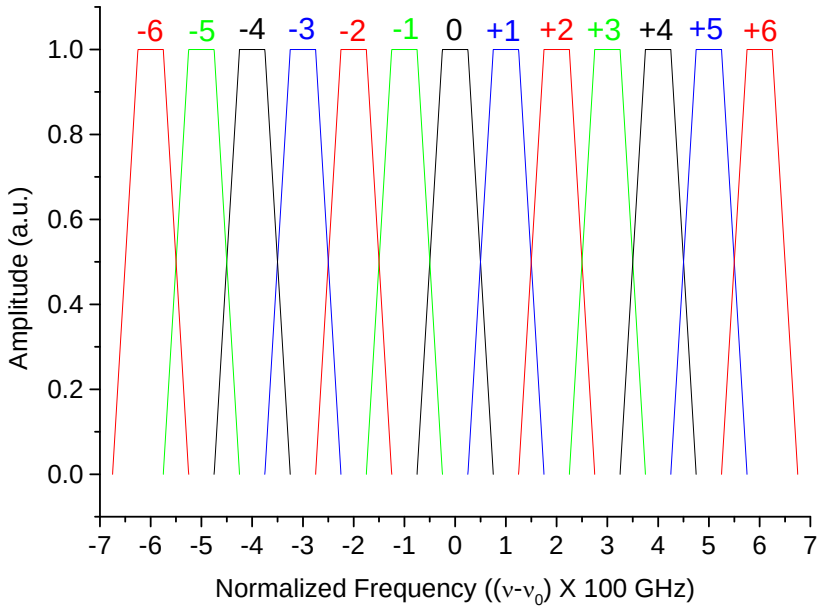

(a)

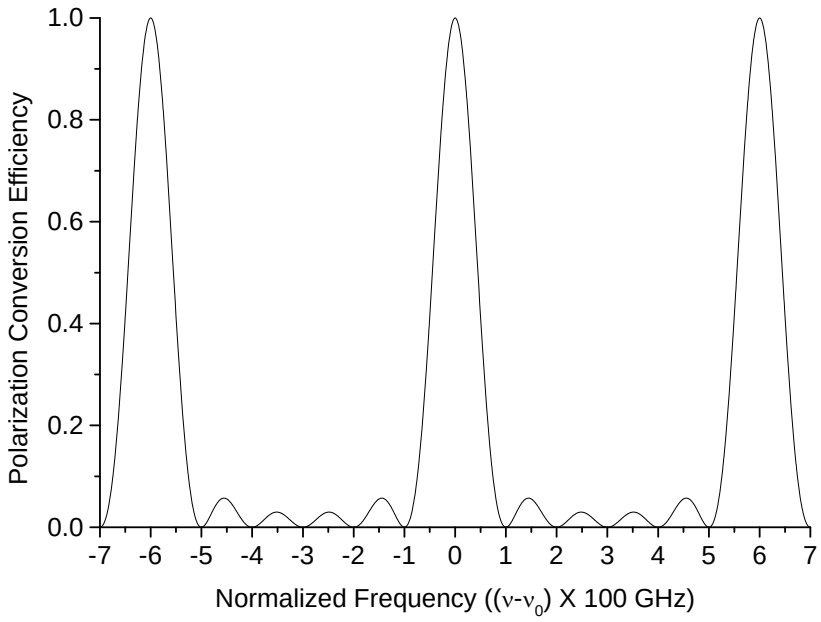

(b)

Fig. 16. Example of filtering performed by a sparse grating on the channel comb: (a) channel comb; (b) filtering function; (c) resulting spectrum.

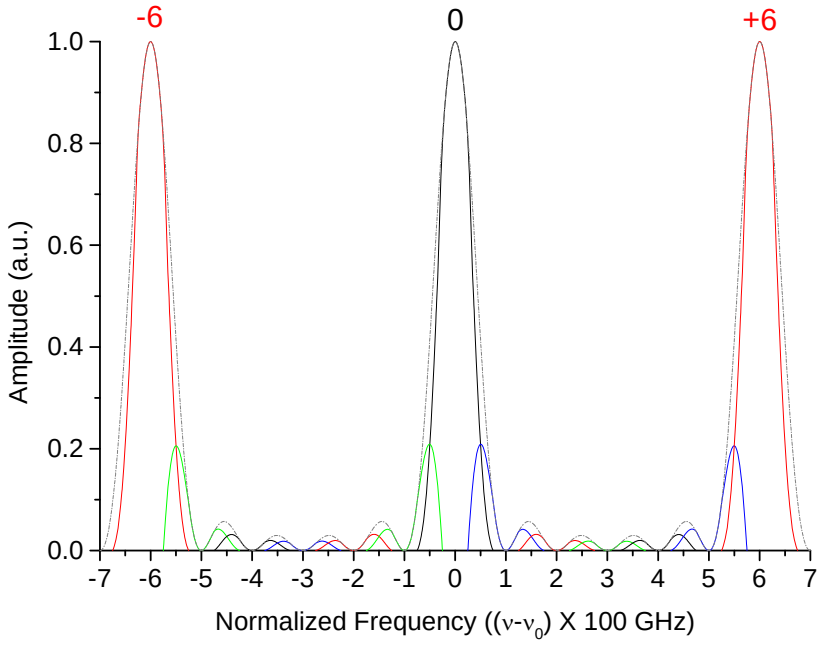

(c)

Fig. 16. Continued

C. Sparse Grating Filter Design

In order to design the sparse grating, the first parameter to be determined is the spatial period of the grating employed in the coupling regions. By using equation (95), and the values for the effective refractive indices for the modes at 1545 nm used before ($n_{TE} \approx n_e = 2.13828$; $n_{TM} \approx n_o = 2.21150$), it is obtained

$$\Lambda = \frac{\lambda_0}{|n_e - n_o|} = \frac{1.545\ \mu m}{|2.13828 - 2.21150|} = 21.1\ \mu \text{m} \ . \qquad (120)$$

To avoid increased complexity and cost in making a photolithography mask capable of showing a feature size with the accuracy required in equation (120), the

grating spatial period will be adopted as $\Lambda = 21\,\mu m$, this should not deviate much the phase-matched wavelength from the design value.

The second parameter is the distance between the coupling regions. This distance is related to the free-spectral range ($\Delta\nu_{FSR}$) or the filtering function spectral period (in frequency). By this definition, $\Delta\nu_{FSR}$ is the reciprocal of differential time delay experienced between both polarizations when propagating between coupling sections (unit delay), i.e.

$$\Delta\nu_{FSR} = \frac{1}{T} = \frac{c}{(n_{gTM} - n_{gTE})L} \quad . \tag{121}$$

The free-spectral range is also related to the frequency separation between channels and number of channels intended to fit in the stopband.

Following the previous 6-coupling region example with 100 GHz separation between channels, $\Delta\nu_{FSR}$ to fit 4 channels in the stopband, the physical separation between coupling regions is determined from equation (121) to be

$$L = \frac{c}{(n_{gTM} - n_{gTE})\Delta\nu_{FSR}} = \frac{2.9979\times10^{8}}{(2.26442 - 2.18267)\cdot 6.0\times10^{11}} = 6111.9\,\mu m \quad . \tag{122}$$

The third design parameter is the length of every coupling region. Once the number of channels in one free-spectral range has been chosen, the number of coupling regions is automatically determined. By looking up on table 2, the coupling strengths for each coupling are listed in the respective row.

Recall that the relationship between continuous and sparse grating lengths for full conversion is

$$\kappa L_{cont} = \frac{\pi}{2} = \sum_{i=1}^{N} \kappa L_i \tag{123}$$

where L_{cont} is the length of the continuous grating, L_i is the length of each of the coupling regions in the sparse grating and N is the number of coupling regions.

Therefore, if the same parameters used in the continuous grating fabrication process to obtain full polarization conversion are also used in the sparse grating fabrication, the same coupling coefficient should be obtained in both situations. Therefore, the sum of the coupling region lengths in the sparse case will be equal to the length of the continuous grating. That along with the coupling strengths that should be attained (from table 2) allows determining the length (or the number of grating periods) of each coupling region.

Previous results in our group obtained full polarization conversion for continuous gratings with 500 grating periods (1.05 cm) [24]. This will be the length used to finalize the design. For the 6-coupling region, used throughout this design example, it is determined

$$\begin{aligned} L_1 = L_6 &= 1361.3\ \mu m \text{ (65 grating periods)} \\ L_2 = L_5 &= 1803.9\ \mu m \text{ (86 grating periods)} \\ L_3 = L_4 &= 2084.8\ \mu m \text{ (99 grating periods)} \ . \end{aligned} \tag{124}$$

Recall that the elements in table 2 were determined with the approximation infinitesimal length for the coupling regions. Unfortunately the coupling regions almost never can be considered infinitesimal due to the finite value of the coupling coefficient (κ).

When the lengths of the coupling regions are taken into account, the approximations in equation (119) do not hold anymore. The associated transmission matrices for the coupling regions will show complex exponentials multiplied by trigonometric functions that are both functions of the frequency detuning.

Another consequence is that the distance between coupling regions cannot be accounted from end of the preceding to begin of the next. Due to the fact that the coupling regions are now distributed over some length, the distance between them should be accounted from center-to-center instead of edge to edge.

Using the calculated lengths in equations (122) and (124), substituting them in equation (116), the full transmission matrix for the structure is calculated. Figure 17 shows the spectral response obtained with this procedure.

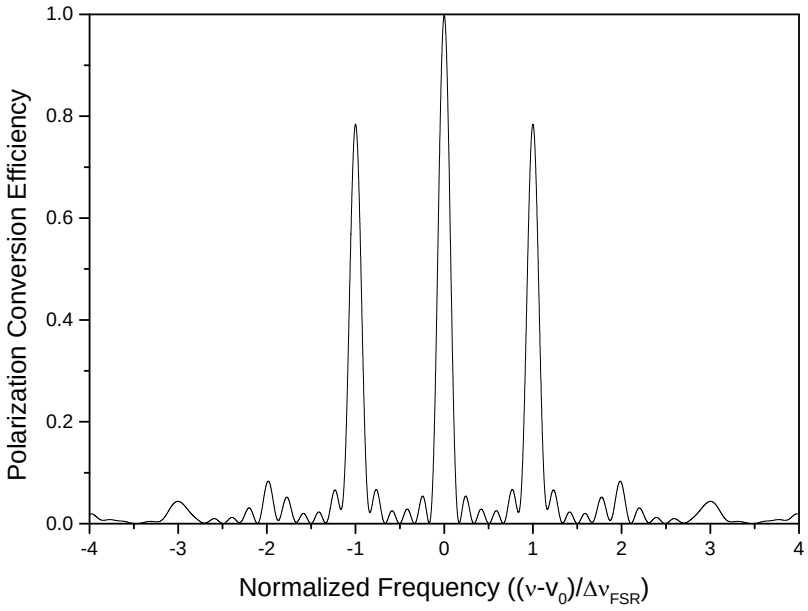

Fig. 17. Filtering response obtained with six finite-length coupling regions.

A sinc-like envelope in the frequency response can be noticed when contrasted with the infinitesimal coupling regions result. It constitutes a more realistic spectral response and will be used as the theoretical reference.

D. Tuning of the Phase-Matched Wavelength

As seen through the design procedure, the spatial period of the strain-inducing gratings is defined with some phase matched wavelength in mind. Once it has been defined by a photolithographic process during the fabrication, the spacing between two SiO_2 strain pads becomes fixed and the phase-matched wavelength cannot be changed by a mechanical mean anymore. The only degree of freedom left for changing the phase-matched wavelength (tuning) is through the variation of the term $(n_{TE} - n_{TM})$, called mode birefringence, as can be seen from equation (95).

There are fundamentally two ways of performing the phase-matched wavelength tuning: through the temperature dependence of the crystal birefringence or through eletrooptical tuning of the birefringence.

Heating or cooling the sample in a controlled way will provide a tuning mechanism for the phase-matched wavelength.

The temperature dependence of the birefringence for bulk $LiNbO_3$ in 1.5 μm wavelength region is $3.45\times10^{-5}\ {}^{o}C^{-1}$ [25]. But it is not only the bulk substrate birefringence temperature dependence the responsible for change, there is also the mode effective birefringence effect. Although the thermal tuning principle does not provide a fast mean, it enables some sort of fine tuning on the filter response.

In order to use the highest possible electro-optic coefficient in $LiNbO_3$ (r_{33}) for changing the refractive indices, an electric field aligned along the crystalline z axis should be applied. Considering the sample orientation and waveguide placement with respect to the crystalline axes (*x-cut*, *y-propagation*), electrodes must be placed alongside the waveguide. They will have a gap g between them and the waveguide should be centered entirely in this gap.

When a voltage (V_m) is applied across the electrodes, it will produce an electric field mostly aligned along the z axis in the region the of waveguide. Since the applied electric field is not uniform nor aligned in the same direction (z) when crossing the region in space where the light electric field is distributed, an overlapping factor between both should be introduced to account for the effective change in the guided mode refractive indices [12]. After this, the electric field intensity along z may be written as

$$E_z = \Gamma \frac{V_m}{g} \tag{125}$$

Applying the electric field in equation (125) to equation (61), considering the proposed field and waveguide relative orientation, the refractive index for each of the polarization modes propagating in the waveguide may be written as

$$n_{TM} = n_o - \tfrac{1}{2}\Gamma_{TM} n_o^3 r_{13} \frac{V_m}{g}$$
$$\text{and} \tag{126}$$
$$n_{TE} = n_e - \tfrac{1}{2}\Gamma_{TE} n_e^3 r_{33} \frac{V_m}{g}$$

where different overlap factors for the *TE* and *TM* modes were assumed, since the electric field distribution for these modes are different.

From equations (126) and (95) the rate of change with voltage for the phase-matched wavelength may be written as

$$\frac{d\lambda}{dV_m} = \frac{1}{2}(\Gamma_{TM} n_o^3 r_{13} - \Gamma_{TE} n_e^3 r_{33})\frac{\Lambda}{g} \tag{127}$$

where Λ is the spatial period of the grating.

E. Polarization Independent Topology

In the straight channel waveguide with a polarization conversion grating on top, part of the light will exit the device on one polarization and the other part of the light on the orthogonal polarization. Therefore, in order to observe either one of them individually, a polarization filter (polarizer) must be included after the device, eliminating the undesired polarization. The addition of one component increases the cost, complexity and the insertion loss of the filter as a whole.

A topology in which the polarizer would be dispensable without distorting the filter response with respect to the polarized straight channel response is highly desirable. Avoiding the use of a polarizer requires the response to be the same no matter which polarization is input to the device, hence the name polarization independent.

One way to accomplish it, is by using the asymmetric Mach-Zehnder interferometer [26]. The device is called asymmetric because there is an imbalance in the

optical path for both arms of the interferometer. The interferometer is fabricated so that the imbalance is equal to a phase difference of π (or $\lambda/2$) between the two arms.

Another particularity of this structure is that the strain-inducing grating in one of the arms is shifted half of the grating spatial period ($\Lambda/2$) with respect to the one on the other arm. Figure 18 shows a schematic diagram of the described configuration.

The best way to analyze this device is by using Jones calculus, where both polarizations may be treated at the same step of the calculation by using matrix multiplications as the light wave propagates through the device.

In order to ease the analysis, some reference planes must be defined along the sample. They are also pictured in figure 18 and marked by the numbers 1,2,3 and 4.

At the Y-branch, power is split into half and directed to each arm. Hence the electric field amplitude after the branch is written

$$\begin{aligned}\begin{pmatrix} E_{TE} \\ E_{TM} \end{pmatrix}_{i-B}^{u} &= 1/\sqrt{2}\begin{pmatrix} E_{TE} \\ E_{TM} \end{pmatrix}_{i} \\ \begin{pmatrix} E_{TE} \\ E_{TM} \end{pmatrix}_{i-B}^{l} &= 1/\sqrt{2}\begin{pmatrix} E_{TE} \\ E_{TM} \end{pmatrix}_{i}\end{aligned} \tag{128}$$

where the superscript u denotes fields in the upper arm and l in the lower arm. Subscript *i* denotes at "input" and i-*B* denotes at input branch.

Assuming the grating is centered with respect to the interferometer arms, at reference plane 1, light that has propagated in the upper arm accumulates a phase difference of $\pi/2$ with respect to light that propagated in the lower arm due to the described interferometer asymmetry.

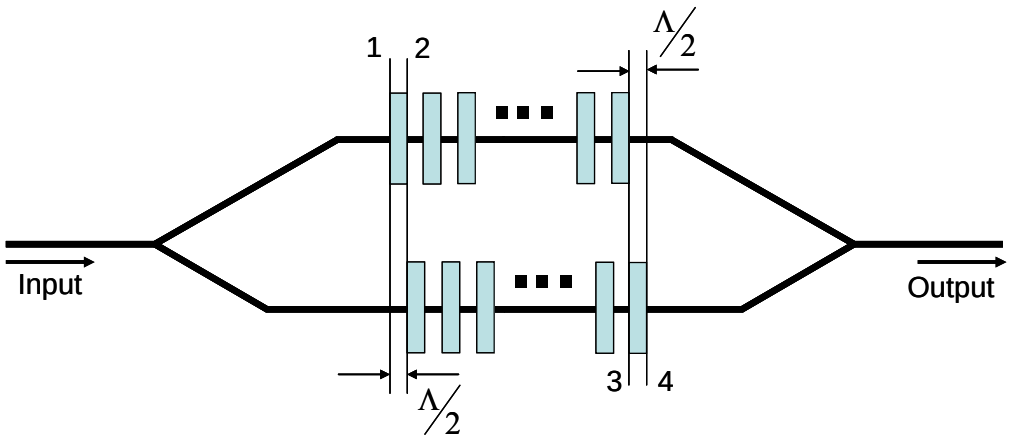

Fig. 18. Schematic diagram of an asymmetric Mach-Zehnder interferometer with strain-inducing gratings on each arm.

Therefore using the phase in the lower arm as reference

$$\begin{pmatrix} E_{TE} \\ E_{TM} \end{pmatrix}_1^u = 1/\sqrt{2} \begin{pmatrix} e^{-j\pi/2} & 0 \\ 0 & e^{-j\pi/2} \end{pmatrix} \begin{pmatrix} E_{TE} \\ E_{TM} \end{pmatrix}_i$$
$$\begin{pmatrix} E_{TE} \\ E_{TM} \end{pmatrix}_1^l = 1/\sqrt{2} \begin{pmatrix} E_{TE} \\ E_{TM} \end{pmatrix}_i . \tag{129}$$

At reference plane 2, light in the upper arm is already in the sparse grating region while light in the lower arm propagated a distance $\Lambda/2$ before reaching reference plane 2. The effect for the sparse grating region will be accounted at the respective reference plane light exits it. Hence

$$\begin{pmatrix} E_{TE} \\ E_{TM} \end{pmatrix}_2^u = 1/\sqrt{2} \begin{pmatrix} e^{-j\pi/2} & 0 \\ 0 & e^{-j\pi/2} \end{pmatrix} \begin{pmatrix} E_{TE} \\ E_{TM} \end{pmatrix}_i$$
$$\begin{pmatrix} E_{TE} \\ E_{TM} \end{pmatrix}_2^l = 1/\sqrt{2} \begin{pmatrix} e^{-j\beta_{TE}\frac{\Lambda}{2}} & 0 \\ 0 & e^{-j\beta_{TM}\frac{\Lambda}{2}} \end{pmatrix} \begin{pmatrix} E_{TE} \\ E_{TM} \end{pmatrix}_i . \tag{130}$$

At reference plane 3, light traveling in the upper arm leaves the sparse grating section, while light in the lower arm is still traveling through it. The same way, the effect of the grating on the lower arm will be accounted at the reference plane it leaves it, then according to equation (116)

$$\begin{pmatrix} E_{TE} \\ E_{TM} \end{pmatrix}_3^u = 1/\sqrt{2} \begin{pmatrix} A(z) & jB^R(z) \\ jB(z) & A^R(z) \end{pmatrix} \begin{pmatrix} e^{-j\pi/2} & 0 \\ 0 & e^{-j\pi/2} \end{pmatrix} \begin{pmatrix} E_{TE} \\ E_{TM} \end{pmatrix}_i$$
$$\begin{pmatrix} E_{TE} \\ E_{TM} \end{pmatrix}_3^l = 1/\sqrt{2} \begin{pmatrix} e^{-j\beta_{TE}\frac{\Lambda}{2}} & 0 \\ 0 & e^{-j\beta_{TM}\frac{\Lambda}{2}} \end{pmatrix} \begin{pmatrix} E_{TE} \\ E_{TM} \end{pmatrix}_i . \quad (131)$$

At reference plane 4, light in the upper arm had traveled an additional distance of $\Lambda/2$ and light in the lower arm is exiting the sparse grating region, which makes

$$\begin{pmatrix} E_{TE} \\ E_{TM} \end{pmatrix}_4^u = 1/\sqrt{2} \begin{pmatrix} e^{-j\beta_{TE}\frac{\Lambda}{2}} & 0 \\ 0 & e^{-j\beta_{TM}\frac{\Lambda}{2}} \end{pmatrix} \begin{pmatrix} A(z) & jB^R(z) \\ jB(z) & A^R(z) \end{pmatrix} \begin{pmatrix} e^{-j\pi/2} & 0 \\ 0 & e^{-j\pi/2} \end{pmatrix} \begin{pmatrix} E_{TE} \\ E_{TM} \end{pmatrix}_i$$
$$\begin{pmatrix} E_{TE} \\ E_{TM} \end{pmatrix}_{o-B}^l = 1/\sqrt{2} \begin{pmatrix} A(z) & jB^R(z) \\ jB(z) & A^R(z) \end{pmatrix} \begin{pmatrix} e^{-j\beta_{TE}\frac{\Lambda}{2}} & 0 \\ 0 & e^{-j\beta_{TM}\frac{\Lambda}{2}} \end{pmatrix} \begin{pmatrix} E_{TE} \\ E_{TM} \end{pmatrix}_i . \quad (132)$$

Right before recombination, light in the upper arm have again accumulated a phase difference of $\pi/2$ with respect to light that propagated in the lower arm due to the interferometer asymmetry, yielding

$$\begin{pmatrix} E_{TE} \\ E_{TM} \end{pmatrix}_{o-B}^u = 1/\sqrt{2} \begin{pmatrix} e^{-j\pi/2} & 0 \\ 0 & e^{-j\pi/2} \end{pmatrix} \begin{pmatrix} e^{-j\beta_{TE}\frac{\Lambda}{2}} & 0 \\ 0 & e^{-j\beta_{TM}\frac{\Lambda}{2}} \end{pmatrix} \begin{pmatrix} A(z) & jB^R(z) \\ jB(z) & A^R(z) \end{pmatrix} \begin{pmatrix} e^{-j\pi/2} & 0 \\ 0 & e^{-j\pi/2} \end{pmatrix} \begin{pmatrix} E_{TE} \\ E_{TM} \end{pmatrix}_i$$
$$\begin{pmatrix} E_{TE} \\ E_{TM} \end{pmatrix}_{o-B}^l = 1/\sqrt{2} \begin{pmatrix} A(z) & jB^R(z) \\ jB(z) & A^R(z) \end{pmatrix} \begin{pmatrix} e^{-j\beta_{TE}\frac{\Lambda}{2}} & 0 \\ 0 & e^{-j\beta_{TM}\frac{\Lambda}{2}} \end{pmatrix} \begin{pmatrix} E_{TE} \\ E_{TM} \end{pmatrix}_i . \quad (133)$$

The components of the output field, after light travels through the interferometer and recombines at the second Y-branch is given by

$$\begin{pmatrix} E_{TE} \\ E_{TM} \end{pmatrix}_o = 1/\sqrt{2}\left[\begin{pmatrix} E_{TE} \\ E_{TM} \end{pmatrix}_{o-B}^{u} + \begin{pmatrix} E_{TE} \\ E_{TM} \end{pmatrix}_{o-B}^{l}\right] . \tag{134}$$

Thus carrying out the matrix multiplications in equation (133) and adding the results according to equation (134), it is obtained

$$\begin{pmatrix} E_{TE} \\ E_{TM} \end{pmatrix}_o = 1/2 \begin{pmatrix} A(z)\left[e^{-j\pi}+1\right]e^{-j\beta_{TE}\frac{\Lambda}{2}} & j\left[e^{-\left(j\pi+\beta_{TE}\frac{\Lambda}{2}\right)}+e^{-j\beta_{TM}\frac{\Lambda}{2}}\right]B^R(z) \\ j\left[e^{-\left(j\pi+\beta_{TM}\frac{\Lambda}{2}\right)}+e^{-j\beta_{TE}\frac{\Lambda}{2}}\right]B(z) & A^R(z)\left[e^{-j\pi}+1\right]e^{-j\beta_{TM}\frac{\Lambda}{2}} \end{pmatrix} \begin{pmatrix} E_{TE} \\ E_{TM} \end{pmatrix}_i .$$

(135)

Which may be further reduced to

$$\begin{pmatrix} E_{TE} \\ E_{TM} \end{pmatrix}_o = 1/2 \begin{pmatrix} 0 & j\left[-e^{-j\beta_{TE}\frac{\Lambda}{2}}+e^{-j\beta_{TM}\frac{\Lambda}{2}}\right]B^R(z) \\ j\left[-e^{-j\beta_{TM}\frac{\Lambda}{2}}+e^{-j\beta_{TE}\frac{\Lambda}{2}}\right]B(z) & 0 \end{pmatrix} \begin{pmatrix} E_{TE} \\ E_{TM} \end{pmatrix}_i . \tag{136}$$

It should be observed that no unconverted light appears at the output. The power associated with them is radiated into the substrate instead of remaining guided. Since after recombining the waveguide modes travel without exchanging power between them, the total power at the output will be the sum of the power on each mode, i.e.

$$P_{out} = \frac{1}{4}\left\{E_{TE-o}E_{TE-o}^{*} + E_{TM-o}E_{TM-o}^{*}\right\} = \frac{|B(z)|^2}{4}\left\{2-2\cos\left[\frac{2\pi}{\lambda}\left(n_{TE}-n_{TM}\right)\frac{\Lambda}{2}\right]\right\}\left(P_{TE-i}+P_{TM-i}\right) \tag{137}$$

since $B(z)B^{*}(z) = B^{R}(z)\left(B^{R}(z)\right)^{*} = \left|B(z)\right|^{2}$, finally yielding

$$P_{out} = \frac{\left|B(z)\right|^{2}}{2}\left\{1-1\cos\left[\frac{2\pi}{\lambda}\left(n_{TE}-n_{TM}\right)\frac{\Lambda}{2}\right]\right\}\left(P_{TE-i}+P_{TM-i}\right) . \qquad (138)$$

Equation (138) is independent from the polarization state of the input, moreover, for the phase-matched wavelength $P_{out} = \left|B(z)\right|^{2}\left(P_{TE-i}+P_{TM-i}\right)$, giving the exact same response for the converted power in the straight channel waveguide sparse grating.

For wavelengths other than the phase-matched, the cosine term in equation (138) will have a value greater than -1 and the efficiency at the output will not be maximum.

Thus the asymmetric Mach-Zehnder Interferometer, in the way it was depicted, enables to realize the same filtering function obtained in the straight channel waveguide and eliminates the need for a polarizer at the output of the device.

CHAPTER IV

DEVICE FABRICATION

The fabrication processes for channel waveguides, continuous-grating polarization mode converters on straight channel waveguides, sparse-gratings on channel waveguides and the sparse-gratings on the asymmetric Mach-Zehnder Interferometer are described in this chapter.

A. Ti Diffused Channel Waveguides in $LiNbO_3$ (Ti:$LiNbO_3$)

It is usual to develop a waveguiding channel in lithium niobate by metal diffusion [27]. The most common and successful metal, being used a long time for that purpose, is Titanium (Ti). In contrast to other ways of developing the waveguiding region, for example proton exchange, Ti diffusion is of particular interest to this work because of its ability to support fundamental mode propagation for both polarizations, TE and TM, which is not the case for proton exchange.

The fabrication of straight channel waveguides starts with dicing the substrate wafer ($LiNbO_3$) into samples of proper size and crystal orientation.

Three-inch diameter, one-millimeter thick, x-cut $LiNbO_3$ crystal wafer supplied by Crystal Technology Inc. (Palo Alto, CA) is used. Since light propagation will be along the crystalline y-axis, orientation flats located at the wafer rim showing the crystalline axes orientation must be identified prior to dicing. The wafer is then diced into 12 mm wide (in the z-direction) by 43 mm long (in the y-direction) for straight

channel waveguides to be used with sparse gratings. Samples with the same width but smaller in length (22 mm) are also diced to be used with a 10.5 mm long continuous grating. These smaller samples are intended to optimize the conditions of producing the strain-inducing structure in the continuous grating case and use the same parameters latter on for the sparse grating.

After dicing, samples were cleaned using soapy water, organic solvents and DI water.

A Titanium film of about 1250Å thick was deposited onto the clean substrate surface by a DC sputtering process.

After Ti-film deposition, the patterns of channel waveguides are delineated by a positive photolithographic process on the Ti film. This process uses the AZ-5214-E-IR photoresist produced by Clariant.

Developed photoresist patterns are then checked to confirm that the desired pattern was obtained. Samples that pass the check are then cleaned with the help of a light plasma (low power O_2 plasma-descum) to remove any possible photoresist residue left on exposed areas. A small amount of the photoresist on the patterns is also removed during this process.

The plasma ashing process is followed by hardbaking at 135°C for 15 minutes to harden the photoresist and prepare it to withstand the Reactive Ion Etching (RIE) process. It is done inside the same chamber, right after ashing and without breaking the vacuum.

Reactive ion etching (RIE) is then used to remove almost all of the titanium film, leaving only portions where the hardened photoresist pattern is present. Since it is an

anisotropic etching process, most of the features are defined by this process with very little distortion from the desired pattern.

On the portions not covered with photoresist, the etching is not complete as a precaution in avoiding damage to the substrate, which may also be etched by the gas mixture used. Therefore, the remaining titanium on the uncovered areas is removed by wet etching with hydrofluoric acid (HF) diluted in De-Ionized (DI) water in the proportion 1:30 by volume. This process is isotropic and should be very well controlled to avoid overetching, which would result in increased waveguide scattering losses and also to avoid underetching, which would not provide much index increment, leaving the mode loosely guided. Typical etching times are on the order of less than 5 seconds, depending on the remaining titanium thickness.

Upon finishing the etching, the photoresist is removed by immersing in a photoresist stripper bath (Clariant AZ 300T or AZ 400T) heated to the temperature range between 95°C and 100°C for 15 minutes. The samples are then cleaned with liquid solvents.

The Ti patterns for both straight channel waveguides and asymmetric Mach-Zehnder interferometers were designed to be 7μm, which upon diffusion should allow single mode operation in each polarization. In order to check the Ti strips width, a 1000X magnification optical microscope is used along with a calibrated scale on the eyepiece (0.625 μm/division). Widths are measured at different locations on the sample and their average is taken as the reference value for the width.

The Ti film thickness is determined from the average of measurements taken at different places on the sample by using a Dektak^3 Surface Profile Measuring System.

When Ti strips desired thickness and width values are obtained sample may be diffused.

Sample is loaded in the furnace quartz tube using an alumina boat. Sample is kept at 1035 °C in wet atmosphere by bubbling compressed breathing air in DI water before flowing it into the furnace. The purpose of the wet atmosphere is to provide an increased oxygen partial pressure that suppresses the observed lithium oxide (Li_2O) out-diffusion [28]. Diffusion time was optimized to 13h for the Ti film thickness (1250 Å).

Finally, both end facets of the sample were polished perpendicular to the waveguides in order to minimize scattering losses on those edges when coupling light to them.

B. Uniform-Grating TE-TM Polarization Converters

Uniform-grating TE-TM polarization converters were fabricated on x-cut, y-propagating, twelve millimeter wide by twenty two millimeter long samples. A continuous strain-induced grating was added on top of a single-mode, Ti-diffused straight channel waveguide. The sample end facets were already polished to enable light coupling.

All the procedures already described in the previous section were used to obtain the sample with low-loss single-mode straight channel waveguides.

After the waveguides had been produced, a spatially periodic strain-induced refractive index grating 10.5 mm long (500 grating spatial periods) was fabricated on top of it by following the procedure described next.

The $LiNbO_3$ sample containing the waveguides was heated up to 389°C in the e-beam chamber, while under vacuum, by using a pair of halogen lamps as the heat source. The voltage applied to the lamp was adjusted to keep an approximately constant heating rate. The sample was then kept at the final temperature by an on/off controller and a 1.7μm thick SiO_2 film was deposited by e-beam evaporation. A small constant flow of oxygen (about 1 sccm) was kept during deposition to avoid oxygen out-diffusion from the lithium niobate.

After completing the SiO_2 deposition, the sample was kept inside the chamber with the O_2 flowing in, until it reached room temperature.

Using positive photolithographic process, a uniform periodic pattern was delineated over the SiO_2 strain film. The parameters for this patterning are different from the parameters used in the Ti patterning, since both films had very dissimilar thicknesses (much thicker SiO_2) and reflectivities in the UV region.

Following the patterning, sample was treated O_2 plasma-descum and then hardbaked at 135°C in vacuum for 20 minutes. The SiO_2 layer was dry etched in the Oxford Plasmalab system for about one hour. The remaining non-etched SiO_2 film was removed by means of a wet-etching in a buffered oxide etch (BOE) for about 40 seconds.

The photoresist left on the sample after RIE was then removed by immersing the sample in photoresist stripper bath (Clariant AZ 300T or AZ 400T) heated to the temperature range between 95°C and 100°C for 20 minutes.

Sample was then inspected under the optical microscope to check grating period and pattern integrity.

After completion, sample was ready for optical testing.

C. Tunable Sparse-Grating TE-TM Polarization Converters

The tunable sparse-grating TE-TM polarization converters were produced on an x-cut, y-propagating, twelve-millimeter-wide by forty three-millimeter-long sample.

To enable electro-optic tuning of the phase-matched wavelength, before the strain grating was produced, a couple of electrodes patterns placed alongside the waveguide were deposited by multiple metal layer e-beam evaporation. Electrode patterns were generated using an image reversal photolithographic process. Figure 19 shows a schematic diagram of the device.

Aiming at avoiding additional loss caused by field attenuation on the electrodes, the gap between them has to be carefully aligned in a way the center of the gap coincides with the center of the waveguide. The gap between electrodes was designed to be 17μm.

After pattern developing, the samples were cleaned with O_2 plasma descum for 3 minutes, in order to remove residual photoresist that would prevent the metallic film to stick well to the substrate. No hardbaking is used in this process.

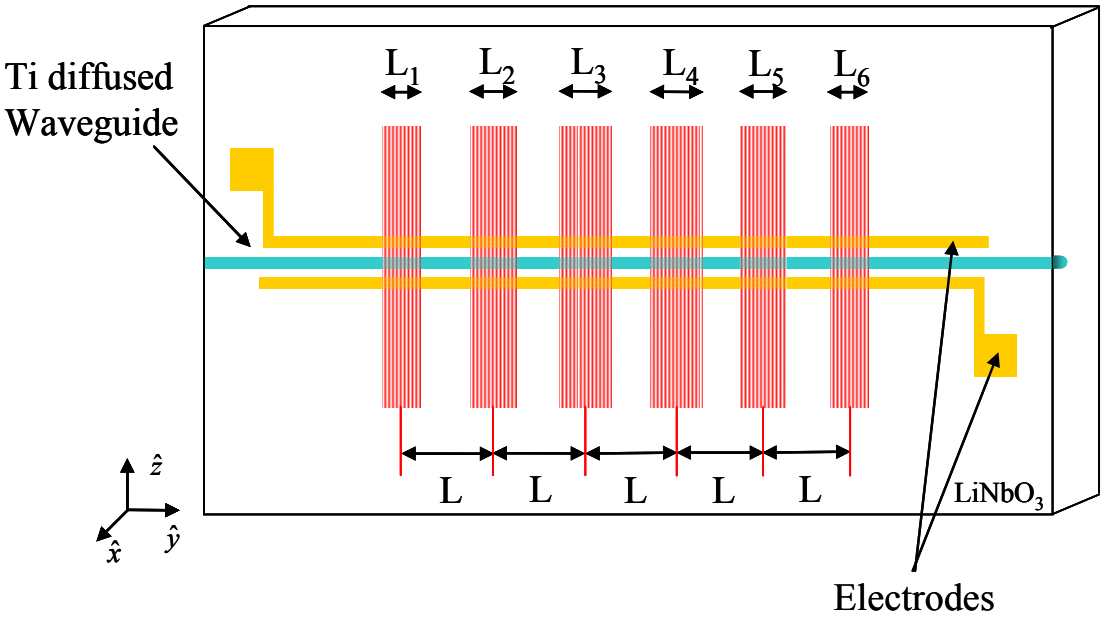

Fig. 19. Schematic diagram of a tunable sparse-grating TE-TM converter on a channel waveguide.

After the descum process, samples were loaded in the e-beam chamber and three-metal layers were deposited. First a 400Å Chromium layer was deposited to improve electrode adherence to the substrate. Without breaking the vacuum an 800Å gold layer was deposited to improve electrode conductivity. Finally a 600Å Ti layer was deposited to avoid gold diffusion into the SiO_2 layer when sample is heated up to deposition temperature.

After deposition, metal electrode patterns were obtained by lifting-off the photoresist layer. This was done by immersing the sample in acetone and sonicating.

The remainder of the process is concerned with producing the sparse grating on top of the waveguides. The procedure parameters for that are identical to the one

described in producing the continuous grating described in the previous section: 1.7 μm thick SiO_2 film deposited at 389 ^oC and patterned at room temperature. The only difference is the pattern, now a 6-coupling region sparse grating. Details for the pattern dimensions are provided in appendix B.

The distance between adjacent coupling region centers in the design of this pattern had to be readjusted with respect to design parameters presented in the previous chapter. This happened because the same pattern was also meant to be used in the asymmetric Mach-Zehnder interferometer (polarization independent topology) and space on the smallest arm was limited to 24 millimeters.

Distance between centers was then reduced from the value of 6111.9 μm, given in equation (122) to 4368 μm, causing the value of $\Delta\nu_{FSR}$ to increase from 600 GHz to 839.55 GHz and spacing between nulls in the stopband to increase from 100 GHz to 139.93 GHz. With these new values the proof of concept can still be made, and future developments can design new asymmetric interferometer capable of accommodating the sparse-grating design presented in the previous chapter.

D. Polarization Independent Sparse-Grating Filter

The polarization independent sparse-grating filter was also produced on an x-cut y-propagating $LiNbO_3$ substrate. Samples were cut 14mm wide by 53mm long. The asymmetric Mach-Zehnder interferometer (MZI) pattern was obtained from Mask EMF-16 that was designed previously.

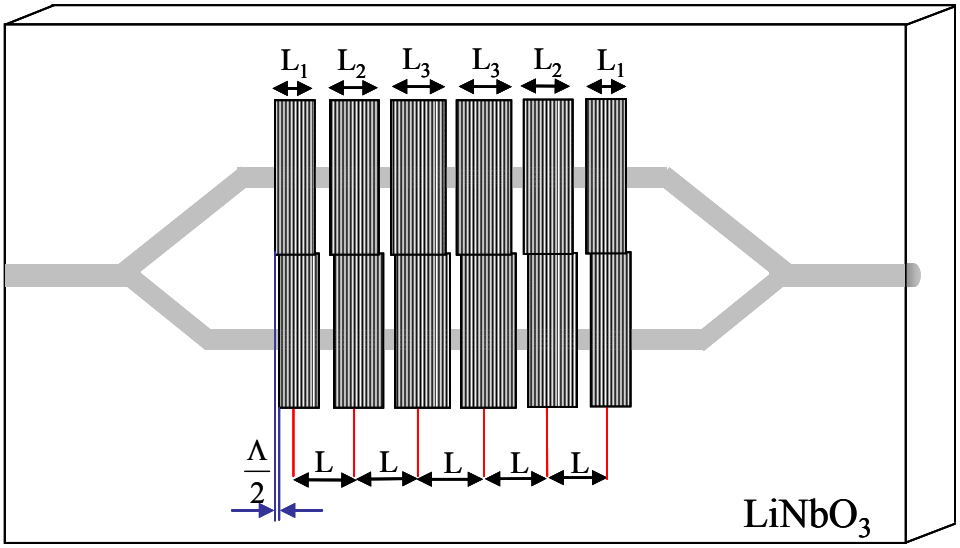

Fig. 20. Schematic diagram of a polarization independent sparse-grating filter.

Figure 20 shows a schematic diagram of the polarization independent sparse grating filter.

The fabrication procedure for the polarization independent sparse-grating filter was exactly the same described previously for the straight channel waveguide polarization converters. The exception is that the pattern for the waveguides is now the asymmetric MZI instead.

Ti-diffused waveguides in an asymmetric Mach-Zehnder interferometer were produced on a $LiNbO_3$ substrate by diffusing a 1240Å thick, DC-sputtered Ti film at 1035°C for 13 hours.

The six-coupling-region sparse strain-inducing SiO_2 grating was produced with a procedure identical to the one described in the previous section. Now there are two sets

of gratings, one for each arm of the interferometer, that are shifted half of the grating spatial period ($\Lambda/2$) from each other. Appendix C shows the dimension details in the mask pattern.

Once the waveguides were produced, the end facets were polished and optical characterization of the sample was carried out. Next, the sparse strain-induced gratings were fabricated on a SiO_2 film that was 1.7 μm thick, and was deposited using by e-beam while the sample being kept at 389°C.

Upon finishing the procedure, sample was ready for optical testing.

CHAPTER V

OPTICAL TESTING AND RESULT ANALYSIS

Once the samples were fabricated, they followed to optical testing and various characteristics were measured. This chapter is intended mainly for presenting the measurement setups, results and analyses of the results obtained by optically testing the fabricated devices. Also, suggestions for future extension on the work developed here are made.

A. Ti Diffused Straight Channel Waveguides in $LiNbO_3$ (Ti:$LiNbO_3$)

The first building block for the realization of the sparse grating filter is the waveguide where the light will propagate. It must present single mode propagation for the filter desired wavelength band of operation, low loss and highest possible overlap between TE and TM polarization modes. All the fabrication processes employed in obtaining the device have an influence on the waveguide being able to simultaneously satisfy those criteria. There is a set of parameters that should be closely monitored and controlled during the waveguide fabrication process to help achieve those goals. The Ti film thickness, patterned waveguide width, the Ti diffusion temperature and duration as well as the atmosphere developed in the diffusion furnace have profound effects in the quality of the obtained waveguide.

Therefore, before fabricating the filter waveguides themselves, fabrication and test experiments were conducted to help characterize and optimize the influence of those

parameters in straight channel waveguides. Once optimized, they were transferred to the fabrication process of the filter waveguides.

The optical loss increment in a system due to the inclusion of a component is called insertion loss of the device. Therefore, a comparison of measured values of optical power at same reference plane before and after the inclusion of the device will enable to determine this performance parameter. It is usually expressed in the form of a logarithmic ratio in decibels (dB) as

$$IL = -10 \log \frac{P_{with}}{P_{without}} \quad \text{(dB)} \tag{139}$$

where P_{with} and $P_{without}$ are the power levels measured at the sample output reference plane after and before including the waveguide in the light path, respectively.

Figure 21 shows a schematic diagram of the test setup used for the optical insertion loss measurement.

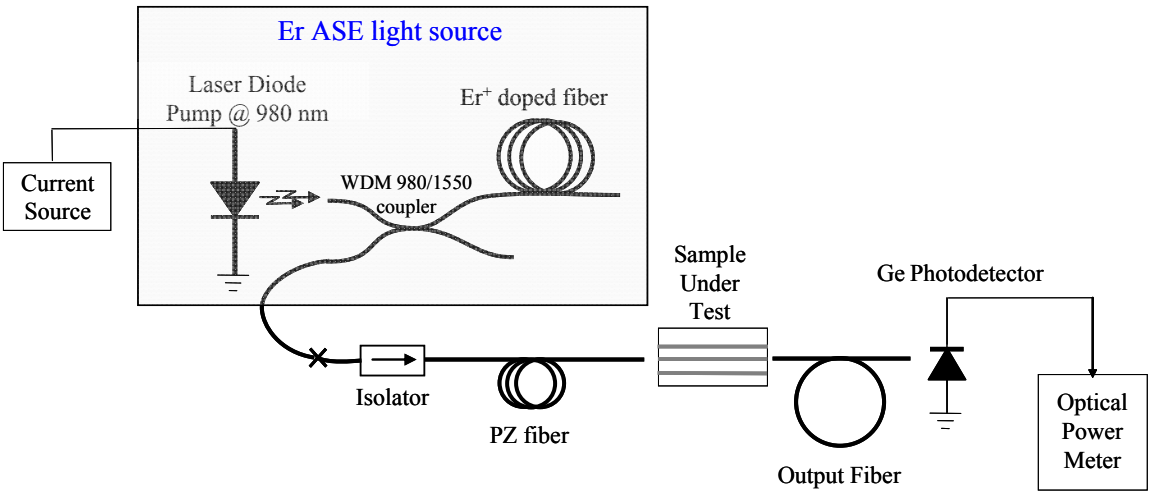

Fig. 21. Schematic diagram of the insertion loss test set up.

The light source was an Amplified Spontaneous Emission (ASE) Erbium-Doped Fiber (EDF) pumped in the backward configuration. It was composed of a 5m long Erbium-Doped Fiber (EDF) pumped by a 980nm Laser Diode (LD) (SDL Optics Inc. Model: SDLO-2400-090) through a 980/1550nm WDM coupler. An optical isolator (Kaifa Technology, Model: IS-A-55-B-A-11) with isolation in excess of 38dB of was connected at the output of the coupler to prevent self-oscillation (lasing). The broadband ASE light was butt-coupled to one of the sample's end facet through a PZ^{TM} fiber that could be axially rotated to select either a TE or TM polarization being input to the sample.

An x-y-z translation stage equipped with differential micrometric screws from Line Tool Co., Allentown, PA was used to hold and precisely manipulate the position of the sample with respect to the input fiber, enabling to optimize optical power coupling to the waveguides being tested.

After propagating through the sample, light was again butt-coupled, this time to a single mode optical fiber (Corning SMF-28^{TM}) at the sample opposite end facet. Light emerging from the output fiber is directed to a Ge detector from Newport (Model 818-IR), having its power level measured by an optical power meter, also from Newport (Model 1825-C).

Insertion losses for 7 μm wide straight channel waveguides fabricated on two 12 mm wide by 22 mm long samples (RD01 and RD02) for different the diffusion durations are summarized in table 3.

Table 3. Channel waveguides insertion losses for TE and TM polarizations under different diffusion durations.

Sample		RD 01		RD 02	
Ti thickness (Å)		1257		1264	
Diffusion Temperature (^{o}C)		1035		1035	
Polarization Mode		TE	TM	TE	TM
Diffusion Duration	11 h	2.53 dB	2.17 dB	2.58 dB	2.05
	12 h = (11+1) h	2.07 dB	1.79 dB	1.98 dB	1.82 dB
	13 h = (11+1+1) h	1.84 dB	1.64 dB	1.8 dB	1.59 dB

Diffusion duration started being timed when furnace temperature reached the desired set value, i.e. after the warm up time, although the sample was already in the furnace, was neglected, because little diffusion, compared to the full time, occurs.

After the initial diffusion of 11 hours duration, insertion losses for both the TE and TM polarizations were measured. Additional diffusions in increments of one hour were carried out and insertion loss measurements repeated right after. It can be observed that the insertion loss difference between both polarization modes is much larger for shorter diffusion times. In the devices of interest for this work, insertion losses for both polarizations should be as close as possible to each other; otherwise the polarization conversion efficiencies would be different for each input polarization after propagating over the same waveguide.

One parameter used to evaluate mode confinement and similarity between polarization modes (TE and TM) is the near field intensity mode profiles. Figure 22

shows the test setup used to measure them. The light source used is a distributed feedback (DFB) laser diode(λ = 1558.2nm) from Alcatel (Module: 1915-LMI) controlled by a stabilized current source from ILX Lightwave (Model LDC-3712). The current driven through the diode and the junction temperature were set at 36.76mA and 20^{o}C, respectively, in order to achieve 1.0mW of optical power at the laser pigtail output reference plane.

The laser diode pigtail was spliced to a single mode fiber (Corning SMF-28^{TM}) and later wound into a fiber polarization controller (Thorlabs Inc., Model FDC010) to enable switching the polarization state of the light input to the device being tested. Light from the polarization controller was butt-coupled to channel waveguides through one of the device polished end facet.

After propagation through the sample, the beam emerging from the 20X objective lens was focused on a vibrating mirror and directed through a 100μm slit. The slit could be oriented either vertically or horizontally depending on which profile is being measured: vertically for transverse profile (along substrate crystalline z axis), horizontally for depth (along substrate crystalline x axis). After going through the slit, light impinged on a Ge photodetector and its power level measured by an optical power meter (same used in insertion loss measurements).

The vibrating mirror was driven with a voltage waveform, resulting in a scan of the waveguide output near field being imaged on the slit. Horizontal and vertical scans were obtained by rotating mirror assembly 90º relative to the vibration axis.

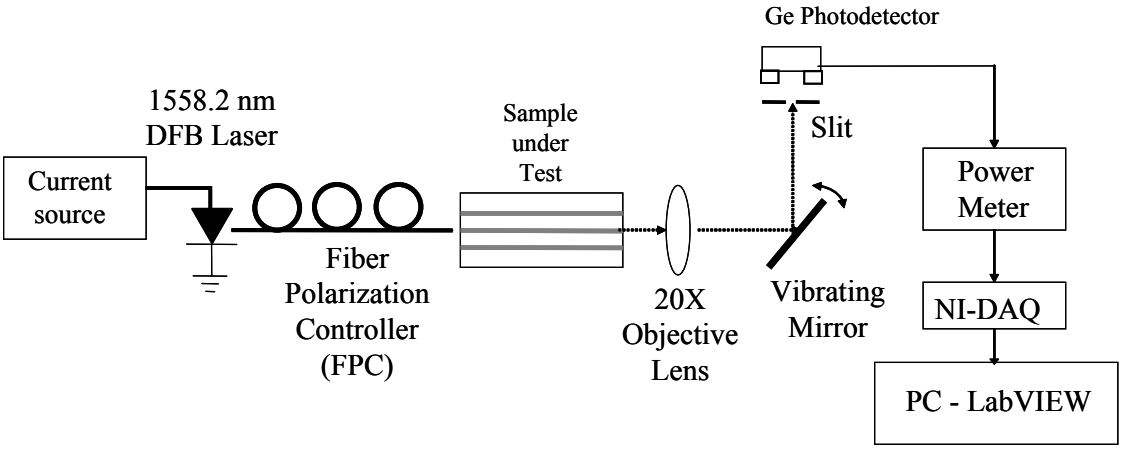

Fig. 22. Schematic diagram for field intensity mode profile measurement setup.

The slit allowed to improve the profile spatial resolution, letting only part of the light strike the detector head.

The output from the optical power meter was connected to a computer via a 16-bit digitizing board (NI-DAQ) from National Instruments for display and storage of the data. The LabVIEW programming environment was used to read the power level reaching the detector at a certain instant and construct the mode profile for one vibrating mirror sweep. All data was stored in text files.

A splitter was positioned at the sample under test site and since the spatial separation from the output waveguides was known to be 67 μm center-to-center, the time scale of the readings could be calibrated to distances.

Figure 23 shows the obtained mode profiles for transversal and depth distributions for both the TE and TM polarizations on a 7 μm wide waveguide on sample RD01 after 13 h diffusion duration. Single mode propagation for both the TE and TM

polarizations in this waveguide can be confirmed from the obtained images. The images show a symmetric Gaussian-like distribution for the transversal profile scan, and an asymmetric profile for the depth profile.

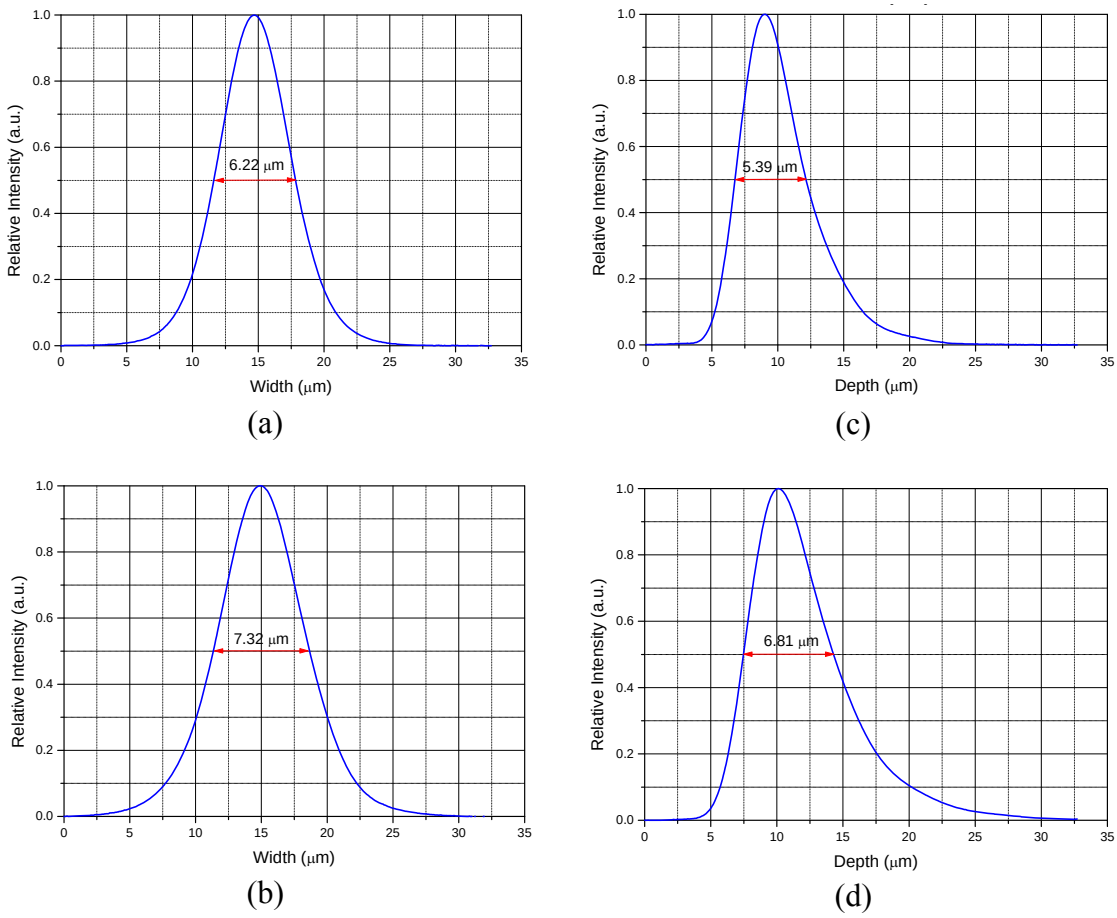

Fig. 23. Intensity profiles for a 7 μm wide channel waveguide on sample RD01. The x axis scale is already calibrated in distance: (a) TE transversal profile; (b) TM transversal profile; (c) TE depth profile; (d) TM depth profile.

This fact is due to the symmetry characteristics of the refractive index profile in the guiding region. In the depth direction the structure is highly asymmetric having 3 layers (air, guide and substrate) owing to different exponential decay coefficients in air and in the substrate, therefore resulting in the profile asymmetry along the same direction.

From figure 23, it is possible to notice that for both polarizations single mode propagation is attained and also that the TE mode is much more confined than the TM mode.

B. Uniform-Grating TE-TM Polarization Converters

The uniform-grating TE-TM polarization converter is another building block in the realization of the sparse grating filter. It is fabricated by adding a continuous strain-induced grating on top of a single-mode, Ti-diffused straight channel waveguide.

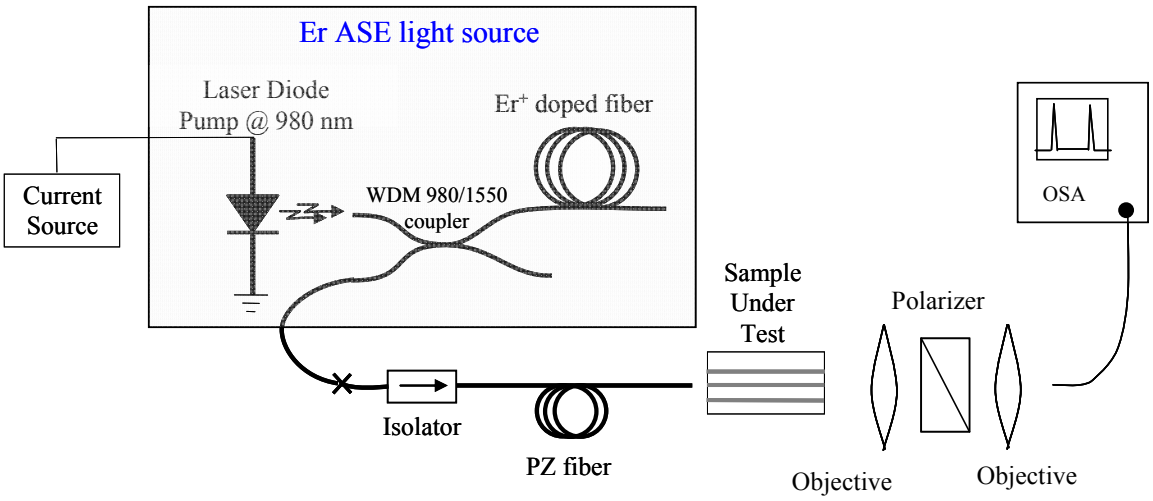

Fig. 24. Schematic diagram of the experimental set up used to test the TE-TM polarization converters.

The test setup used to characterize the polarization converter is presented in figure 24.

A broadband source is convenient to characterize wavelength selectivity. The amplified spontaneous emission (ASE) Erbium doped fiber (EDF) that was used as the broad band light source is the same used in the insertion loss measurement.

The test setup is changed at the output: a 20X objective is included to expand the beam to conform it to go through a bulk polarizer; the bulk polarizer is included to allow selecting the polarization state that will be analyzed in the Optical Spectrum Analyzer (OSA), since the converted and unconverted portions of light are orthogonal to each other; another 20X objective was included to refocus the light and couple to a single mode fiber, which is connected to the OSA input; last the Optical Spectrum Analyzer (Anritsu, Model MS9710C) is included to allow characterize the wavelength selectivity of the device. A typical emission spectrum of the amplified spontaneous emission Erbium doped fiber light source obtained directly from the OSA is presented in figure 25.

The substrate temperature was controlled by placing the sample on a Cu plate that was located on top of a Thermo-Electric Cooler (TEC). A thermistor (Omega Model: 44030) was placed in contact with the Cu plate and close to the sample to measure the temperature at which the substrate was. Everything is set on a metallic arm, which in turn was fixed to x-y-z translation stage (LineTool Co., Model: A-RHFF) equipped with differential micrometric screws in order to allow a precise positioning of the sample with respect to the input and output optics.

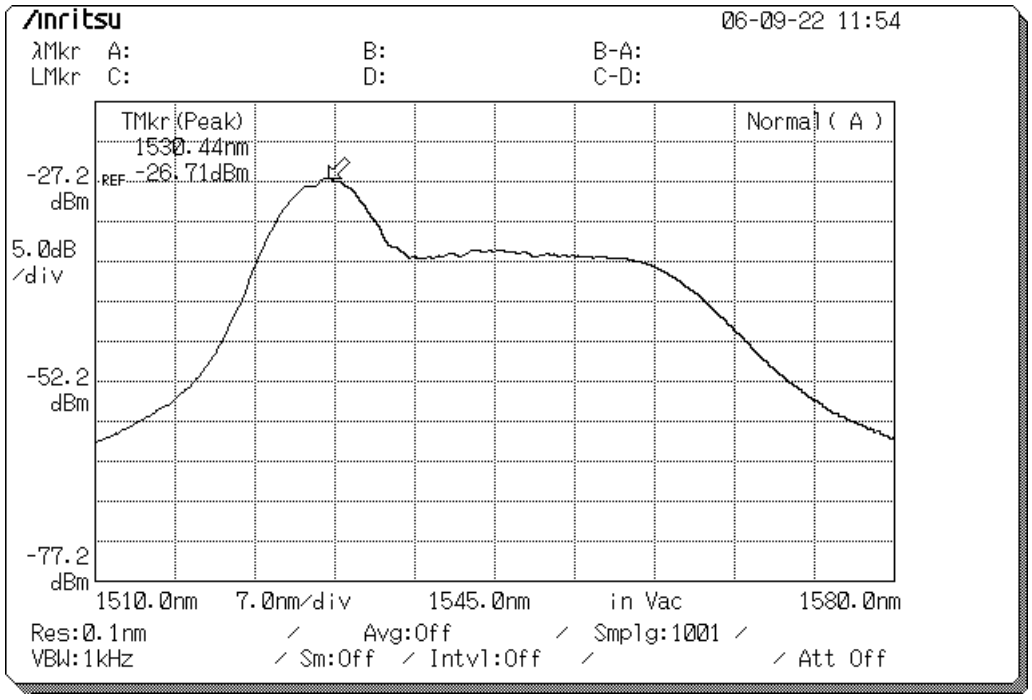

Fig. 25. Amplified spontaneous emission from an Erbium doped fiber source.

The strained SiO_2 film thickness and substrate temperature during the film deposition process are key parameters to be adjusted in optimizing the device polarization conversion efficiency.

Various converters of different SiO_2 film thicknesses were deposited and characterized. It was found that for a substrate temperature of 389 ^oC during deposition and a SiO_2 film thickness of 1.7 μm 99.8% conversion efficiency was achieved.

The output spectra of a uniform-grating TE-TM polarization converter fabricated on sample RD01 are shown in figure 26 for both TE and TM polarized inputs.

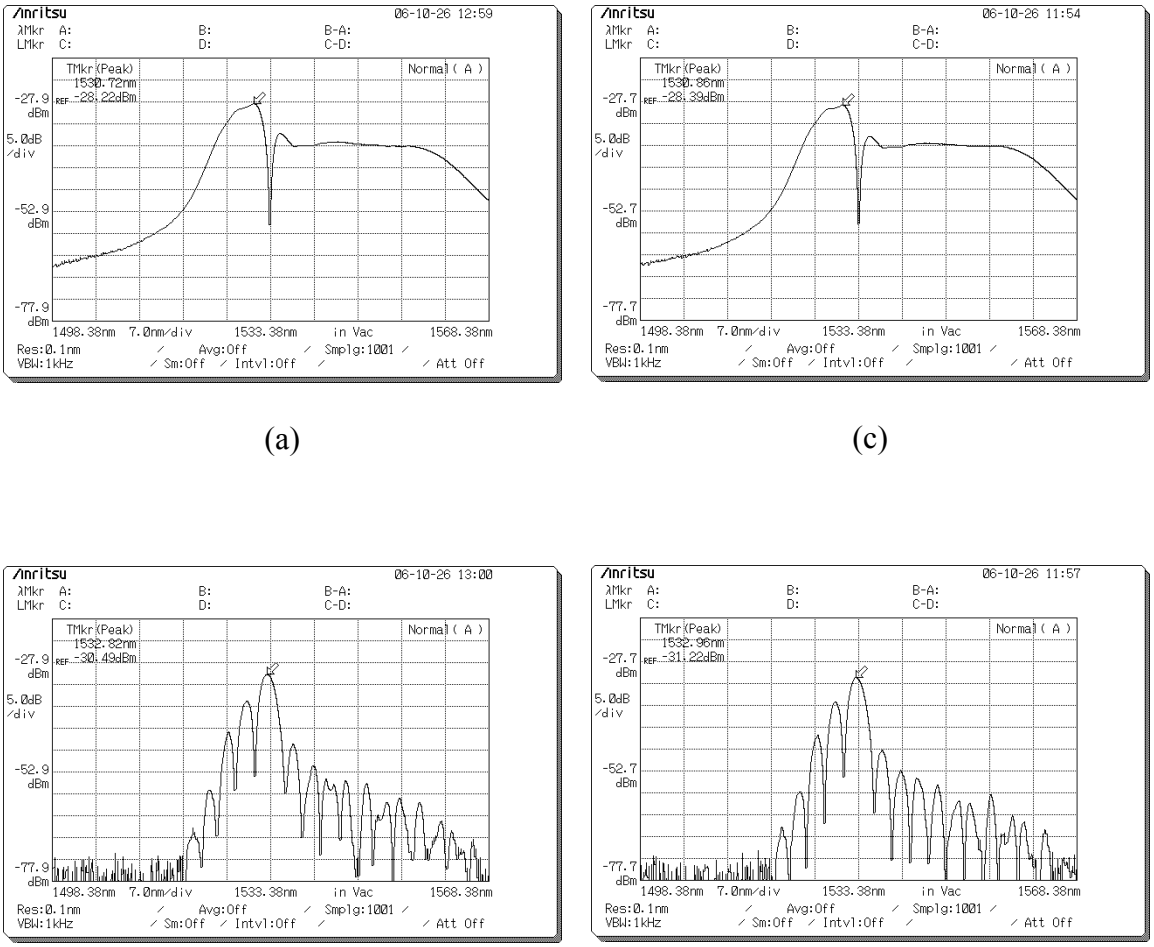

Fig. 26. Output spectra from a uniform-grating TE-TM polarization converter fabricated on sample RD01: (a)TM input/TM output (unconverted); (b) TM input/TE output (converted); (c) TE input/TE output (unconverted) and (d) TE input/TM output (converted).

The grating pattern had a spatial period of 21μm and a total of 500 strain-induced grating periods. Figure 26 (a) and (c) show the unconverted output spectrum in logarithmic (dB) scale for TM and TE inputs, respectively. Figure 26 (b) and (c) show the converted

output spectrum, also in dB scale, for TM and TE inputs, respectively. It can be noticed that they present very similar output behaviors (converted and unconverted) for both input polarizations. The measured phase-matched wavelength is 1532.82 nm for TM mode input and 1532.96 nm for TE mode input. The polarization conversion efficiency (PCE) may be calculated the same that was described on equation (111), rewritten below in a generalized format for both polarizations

$$PCE = \frac{P_{conv}(\lambda)}{P_{unconv}(\lambda) + P_{conv}(\lambda)} \tag{140}$$

where $P_{conv}(\lambda)$ is the converted light spectrum (orthogonal to the input polarization) and $P_{unconv}(\lambda)$ is the unconverted light spectrum (same polarization as input).

The raw spectra shown on figure 26 were also retrieved in a text file format from the OSA, allowing the application of equation (140) to calculate the polarization conversion efficiencies (PCEs). The theoretical polarization conversion efficiency may also be calculated. It is employed a method identical to the one used to generate the spectrum in figure 12. Figure 27 shows a plot comparing the PCEs for each polarization input with the theoretical expected spectrum. It can be noticed that they are in very good agreement.

The waveguide mode birefringence may also be determined by use of equation (95), yielding

$$\Delta n_{TE-TM} = 0.072994 \tag{141}$$

As stated before on this dissertation, the temperature dependence of the bulk substrate birefringence provides a mean of tuning the phase-matched wavelength.

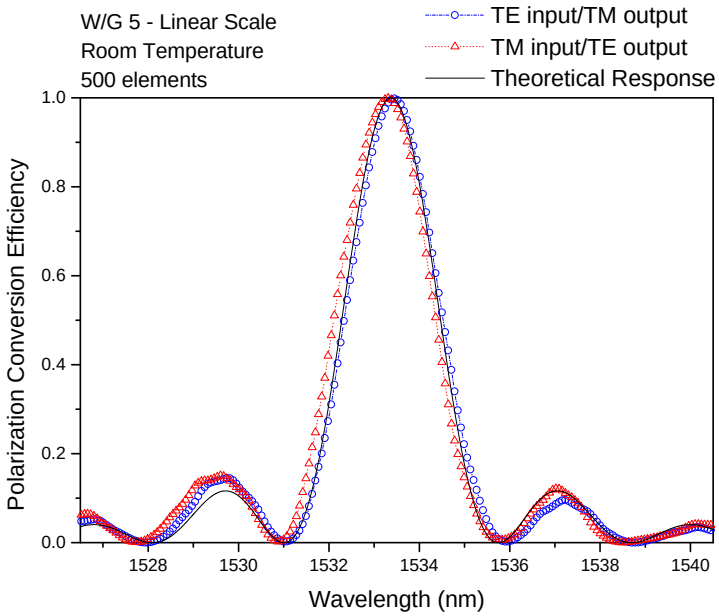

Fig. 27. Polarization conversion efficiencies (PCEs) for uniform-grating TE-TM polarization converter: TE polarization input (red up-triangle) and TM input polarization (blue circle), compared with the theoretical response (solid black).

The substrate temperature may be changed (heating or cooling) by applying different values of electric current to the thermo-electric cooler on which the sample is placed. The temperature was obtained through the reading of the thermistor resistance.

This way, different values of electrical current were applied to the TEC. It was allowed enough time for the heat exchange reach a steady state and then the spectra for the polarization modes (converted and unconverted) were measured and the temperature obtained by reading the thermistor resistance. The shift of the phase-matched wavelength was observed as can be seen with the calculated PCEs in figure 28 (a). A tuning curve for

the phase-matched wavelengths can be plotted and it is shown in figure 28 (b). The obtained temperature tuning rate for the phase-matched wavelength on sample RD01 was $d\lambda/dT = -1.3419\ \text{nm}/^{o}C$.

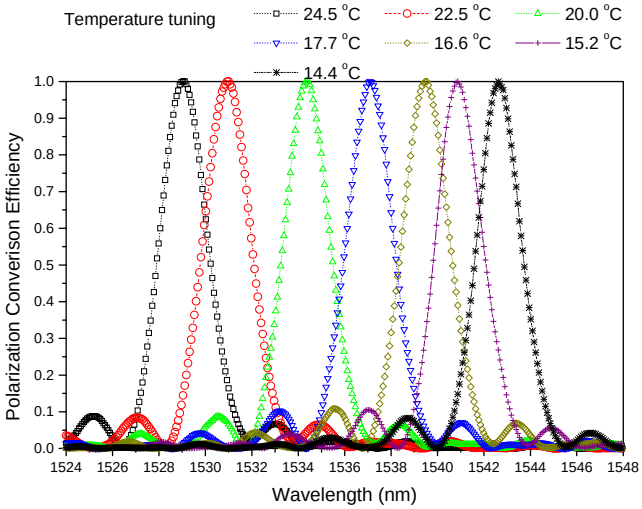

(a)

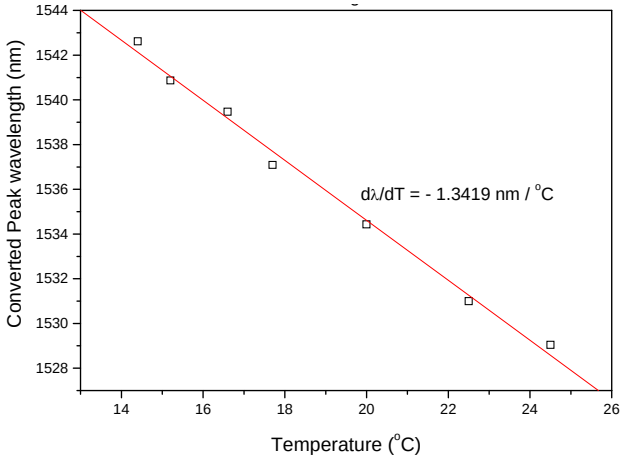

(b)

Fig. 28. Results from the phase-matched wavelength temperature tuning: (a) polarization conversion efficiencies for different temperatures; (b) phase-matched wavelength temperature dependence.

C. Tunable Sparse-Grating TE-TM Polarization Converters

The tunable sparse-grating TE-TM polarization converter consists of a straight channel Ti-diffused waveguide overlaid with a 6-coupling region strain induced sparse grating. The same fabrication parameters used with sample RD01 in the preceding section were used in the fabrication of sample RY07, which was cut 12mm wide by 43 mm long in order to accommodate the longer sparse grating. The device was fabricated in a three-layer configuration. First layer consisted of the waveguide layer, second layer consisted of the electrodes and last layer consisted of the sparse grating.

The deposited Ti-film thickness ended up to be 1275 Å and was diffused for 13.5 h, at 1035 ^{o}C, in wet ambient with compressed breathing air being flown in the furnace at about 190 sccm (~4 bubbles/s in the front bubbler). End facets were polished to provide low coupling loss. Overall insertion loss for the 43 mm long sample without the grating was measured 2.5 dB for the TM polarization mode and 2.17 dB for the TE polarization mode. Single mode propagation was confirmed through quick check of intensity profiles.

Then electrodes were patterned by image reversal lithography and deposited by e-beam (400 Å Cr/ 800 Å Au/ 600 Å Ti) alongside the waveguides and later defined by lift-off. Electrode gap equals 17 μm.

As the last step, the sparse grating was delineated on a SiO_2 film deposited at 390 ^{o}C by e-beam evaporation and patterned after cooling down to room temperature. SiO_2 film thickness was measured 1.75 μm.

Once the device had been produced and had its critical dimensions and integrity checked under an optical microscope, optical testing was carried out. The spectral

characteristics were investigated by using the optical setup used for the same purpose with the uniform grating TE-TM converter described in the previous section (figure 24).

The polarization conversion efficiency was determined the same way that was done in the previous section, by applying equation (140).

C-1. Spectral characteristics without applying voltage

Figure 29 shows the raw spectra obtained from the OSA for the sparse-grating TE-TM polarization converter fabricated on sample RY07 (fabrication parameters no page 109), for both TE and TM polarized inputs, when no voltage was applied to the electrodes and at room temperature (25.0 ^{o}C).

Figure 29 (a) and (c) show the unconverted output spectrum in logarithmic (dB) scale for TM and TE inputs, respectively. Figure 29 (b) and (c) show the converted output spectrum, also in dB scale, for TM and TE inputs, respectively. It can be noticed that they present very similar output behaviors (converted and unconverted) for both input polarizations. The measured phase-matched wavelength (center peak) is 1529.16 nm for TM mode input and 1529.1 nm for TE mode input. Achieved polarization conversion efficiencies were 96.1% for TE polarization input and 95.7% for TM polarization input.

Like it was done in the uniform-grating case, spectra were also retrieved in a text file format from the OSA, allowing the application of equation (140) to calculate the polarization conversion efficiencies (PCEs). The theoretical polarization conversion efficiency was also calculated through the knowledge of the grating dimensions and by

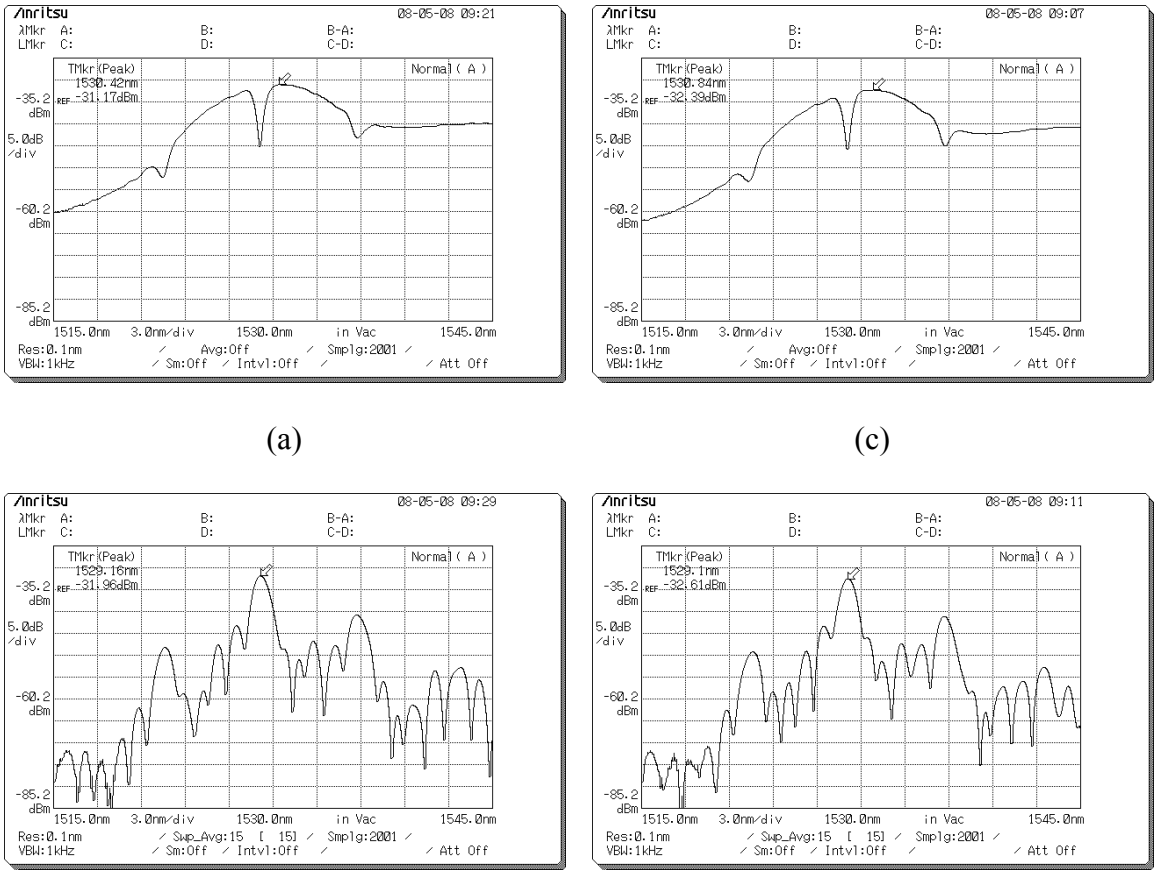

Fig. 29. Output spectra from a 6-coupling region sparse-grating TE-TM polarization converter fabricated on sample RY07: (a)TM input/TM output (unconverted); (b) TM input/TE output (converted); (c) TE input/TE output (unconverted) and (d) TE input/TM output (converted).

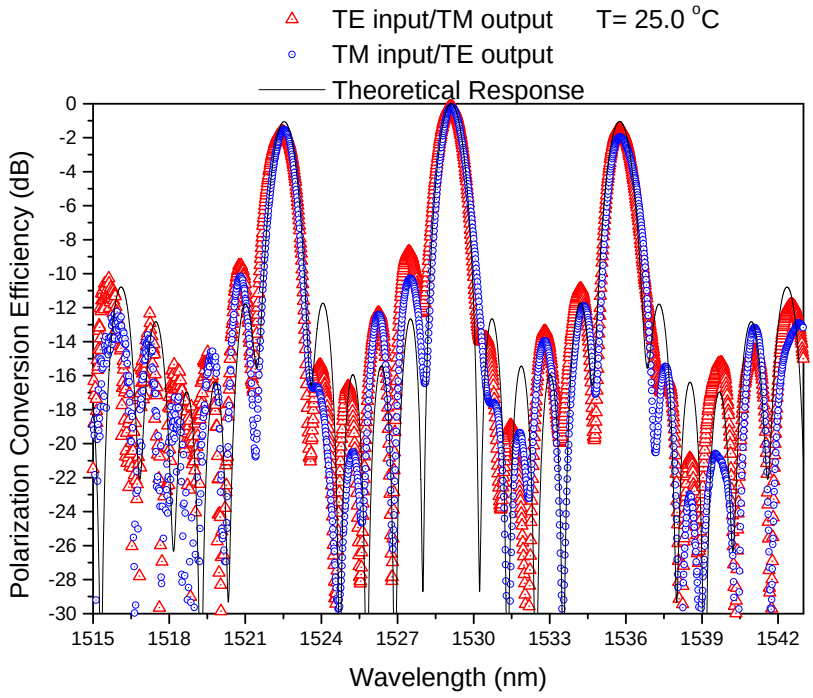

Fig. 30. Polarization conversion efficiencies (PCEs) for the 6-coupling region sparse-grating TE-TM polarization converter: TE polarization input (red up-triangle) and TM input polarization (blue circle) compared with the theoretical response (solid black).

applying the transmission matrix approach (equation (116)) used in Chapter III (recall figure 17).

Figure 30 shows a plot comparing the PCEs for each polarization input with the theoretical expected spectrum. It can be noticed that they are in very good agreement.

Applying equation (95) to the filter center peak, the waveguide modal birefringence may be determined the same way it was for the uniform grating TE-TM mode converter of the previous section.

$$\Delta n_{TE-TM} = 0.0728157 \tag{142}$$

By appropriately applying different values of electric current to the thermoelectric cooler (TEC), sample temperature was varied the same as it was described in the previous section. Temperature was obtained through the reading of the thermistor resistance. Spectral behaviors were measured for various temperatures and the respective polarization conversion efficiencies determined.

It was observed the shift not only in the center peak wavelength but in the whole filtering function as a result of the temperature change, characterizing temperature tuning of the device. In figure 31(a) the conversion efficiencies for the lowest and highest temperatures are shown. The conversion efficiencies for other temperatures were not plotted to avoid excessive cluttering. With the different values of the resultant center peak wavelength and respective temperature, a tuning curve was plotted.

The obtained temperature tuning rate for the center peak wavelength on sample RY07 (fabrication parameters on page 109) was determined $d\lambda/dT = -0.99929\,\text{nm}/^{\circ}C$ for TE polarization input and $d\lambda/dT = -1.00138\,\text{nm}/^{\circ}C$ for TM polarization input. The tuning curves for both input polarizations is shown in figure 31 (b).

The obtained bandwidth (FWHM) for the center peak was measured 1.044 nm around 1540.19 nm (or 131.9 GHz around 194.645 THz). Because of the proximity between theoretical response and measured responses, it may be said that they are in good agreement (within an experimental error).

In figure 30, a little asymmetry in the height of secondary peaks (those in the rejection band) in the lower wavelength side when compared with the ones in the high wavelength side can be noticed. This may be explained by a gradient in the birefringence

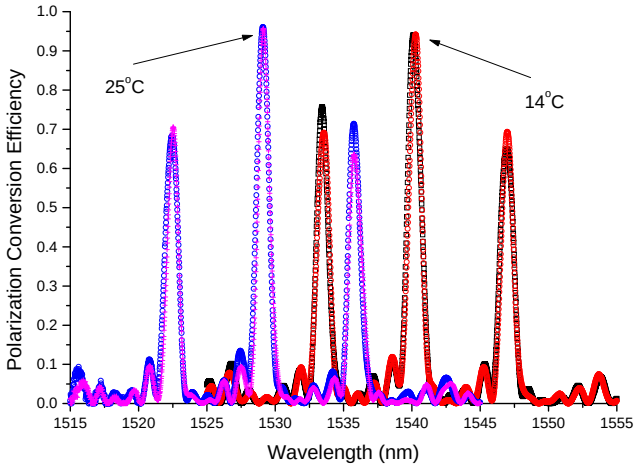

(a)

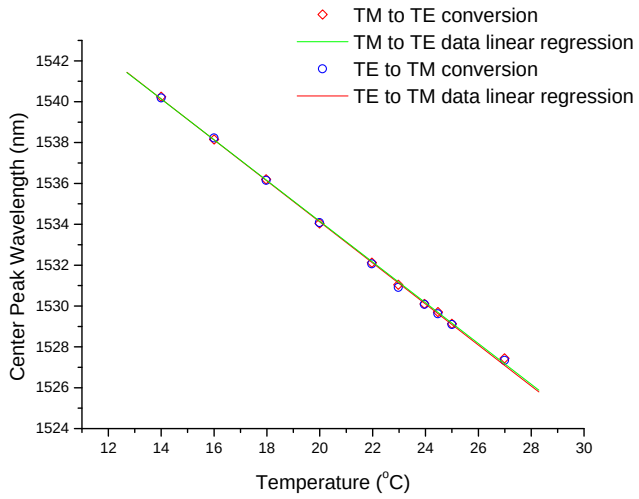

(b)

Fig. 31. Results from the 6- coupling region sparse-grating center peak wavelength temperature tuning: (a) polarization conversion efficiencies for two values of temperature (14 °C and 25 °C) - TE input polarization is shown in red and magenta, while TM input polarization is shown in black and blue; (b) center peak wavelength temperature dependence.

along the length of the sample (direction of light propagation in the waveguide), that would in turn cause a variation in the phase-matched wavelength of one section of the sparse grating to be slightly different than in the others. The net result is a "sliding" effect in the contribution of that section with respect to the contribution of the other sections in the composition of the whole filtering function, causing the asymmetry. The effect was even more severe when dealing with longer sparse gratings (8-coupling regions), in which even nulls of the filtering function were missing (reduction in the number nulls). Secondary peaks (rejection band), for these cases, rose as high as main peaks (pass band).

It was found in the literature [29] reports on similar effects in long uniform grating TE-TM polarization coupling filters, also attributing to birefringence gradients in the device.

The causes of this gradient may be many, for example non-uniformity in the Ti film thickness obtained in the deposition, causing, after diffusion, variations in the refractive indices increments along the sample, thus birefringence variations. Another hypothesis is that the Ti film thickness is uniform but the temperature along the sample during the diffusion presents a gradient, resulting in different diffusion depths along the sample, thus effective index for the modes on that section of the waveguide. It may even be that those variations do not arise from the fabrication parameters, but imperfections in the substrate ($LiNbO_3$) growth process [29].

There seems to be no dispute that those problems arise from birefringence gradients along the sample, although the debate is in fact on what causes the gradient.

These effects also seem to pose a limitation on the maximum length a device based on TE-TM mode coupling may have. That limitation, if confirmed, will result in limitations for sparse gratings on the narrowest achievable free spectral range, which in turn would result in limitations for the narrowest achievable bandwidth in the passband.

C-2. Electro-optic Tuning

The application of a voltage to the electrodes deposited alongside the waveguide generates an electric field in the waveguide mainly oriented along the crystalline z direction, changing the waveguide birefringence (recall equation (62)). By changing birefringence, the phase-matched wavelength is also changed (equation (95)). Therefore, the electro-optic effect provides another tuning mechanism for a TE-TM polarization converter.

This is also done with the highest voltage-refractive index transduction because the field orientation takes advantage of the highest electro-optic coefficient in $LiNbO_3$. The limit in the tuning range is determined by the maximum achievable voltage, which in turn is limited by dielectric strength of the $LiNbO_3$ (10 V/μm [11]) integrated across the electrodes gap. For the device being measured, the electrode gap is 17 μm, thus voltages below 170 V applied to the electrodes should be safe, if there are no free charges in the SiO_2 strain film. The spectral characteristics were measured at constant

temperature for various applied voltages to the electrodes deposited on sample RY07 (fabrication parameters on page 109).

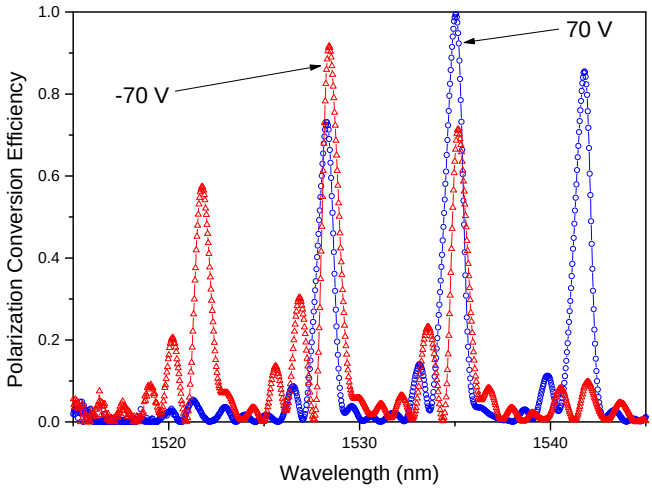

(a)

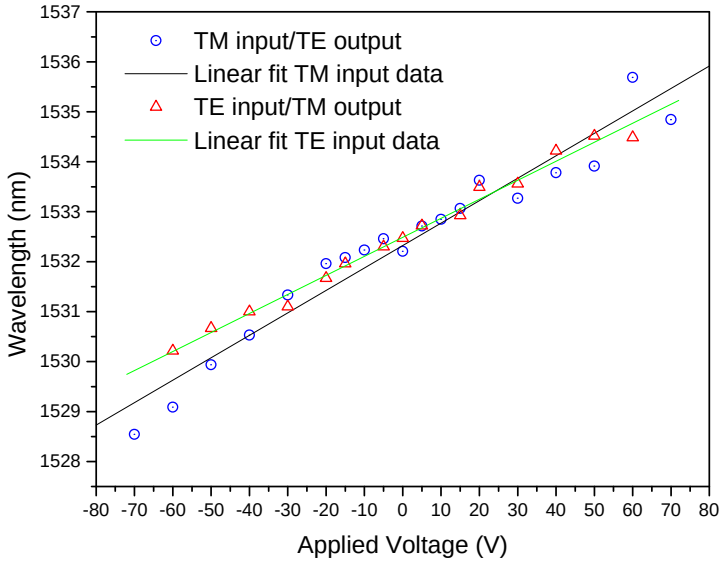

(b)

Fig. 32. Results from the 6- coupling region sparse-grating center peak wavelength voltage tuning: (a) polarization conversion efficiencies for two values applied voltage (-70 and +70 V) - TM input polarization; (b) center peak wavelength voltage dependence.

The spectra obtained when applying the two voltage extrema are shown in figure 32(a) for the TM polarization. TE polarization tuning spectra were very similar and are not presented to avoid cluttering of the plot. The center-peak wavelength of the response shifted by 5.76 nm with a variation in the applied DC voltage tuning from -70 V to +70 V, corresponding to a tuning rate of 0.045nm/V for TM input, and 0.039nm for TE input. Polarization conversion efficiency varied somewhat between both situations (from 99.4% at +70V to 91.7% at -70 V). The tuning curve for the center peak wavelength as a function of applied voltage, shown in figure 32(b), presents a linear behavior for both polarization modes, although the values for the tuning rates are low when compared to previous results in our group. An effect that might account for this difference is the presence of free-charges in the SiO_2 strain film, which under the application of external voltage would move and develop an electric field counter acting the applied field, thus reducing the voltage- refractive index transduction. The appearance of free charges in a film expected to be an insulator probably has its roots in the deposition system being used (e-beam evaporation), which is used either for metal or dielectric films. Therefore cross contamination between highly conductive and insulating materials deposited in the same chamber becomes very likely.

D. Polarization Independent Sparse-Grating Filter

The polarization independent sparse-grating filter consists of an asymmetric Mach-Zehnder interferometer overlaid with two identical 6-coupling region strain inducing sparse gratings, each one covering one arm of the interferometer. In addition to

that, there is a spatial shift between the sparse gratings in both arms equal to half a spatial period of the strain-inducing grating ($\Lambda/2$). Also, light in one arm of the interferometer travels an effective optical path equal to half of the wavelength ($\lambda/2$) longer than in the other arm. As it was shown in Chapter III, those characteristics are central to the proper functioning of the device. The waveguide width used in the interferometer is $7\,\mu m$. The pattern used in defining the Ti strips has two slightly different interferometer configurations, with respect to the optical path difference between arms. They were made this way to enable the selection of the best interferometer for the device. It was tried to use the experience acquired previously by using the same fabrication parameters optimized in the previous devices. Samples were cut 14mm wide by 53 mm long in order to accommodate the whole interferometer pattern. The device was fabricated in a two-layer configuration. First layer consisted of the waveguide layer (interferometer), second layer consisted of the the sparse grating.

The deposited Ti-film thickness on sample RY19 ended up being 1243 Å and was diffused for 13.5 h, at 1035 ^{o}C, in wet ambient with compressed breathing air being flown in the furnace at about 180 sccm (~4 bubbles/s in the front bubbler). End facets were polished to provide low coupling loss.

Before proceeding, the best interferometer to put the gratings on had to be identified.

Recall that the interferometer has a half wavelength unbalance between optical paths in both arms, i.e. a π radians phase difference. Therefore, after light have being

coupled to the sample, with no coupling structures on the waveguides, it should have no light coming out of the interferometer output. In fact light that was confined in the waveguide in both arms, upon recombining at the output branch, have phases such that the resulting field profile does not match any of the allowed mode profiles for the structure. Thus, it does not remain confined in the waveguide and leaks to the substrate. Therefore, the best waveguide will be the one that exhibits the optical path unbalance as close as possible to π, i.e. that gives the lowest output power when light is input to it.

Sample RY19 was then tested in a setup identical to the one that measured insertion loss (figure 21). The sample was laterally moved with the help of x-y-z translation stage and light was coupled to one interferometer at a time and the output power observed.

Mach-Zehnder interferometer AMZ #1b and #2b were the best ones. When 0dBm (1mW) was coupled to their input, power levels of -36.8 dBm and -38.0 dBm at the output, for the TM and TE input polarization, respectively, were obtained. While the other asymmetric MZ interferometers showed -15 dBm at the output. For comparison purposes, straight channel waveguides on the same sample showed -3.1 dBm at the output. The symmetric MZI showed -6.8 dBm at the output.

With the optimum waveguide identified, the sparse grating was then delineated on a SiO_2 film deposited at 389 ^oC by e-beam evaporation and patterned after cooling down to room temperature. SiO_2 film thickness was measured 1.78 μm.

Once the device had been produced and had its critical dimensions and integrity checked under an optical microscope, optical testing was carried out.

The spectral characteristics were investigated by using the same optical setup used for insertion loss measurement (figure 21), and thus the polarizer needed previously at the output was indeed eliminated from the test setup.

This time it is not possible to determine the polarization conversion efficiency because the unconverted light is not accessible at the waveguide output, once it is scattered to the substrate at the recombination branch.

Since the Er ASE spectrum is not uniform along the bandwidth of interest, the filter measured spectrum should be normalized with respect to that ASE spectrum. The ASE spectrum is obtained from a straight channel waveguide placed on the pattern for other reasons including the measurement of this normalization spectrum.

With both spectra (filter and ASE) retrieved from the optical spectrum analyzer in a text file format as before, the filter normalized spectrum can be calculated *a posteriori* by the relationship

$$P_N(\lambda) = \frac{\left(\frac{P_f(\lambda)}{P_{st}(\lambda)}\right)}{\left(\frac{P_f^{MAX}(\bar{\lambda})}{P_{st,}(\bar{\lambda})}\right)} \tag{143}$$

where $P_N(\lambda)$ is the filter normalized spectrum; $P_f(\lambda)$ is the filter spectrum measured at the filter output; $P_{st}(\lambda)$ is the spectrum measured at the straight channel output; for the straight channel waveguide; $P_f^{MAX}(\bar{\lambda})$ is the filter power density at the center peak

wavelength ($\overline{\lambda}$) and $P_{st}(\overline{\lambda})$ is the power density level for the measured straight channel spectrum at the center peak wavelength.

Figure 33 presents the "raw" (not normalized) spectra measured at the filter output for each polarization input to the filter and at a constant temperature.

The center peak wavelength is 1531.88 nm for the TM polarized input and 1532.0 for the TE polarized input.

As can already be seen, the form of the measured spectra for both cases is very similar, hinting at the polarization independence of the device.

To confirm, the normalized spectra for each polarization should be superimposed on the same plot. This is done in figure 34.

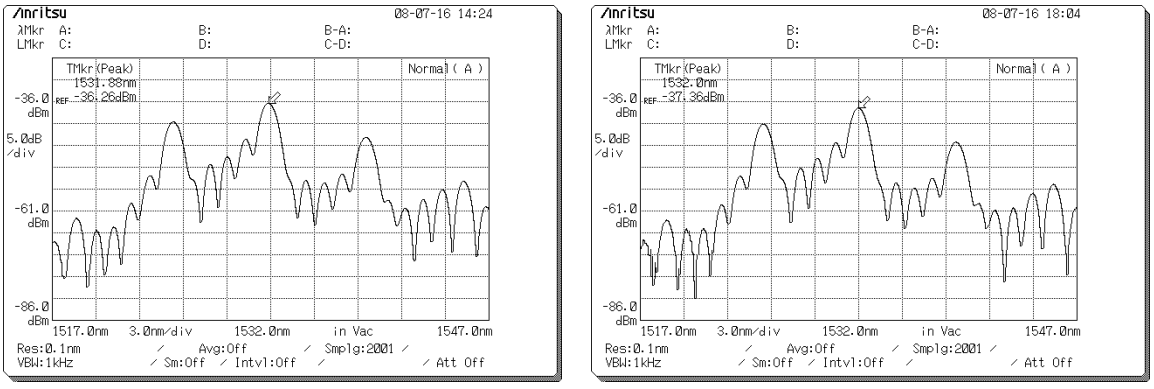

(a) (b)

Fig. 33. Output spectra for the polarization independent sparse grating filter for different polarizations input to the device: (a) TM polarized input; (b) TE polarized input.

Since electrodes were not deposited on this sample the only mean that the filter response can be tuned is by changing the substrate temperature. Like done with the devices in the previous sections, the substrate temperature was modified by changing the current applied to the TEC which is in thermal contact with the sample and monitored through the measuring the resistance of a thermistor that is also in thermal contact with the platform where the tested sample is placed.

For each temperature, the filter output spectrum was measured, normalized and the center peak wavelength identified. The plot of the center peak temperature dependence is plotted in figure 35(b), while the spectra obtained at the two measured temperature range extrema are plotted in figure 35(a) for the TE polarization.

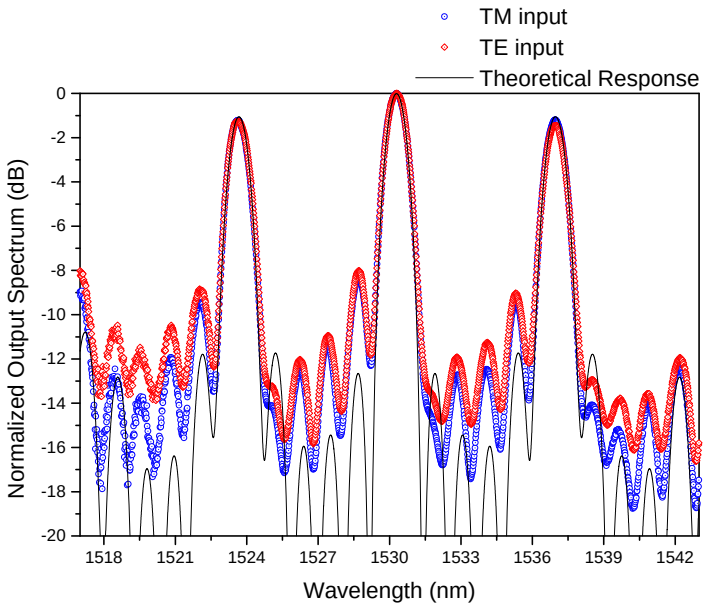

Fig. 34. Normalized output spectra for the polarization independent sparse grating filter for different polarizations input to the device: TM polarized input (blue circle); TE polarized input (red diamond); theoretical (black solid).

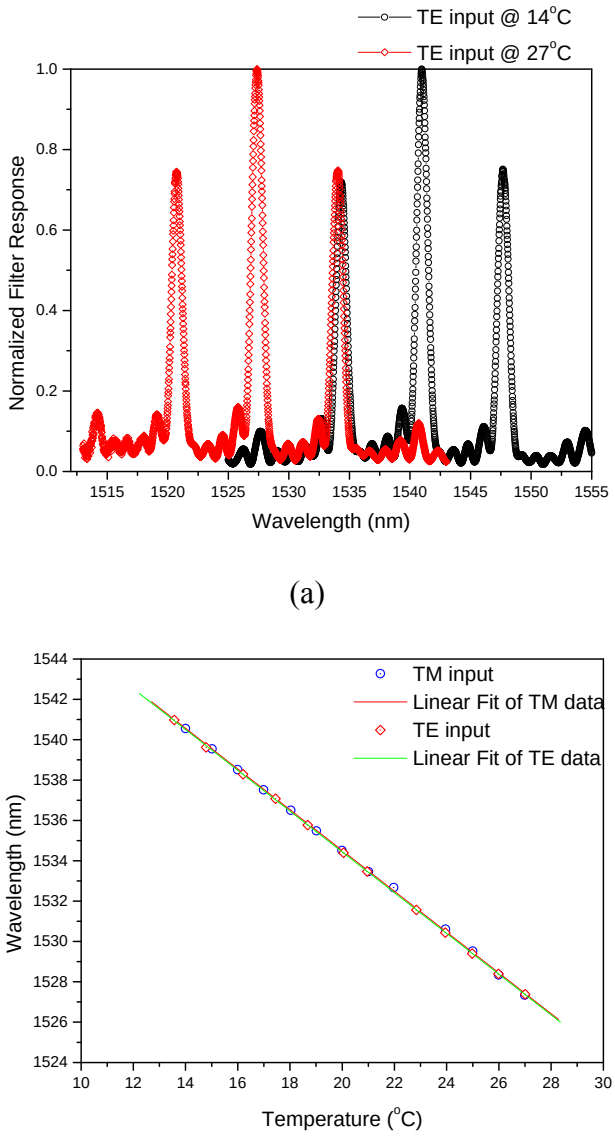

Fig. 35. Temperature tuning experiment results: (a) normalized output spectra of the polarization independent sparse grating filter at different temperatures: black circles 14°C; red diamonds 27 °C – TE polarization input only; (b) tuning curves for both polarizations.

TM polarization responses are not showed to avoid excessive cluttering on the plot but were indeed very close to the ones being showed.

The temperature tuning rate obtained for the center peak wavelength on sample RY19 was determined $d\lambda/dT = -0.99997\,\text{nm}/^{o}C$ for TE polarization input and $d\lambda/dT = -0.99985\,\text{nm}/^{o}C$ for TM polarization input.

The striking match of the normalized spectra for both input polarizations, seen on figure 34 definitely shows the device polarization independent behavior. Also the match with the theoretical response confirms the realizability of the designed filtering function by employing the sparse grating concept.

Higher number of nulls in between main peaks may be obtained by designing a device with more coupling regions and conveniently adjusting the coupling strengths for each region, according to design procedure shown. Narrower or wider free spectral ranges may also be obtained by spacing more or less the coupling regions. Those facts show the design flexibility in adapting to various needs.

The same asymmetry between low and high wavelength-side for secondary peaks (around the main peaks) observed in the straight channel sparse grating converter is also observed here. This is may constitute a limitation in the design. A better control of the fabrication parameters may be able to reduce birefringence gradients responsible for this effect, leading to an improvement in the filter characteristic.

Electro-optic tuning could have also been used to tune the filter characteristics, although it was not done on this work. It is a natural development in the research of this device.

E. Future Work

The first suggestion for future work is to use a 4-port asymmetric interferometer in making the sparse grating filter instead of the 2-port used in this work. With this improvement, add-drop filters with the sparse grating filtering characteristic may be realized. It will be possible because the unconverted light is not lost to the substrate in a radiation mode, being just redirected to the device through port. Also, the inclusion of a port on the device input side allows a channel to be added. Still on this line of work, electro-optic and temperature tuning should be employed.

The second suggestion is concerned in realizing arbitrary "zero-only" filtering functions, like gain equalizers or even some dispersion compensators. First a z-transform domain polynomial must have its coefficients adjusted to approximate the desired filtering function, for example by a least-squares algorithm. Then by using those coefficients in the synthesis algorithm, described in this and other works, the coupling coefficients for each of the regions and phases that should be accumulated between them are determined, yielding to coupling region and clear region lengths.

Filtering functions with poles cannot be realized by this topology alone. If poles are needed to approximate a desired filtering funtion, the inclusion of IIR devices, like ring resonators, Gires-Tournois interferometers or Fabry-Perot interferometers must be included in the light path and in combination with sparse gratings (FIR type).

CHAPTER VI

CONCLUSION

A new type of devices employing the sparse-grating concept was developed. This type of devices may find application as filters in DWDM communication systems due to the fact that they are able to generate very narrow bandwidth filters in the passband with adjacent channels in the stopband placed by design on nulls of the filtering function. To realize these filtering functions, the codirectional coupling between orthogonal modes in a waveguide (TE-TM conversion) was employed. Devices proving the concept and realizing filtering functions were produced on an x-cut $LiNbO_3$ substrate, with y-propagation waveguides. It presented a narrower 3dB bandwidth (FWHM) when compared to previous research that employed uniform codirectional TE-TM polarization mode coupling. The obtained bandwidth was 1.0 nm operating around 1530 nm. Two types of devices were fabricated. The first one employed straight channel waveguides and had an intrinsic polarization dependent behavior, highly undesirable in optical communication systems. The second one employed interference between light traveling in a 2-port asymmetric Mach-Zehnder interferometer to generate a polarization independent behavior and circumvent that problem. For the straight channel device, temperature and voltage (electro-optic) tuning of the selected wavelengths were employed. For the polarization independent device only temperature tuning was employed.

Six-coupling region strain-induced sparse gratings were overlaid on 7 μm wide Ti-diffused channel waveguides in both devices. One optimum set of fabrication parameters for waveguides and SiO_2 strain film was identified. The Ti film was deposited on the sample to around 1250 Å thickness, patterned and diffused at 1035 ^oC for 13 h. Fiber-to-fiber insertion loss for the waveguide was 2.5 dB for the TM polarization and 2.1 dB for the TE polarization on a 43 mm long sample. Under these fabrication conditions, the channel waveguides were confirmed to be single mode for both polarizations through intensity profile measurements. The measured mode diameters (FWHM) of the mode near field profiles were 6.22μm in the transversal (horizontal) scan and 5.39μm in the depth (vertical) scan for TE polarization, while those for the TM polarization were 7.32μm and 6.81 μm, respectively.

The spatially periodic static-strain inducing SiO_2 surface film was obtained by depositing a 1.7μm thick SiO_2 with the substrate ($LiNbO_3$) preheated and kept at 389ºC during the whole deposition. It was let cool down to room temperature and patterned with a spatial period of 21μm. By using these parameters a uniform grating with 500 periods of the grating (10.5 mm) was delineated on a straight channel waveguide and yielded a polarization conversion efficiency of 99.9% a 3dB bandwidth (FWHM) of 2.3nm, in close agreement with the theoretical value of 2.4 nm.

Temperature tuning was used to shift the peak wavelength and a rate of negative 1.3419nm/^oC was obtained for the uniform grating.

Parameters determined in this experiment were employed in producing high polarization conversion efficiency sparse gratings. Center peak wavelength polarization

conversion efficiencies (PCEs) as high as 99% were obtained in straight channel waveguides with overlaid six-coupling region strain-induced sparse gratings. Thermal tuning was also used to shift the peak wavelength, and a thermal tuning rate of -1.0 nm/°C was measured for both polarizations. Electro-optic tuning was also demonstrated in the straight channel sparse-grating device. A shift for the peak conversion wavelength of 5.76 nm was realized over a tuning voltage ranging from -70V to +70V. The electrode gap is 17μm, and tuning rates of 0.045nm/V for the TM and 0.039nm/V for the TE polarization were obtained.

A polarization independent sparse grating filter was also demonstrated. It presented the same spectral behavior obtained in the straight channel waveguide. The major difference is that no polarization filter is needed at the device output to observe the filtering function. The obtained filtered spectrum was demonstrated to be the same for both input polarizations. Selected channels showed a 3 dB bandwidth (FWHM) of 1.0 nm. Temperature tuning was employed, and rates of negative 1.0 nm/^{o}C for both polarizations were achieved.

Obtained results were compared to theoretical responses and they were found to be in very good agreement.

REFERENCES

[1] G. Keiser, *Optical Fiber Communications*, 2nd ed. Singapore: McGraw-Hill, 1991.

[2] P. E. Green, Jr., *Fiber Optic Networks*. Englewood Cliffs, NJ: Prentice Hall, 1993.

[3] G. P. Agrawal, *Fiber Optic Communication Systems*, 2nd ed. New York: John Wiley & Sons, 1997.

[4] S. V. Kartalopoulos, *Introduction to DWDM Technology, Data in a Rainbow.* Piscataway, NJ : IEEE Press, 2000.

[5] D. Sadot and E. Boimovich, "Tunable optical filters for dense WDM networks," *IEEE Commun. Mag.*, pp. 50-55, Dec. 1998.

[6] P. Tang, "Polarization independent electrooptically tunable add drop filter in Ti:$LiNbO_3$ at 1.55 μm wavelength regime," Ph.D. Dissertation, Texas A&M University, Department of Electrical Engineering, College Station, Texas, 2002.

[7] P. Tang, O. Eknoyan, and H. F. Taylor, "Rapidly tunable optical add-drop multiplexer (OADM) using a static-strain-induced grating in $LiNbO_3$," *Journal of Lightwave Technology*, vol. 21, no. 1, pp. 236-245, Jan. 2003.

[8] H. Kuo, "Investigation of an electrooptic tunable filter in litium niobate," Ph.D. Dissertation, Texas A&M University, Department of Electrical Engineering, College Station, Texas, 2006.

[9] H. F. Taylor, "Tunable spectral slicing filters for dense wavelength division multiplexing," *Journal of Lightwave Technology*, vol. 21, no. 3, pp. 837-847, March 2003.

[10] C. A. Balanis, *Advanced Engineering Electromagnetics.* New York: John Wiley & Sons, 1989.

[11] A. Yariv and P. Yeh, *Optical Waves in Crystals.* New York: John Wiley & Sons, 1984.

[12] H. Nishihara, M. Haruna, and T. Suhara, *Optical Integrated Circuits*. New York: McGraw-Hill, 1989.

[13] E. A. J. Marcatili, "Dielectric rectangular waveguide and directional coupler for integrated optics," *The Bell System Technical Journal*, vol. 48, pp. 2071-2102, Sept. 1969.

[14] R. M. Knox and P. P. Toulios, "Integrated circuits for the millimeter through optical frequency range," *Proceedings of MRI Symposium on Submillimeter Waves*, J. Fox editor, pp.497-516, Brooklyn, NY: Polytech. Press, 1970.

[15] G. B. Hocker and W. K. Burns, "Modes in diffused channel optical of arbitrary index profile," *IEEE Journal of Quantum Electronics*, vol. 11, no. 6, pp. 270-276, June 1975.

[16] G. B. Hocker and W. K. Burns, "Mode dispersion in diffused channel waveguides by the effective index method," *Appl. Opt.*, vol. 16, no. 1, pp. 113-118, January 1977.

[17] I. P. Kaminow, *An Introduction to Electrooptic Devices*. New York: Academic Press, 1974.

[18] C. K. Madsen and J. H. Zhao, *Optical Filter Design and Analysis: A Signal Processing Approach*, 1st. ed. New York, NY: John Wiley & Sons, 1999.

[19] Y. S. Kim and R. T. Smith, "Thermal expansion of lithium tantalate and lithium niobate single crystals," *Journal of Applied Physics*, vol. 40, no. 11, pp. 4637-4641, Oct. 1969.

[20] Z. Tang, O. Eknoyan, H. F. Taylor and V. P. Swenson, "Tunable guided-wave optical polarization converters in lithium tantalite," *Applied Physics Letters*, vol. 62, no. 10, pp. 1059-1061, March 1993.

[21] K. Saitoh and M. Koshiba, "Stress analysis method considering piezoelectric effects and its application to static strain optic devices," *Journal of Lightwave Technology*, vol. 17, no. 9, pp. 1626-1633, Sep. 1999.

[22] D. F. Nelson and R.M. Mikulyak, "Refractive indices of congruently melting lithium niobate," *Journal of Applied Physics*, vol. 45, no. 8, pp. 3688-3689, Aug. 1974.

[23] K. Jinguji and M. Kawachi, "Synthesis of coherent two-port lattice-form optical delay-line circuit," *Journal of Lightwave Technology*, vol. 13, no.1, pp. 73-82, Jan. 1995.

[24] Y. Ping, O. Eknoyan and H. F. Taylor, "Polarisation-independent tunable bandpass filter utilising symmetric branch beam splitters," *Electronics Letters*, vol. 40, no. 15, pp. 960-962, July, 22, 2004

[25] G. D. Boyd, W. L. Bond, and H. L. Carter, "Refractive index as a function of temperature in $LiNbO_3$," *Journal of Applied Physics*, vol. 38, no. 4, pp. 1941-1943, Mar. 1967.

[26] Y. Ping, "Two-Port polarization independent electro-optically tunable wavelength filter in lithium niobate," Master Thesis, Texas A&M University, Department of Electrical Engineering, College Station, Texas, 2003.

[27] R. V. Schmidt and I. P. Kaminow, "Metal-diffused optical waveguides in $LiNbO_3$," *Applied Physics Letters*, vol. 25, no. 8, pp. 458-460, Oct. 1974.

[28] J. L. Jackel, V. Ramaswamy, and S. P. Lyman, "Elimination of out-diffused surface guiding in titanium-diffused $LiNbO_3$," *Applied Physics Letters*, vol. 38, pp. 509-511, Apr. 1981.

[29] F. Cholet, J. P. Goedgebauer and G. Ramankoto, "Limitations imposed by birefringence uniformity on narrow-linewidth filters based on mode coupling," *Optical Engineering*, vol. 40, no. 12, pp. 2763-2770, Dec. 2001.

APPENDIX A

MATLAB™ SPARSE GRATING SYNTHESIS ROUTINE

Sparse grating design.m

```
clear all
syms z unreal
syms z
reg=6;% reg is the desired number of coupling regions
b=(ones(reg,1))';
N=length(b);
p=-(0:N-1);
ZZ=(z.^(p)).';
B=b*ZZ;
omega=-10*pi:0.01:10*pi;
zz=exp(i*omega);
f=1/(2*pi)*omega;
BB=subs(B,zz);
mag2=BB.*conj(BB);
c=max(mag2);
mag2=mag2/c;
mag22=10*log10(mag2);
plot(f,mag2)
title('Square Magnitude Frequency Response for B_{n}(z)')
xlabel('Normalized Frequency (\nu - \nu_{0}/ \Delta\nu_{FSR})')
ylabel('Square Magnitude')
%xlim([-1 1]);
%ylim([-30 0]);
%%
ff=f';
mag2t=mag2';
BB=[ff mag2t];
save('designtheo6.txt','BB','-ascii','-double','-tabs')
%%
bb=b./sqrt(c);
tt=-angle(bb(N));
bbr=exp(-i*tt)*fliplr(bb);%calculates the reverse polynomial of B
aux1=conv(bb,bbr);
aux2=zeros([1,length(aux1)]);
aux2(N)=exp(-i*tt);
aux2(N)=1;
aaaar=aux2-aux1;
r=roots(aaaar);%+i*1e-5
figure
plot(r,'o r')
tetha=0:0.001:2*pi;
r1=exp(i*tetha);
hold on
plot(r1,'-b')
axis equal
title('Roots of A_{n}A_{n}^{R}(z)')
xlabel('Re')
```

```
ylabel('Im')

%% Chosing roots
ra=r(1:5);%max-phase roots (outside unit circle) should be chosen for
AnAnr
an=poly(ra);
alpha=sqrt(-bb(1)*bb(N)/(an(1)*an(N)));
if an(1)<0
   aa=real(alpha*an);
else
    aa=-real(alpha*an);
end
%% Calculating csi and phi
uu=N;
for jj=1:N-1;
    csi(uu)=atan(bb(uu)/aa(uu));
    s(uu)=sin(csi(uu));
    c(uu)=cos(csi(uu));
    auxbb=-s(uu)*aa+c(uu)*bb;
    auxaa=c(uu)*aa+s(uu)*bb;
    auxbb(uu)=[];
    auxaa(1)=[];
    nn=length(auxaa);
    phi(uu)=-unwrap(angle(auxaa(nn)))-unwrap(angle(auxbb(nn)));
    bb=auxbb;
    aa=exp(-i*phi(uu))*auxaa;
    uu=N-jj;
end
c(1)=aa(1);
s(1)=sqrt(1-c(1)^2);
csi(1)=acos(c(1));
csi
phi
```

APPENDIX B

DIMENSION DETAILS FOR THE 6-COUPLING REGION SPARSE GRATING

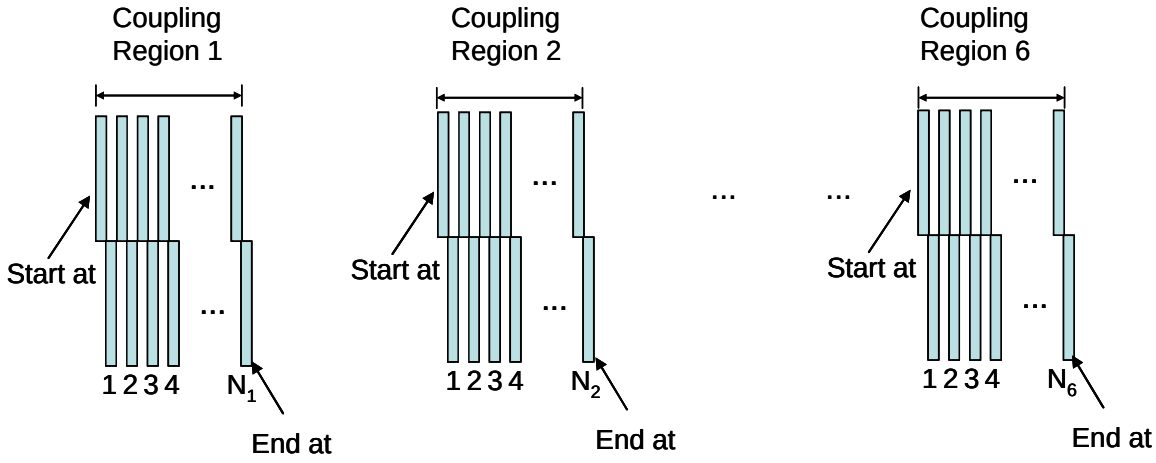

Figure 36 – Sparse grating dimension details

Table 4 – 6-coupling region sparse grating lengths and distances

Coupling Region	Starts at	Ends at	# of SiO_2 grating periods in each region (N_i)
1	0	1365	65
2	4137	5943	86
3	8379	10458	99
4	12726	14805	99
5	17241	19047	86
6	21819	23184	65

APPENDIX C

6-COUPLING REGION SPARSE GRATING PATTERN LAYOUT ON MASK SPFILTV_1

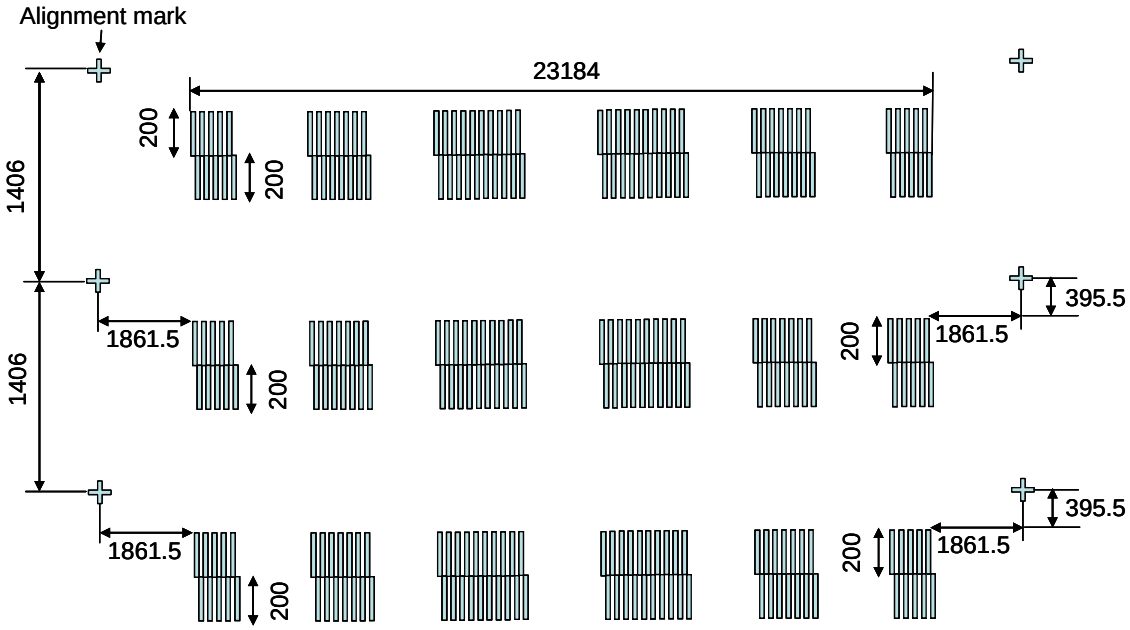

Fig. 37. 6-coupling region sprase grating mask layout details.

VITA

Renato Cunha Rabelo was born in Brasilia – DF, Brazil. He received his B.S. degree (Electronics Engineer) from Instituto Tecnológico de Aeronáutica (ITA), Brazil in 1992 and his M.S. degree also from ITA in 1998 working on fiber-optic rotation sensors. He started pursuing his Ph.D. degree at Texas A&M University in Sept. 2004, working with integrated optical devices in lithium niobate, and received his degree in December 2008. He can be reached at the following address:

Renato Cunha Rabelo

Instituto de Estudos Avançados (IEAv/CTA)

Rodovia dos Tamoios km 5,5

São José dos Campos – SP – Brazil

12228-001